

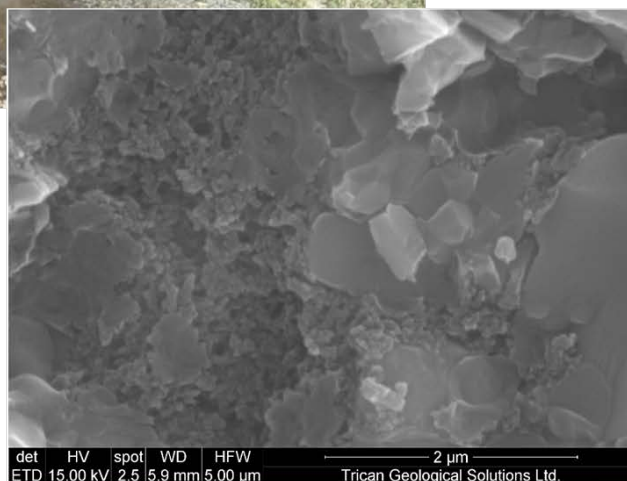


# **Chevron Canada Resources Ltd.**

## **Sample Analysis Report**

### **Yukon Diamond Core Hole # FX07-03**

#### **Northern Richardson Mountains**



G. Hayden  
Sr. Staff Geologist  
Chevron Canada Resources  
2013-11-01



## Table of Contents

SAMPLE ORIGIN & DESCRIPTION .....	2
INTRODUCTION .....	5
ANALYSES CONDUCTED & ORGANIZATION OF REPORT.....	5
SOURCE ROCK ANALYSES.....	6
MINERALOGICAL ANALYSES BY X-RAY DIFFRACTION.....	8
UNCONFINED POROSITY & MATRIX PERMEABILITY.....	10
PORE SIZE DISTRIBUTION & TOTAL POROSITY BY MERCURY POROSIMETRY .....	12
PETROGRAPHIC & SEM DESCRIPTIONS.....	16
DISCUSSION OF FINDINGS.....	84
APPENDIX.....	85
Appendix A .....	85
Appendix B .....	87
Appendix C .....	95
Appendix D .....	100
Appendix E .....	102
Appendix F.....	103
REFERENCES .....	106

*Cover photo – Outcrop of Upper Canol shales west of FX07-03 drill site where combustion has occurred in the Canol Formation. Companion photo is of porous organic matter from core at depth below weathered zone in FX07-03.*

## **SAMPLE ORIGIN & DESCRIPTION**

Samples analyzed in this study consisted of three samples of diamond drill hole core from the FX07-03 hole originally drilled in 2007 on the FOX mineral property in northern Yukon by Southhampton Ventures Inc. and Strategic Metals Ltd.

Samples were obtained at the Bostock Core Library facility in Whitehorse in 2013-06 under sampling authorization [YGS-HSBSV-2013-04](#).

Sample depths:

60.72 – 60.97 m  
67.18 – 67.48 m  
73.70 – 74.00 m

Formation sampled was the Middle Devonian Earn Group according to original mineral file assessment report (Dumala, 2007) and later ascribed to the Canol Formation (Frasier, 2012) present over the interval from surface to a depth of 95m in FX07-03.

Lithology of the samples was dominated by black siliceous shale with occasional subsidiary laminations of dark grey silty shale and dark grey siltstone which were distinct enough to warrant sub-division of sample into sub-sets (Table 1). Samples collected from FX07-03 are from depths below zone of weathering noted in the original core hole logs and described as fresh. This significantly reduced the uncertainty of weathering affects adversely affecting the composition and fabric of the rock.

**Table 1.** Sample descriptions

<b>Sample Number</b>	<b>Core Depth</b>	<b>Lithology</b>
FX 60.72	60.72 – 60.97m	Shale; black, siliceous, dense -faintly laminated
FX 67.18  FX 67.18a FX 67.18b FX 67.18c	67.18 – 67.48 m	Shale; black, siliceous, dense with lesser thin laminations of dark-grey silty shale and dark grey siltstone  -black shale sampled as sub-set A -dark-grey silty shale sampled as sub-set B -dark grey siltstone with sulphide minerals sampled as sub-set C in contact with black siliceous shale
FX 73.70	73.70 – 74.00 m	Shale; black, siliceous, dense -faintly laminated, rubbly, occasional fractures in-filled with solid bitumen

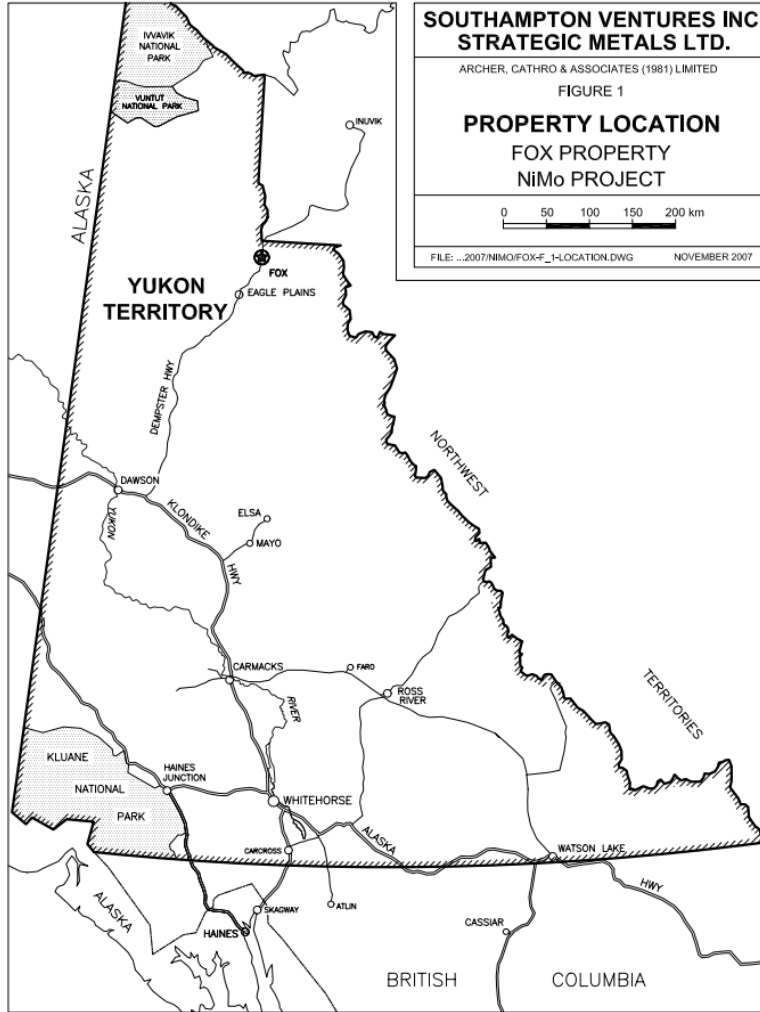


**Figure 1.** Location of FOX FX07-03 drill hole ((Dumala, 2007).

**Table 2.** Drill hole location and details

Hole	Easting	Northing	Elevation	Azimuth	Angle	Depth (m)
FX07-03	442337	7423398	550	110°	-75°	210.31

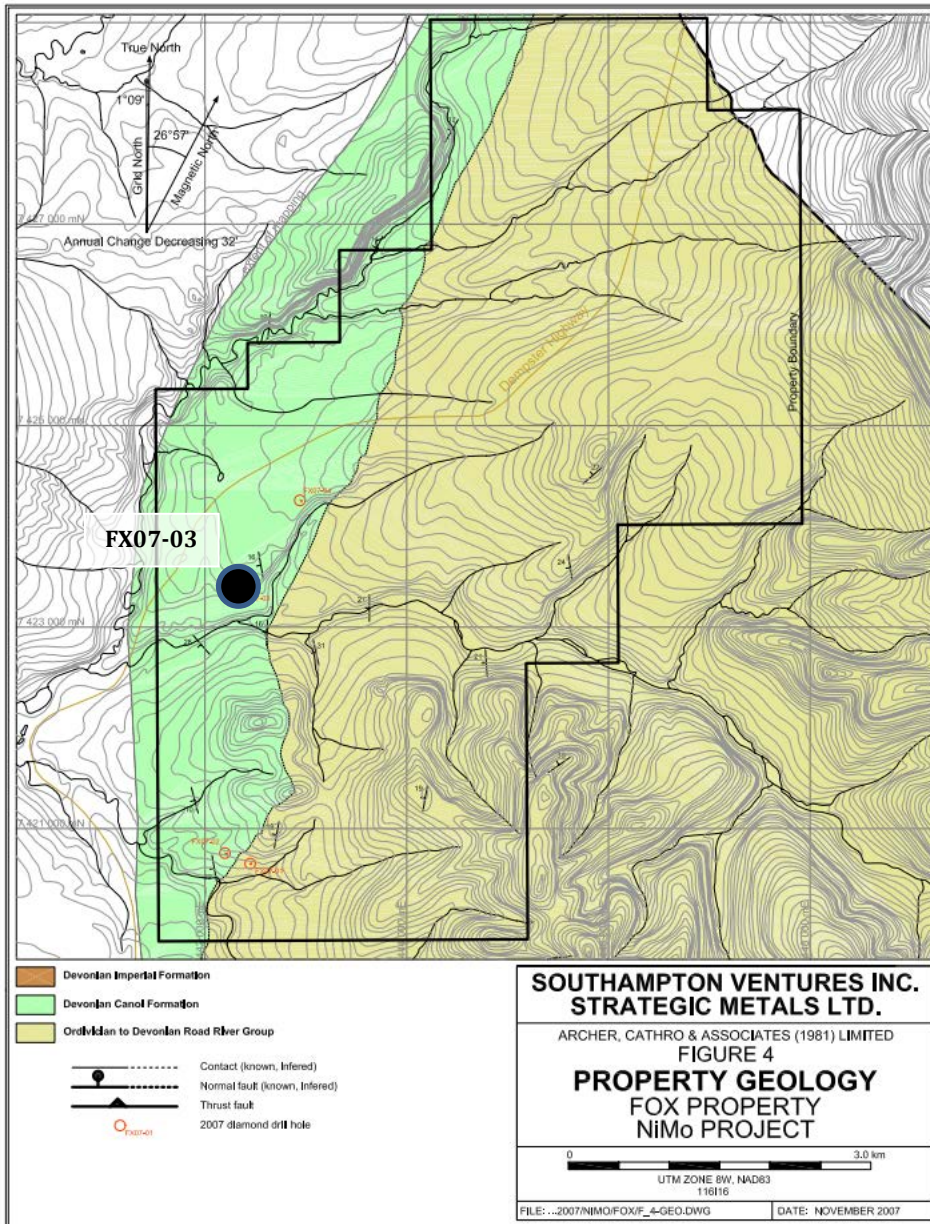


**Figure 2.** Drill hole location map with formation contacts (from Dumala, 2007). Drill hole situated on northwest flank of Richardson Mountains where Canol Formation dips gently to west at 30 degrees.

## **INTRODUCTION**

The core samples from FX07-03 were collected and analyzed for additional insights into source-rock quality and gas shale reservoir potential of the Canol Shale within the Eagle Plains basin.

Previous geochemical analysis in the public domain for the Eagle Plains Basin includes analyses by Lane et al (2010, 2012) conducted on ditch cutting samples from earlier drilled oil and gas exploratory wells via either RockEval pyrolysis or additionally XRD and vitrinite reflectance techniques. An extensive analysis of Canol and underlying Road River shale intervals was conducted on other diamond core remains from the Richardson Mountain areas by Fraser et al (2012). The descriptions by Fraser et al include written descriptions of the type and abundance of organic matter present in the Canol and Road River shales from microscopy by GSC workers.

The previous studies have established the good hydrocarbon source rock quality of the Canol. Drill hole core samples from the Richardson Mountain locations such as at Fox exhibit elevated levels of thermal maturity and indicate the Canol at this location to be over-mature for the presence of oil or wet-gas liquids and mature for dry gas generation and preservation.

The present study was intended to further assess Canol shale petrology (inorganic and organic) and textures via thin-sections, scanning electron microscopy (SEM), identification of pore types & sizes and quantify porosity and permeability utilizing standard industry techniques used to assess gas shale reservoirs.

## **ANALYSES CONDUCTED AND ORGANIZATION OF REPORT**

The analyses conducted on the three core samples are summarized in Table 3. Objective was to evaluate representative lithofacies present.

**Table 3.** Analyses conducted

	SRA/TOC	XRD	Porosity	Perm.	Pore Size	Thin - Section	SEM
FX-60.72	√	√	√	√	√	√	
FX-67.18a	√	√	√	√	√		√
FX-67.18b		√			√		√
FX-67.18c						√	√
FX-73.70	√	√	√	√	√		√

All laboratory work was conducted by Trican Geological Solutions of Calgary under the supervision of Cory Twemlow with separate authors for individual sets of analyses. The

analyses of the core samples was proceeding in parallel with the analysis of Chevron collected outcrop grab samples from the same area which remain company confidential.

All of the individual classes of analysis conducted by Trican were originally documented in separate sub-reports from Trican but have been consolidated herein into a single report for simplicity. Descriptions of techniques and procedures are referenced in appendices to this report.

The reports by Trican cover the following subjects:

1. source rock analysis referred to as SRA Analysis
2. mineralogical analysis by X-ray diffraction
3. unconfined porosity and matrix permeability
4. pore size distribution and total porosity by mercury porosimetry
5. petrographic and SEM description

All of the analyses by Trican were submitted to Chevron covered by Trican disclaimers which in essence do not warrant interpretive findings. The content of the Trican disclaimers for component analyses are attached for reference as **Appendix A**.

## **SOURCE ROCK ANALYSES**

**No. of Samples Analyzed:** 3  
**Sample Type:** Core (3)  
**Analyses Completed:** Source Rock Analysis (SRA)

### *Summary of Findings:*

The source rock potential of 3 core samples from the Chevron Core Project was determined using a Source Rock Analyser (SRA).

Variation in Tmax is a reflection of the quality of the sample and the generation of reliable S2 peaks used to determine Tmax. For most samples the S2 distribution is either non-existent (no S2 peak is present) or has poor resolution where the distribution is broad and the peak intensity (Tmax) is low/poorly defined. This can be due to low total organic carbon content, high maturity and/or mixed kerogen type. From the FX group of samples, no Tmax values were resolvable. Tmax values for the YG samples were not resolvable. The samples are overmature with respect to the oil window.

The total organic carbon content of the 3 samples from the YG group have TOC values ranging between 7.08% and 14.06%, with an average of 10.20%.

The organic matter type cannot be confidently determined due to the high maturity of the samples.

## Sample Selection and Preparation

Core samples were provided to Trican Geological Solutions by Chevron Canada. A portion of the samples were split for SRA analysis then crushed to a powder in order to obtain a representative and homogenous sample.

## Results and Interpretation

The compiled results of the SRA analyses are found in **Table 4**. **Appendix B** provides detailed notes on TOC and SRA analyses.

**Table 4.** Summarized results of SRA pyrolysis

Chevron Outcrop Project - July 2013															
Sample Groups	Sample	Sample Type	Tmax °C	Tpeak °C	S1 (mg/g)	S2 (mg/g)	S3 (mg/g)	PC (%)	PI	S2/S3	S1/TOC	TOC%	HI	OI	Tmax Data Quality
YG	FX-60.72	Core			0.07	0.15	0.21	0.02	0.32	0.71	0.01	7.08	2	3	no good
	FX-67.18A	Core			0.05	0.13	0.33	0.01	0.28	0.39	0.01	9.46	1	4	no good
	FX-73.7	Core			0.08	0.15	0.57	0.02	0.35	0.26	0.01	14.06	1	4	no good

## Thermal Maturity

Thermal maturity was evaluated in 3 core samples for the Chevron Core Project using pyrolysis derived Tmax. The temperature at which maximum rate of hydrocarbons is generated during pyrolysis is referred to as Tmax. Tmax results are calculated by the intersection of the S2 curve on the pyrogram with temperature at Tpeak. Tpeak values are corrected by a straight linear shift of 39°C in order to calculate Tmax. Tmax provides the historical baseline for thermal maturity.

The S2 quality review (**Table 4**) is an internal Trican quality control method to evaluate the highest quality samples and is based on the development of the S2 peak. A “best” quality is the highest scale in the evaluation of the S2 peak. An “excellent” quality control indicates an S2 peak which is large and symmetrical in shape. A “good” quality control indicates a well developed peak with slightly lower peak area. The “OK” quality control indicates an S2 peak that is not sharp or symmetric and has low peak area, however, the resulting Tmax value can be used with confidence as an apex to the S2 peak can still be defined with certainty. “Poor” quality S2 peaks are very small and non-symmetric; “No good” quality peaks are as stated – no discernible value for Tmax is present. However, note that all samples do provide adequate TOC measurements regardless of the quality of the S2 peaks.

In this sample suite the 3 core samples from the YG group were given “no good” qualifiers and the Tmax values were removed from the dataset as they were not resolvable.

Pyrograms for the samples analyzed are included **Appendix B** in Figure B1

## *Kerogen Type*

Various pyrolysis indices can normally be plotted to estimate the organic matter type. With increasing maturity and conversion of H and C into hydrocarbons, organic matter type becomes increasingly difficult to determine. Due to the overmaturity of the samples giving low S2 peaks and subsequent low HI values, estimating the kerogen type based on the Van Krevelen diagram is unreliable. Cross-plotting of S2 with total organic carbon, can be used in the determination of organic matter typing. Due to the low S2 for the core values, this plot is also unreliable in determining organic matter type.

## **MINERALOGICAL ANALYSES BY X-RAY DIFFRACTION**

**No. of Samples Analyzed:** 4  
**Sample Type:** core samples  
**Analyses Completed:** X-ray diffraction analysis, Rietveld refinement and bulk mineralogical quantification

### *Summary of Findings:*

The mineralogical composition of 4 core samples from the Chevron Core Project was determined by X-ray diffraction and quantified using Rietveld refinement methods. Quartz, feldspar (albite and orthoclase), carbonates (calcite, dolomite and siderite), clay minerals (mica/illite, chlorite, and kaolinite), pyrite, sulphates (gypsum, barite and bassanite), phosphates (apatite and hydroxylapatite), natrolite and possible traces of prenite were detected and quantified.

The mineralogical composition of the 4 core samples analyzed from the YG sample group is dominated by quartz (52-76%; average 60%), with lesser amounts of feldspar (6-26%; average 16%), clay minerals (6-12%; average 9%, mica/illite only), carbonates (0.5-3%; average 2%), pyrite (2-7%; average 5%), phosphates (0-25%, *only present in 1 sample*) and natrolite (1-4%; average 2%). Feldspars are comprised of albite (2-5%; average 3%) and orthoclase (3-21%; average 12%). Carbonates are comprised of calcite (0.5-2%) and dolomite (0-1%, *only present in 2 samples*). TOC content ranges from 7.08-14.06 wt-%, with an average of 10.20 wt-% (*only 3 of the 4 YG group samples were tested for TOC*).

The quantitative mineralogy is tabulated in **Table 5** and a Ternary Diagram for the relative proportion of quartz, calcite and clay content is provided in **Figure 3**. The YG group samples plot close to the quartz-clay end line near the quartz end member.

## Sample Selection and Technique Introduction

X-ray diffraction (XRD) analyses of 4 core samples from the Chevron Core Project were carried out in order to determine and quantify the mineralogical composition. This report summarizes the methods and analytical results. XRD is generally the fastest and most reliable method used in the identification and quantification of crystalline materials. The technique utilizes the diffraction (reflection) of x-rays from the unique arrangement of atoms in a crystal structure. The technique is particularly useful for materials with grain sizes too small for microscopic identification (i.e. clay minerals, soils minerals, dusts etc.). The XRD trace data was analyzed by Rietveld methods to quantify the mineralogy. Details of the analysis, samples preparation, methods and data plots are provided in **Appendix C**.

An example X-ray diffraction trace pattern with mineral identification is provided in **Appendix C** as Figure C1. Mineral comparison plots are provided as Figure C2.

**Table 4.** Mineralogy of the four YG core samples.

Chevron Outcrop Project YG Sample Data															
Sample Group	Sample ID	Quartz	Feldspar		Carbonates		Clays	Phosphates		Sulphides	Zeolites	TOC	Total Felds	Total Carbs	Total Phosphates
		Quartz	Albite	Orthoclase	Calcite	Dolomite	Mica/Illite*	Apatite	Hydroxylapatite	Pyrite	Natrolite				
YG	FX60 72	76.0	2.7	9.8	1.6		5.7			2.4	1.8	7.08	12.5	1.6	
	FX67 18A	51.6	4.8	20.9	0.5		12.0			6.4	3.8	9.46	25.7	0.5	
	FX67 18B	55.7	2.4	3.2	1.5	1.1	6.2	25.1	0.1	4.0	0.8		5.6	2.6	25.2
	FX73 70	57.6	3.4	15.8	1.3	1.2	11.1			7.2	2.3	14.06	19.2	2.5	

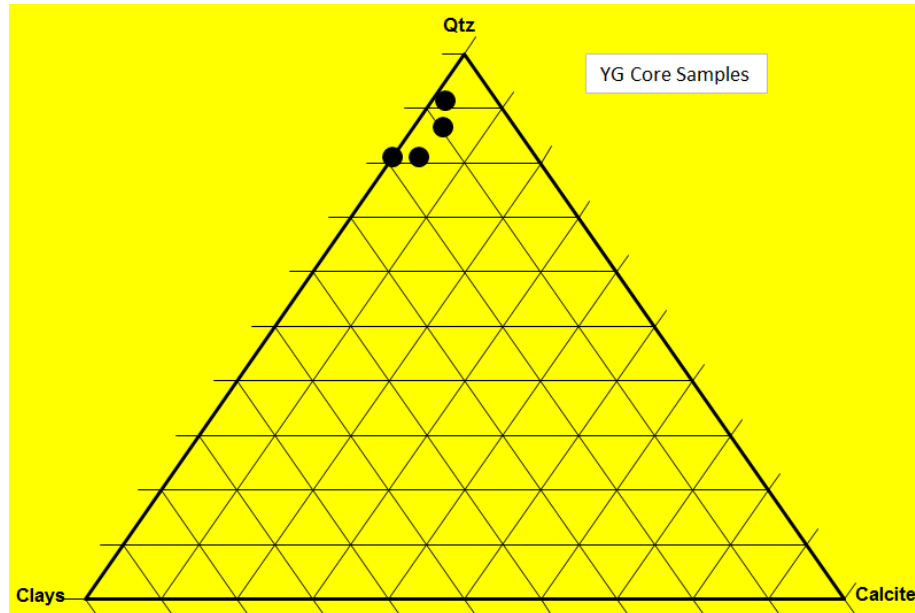


**Figure 3.** A quartz-carbonate-clay ternary diagram for YG core samples showing relative proportion of three components.

## UNCONFINED POROSITY AND MATRIX PERMEABILITY

**No. of Samples Analyzed:** 3  
**Sample Type:** core samples  
**Analyses Completed:** unconfined porosity and matrix permeability  
**Gas Used for Analyses:** helium

### *Summary of Findings:*

Porosity and matrix permeability were determined on 3 core samples from the Chevron Project. The porosity measured and reported is based on oven drying of the samples for 36 hours to ensure all samples are close to the same moisture conditions when analyzed.

Average porosity of the YG core is 9.02 %. Matrix permeability average for the core samples from YG is 1.34E-04 md. There is a positive relationship between porosity and matrix permeability for the samples from this project.

### *Sample Selection and Preparation*

Employing a variety of laboratory apparatus, density and matrix permeability analyses were conducted on 3 core samples from the Chevron Project. All tests were performed under ambient (unconfined) conditions with helium gas.

This report describes Trican Geological Solutions' experimental setup and test results.

On receipt in the lab, the samples were split for several analyses including, but not limited to, porosity, permeability, XRD, and SRA. A representative 5 gram sub sample was taken from each sample to measure bulk density via mercury immersion and a 20 gram porosity sample was crushed and sieved with a 10 mesh screen (particle size 1.7 mm and smaller). The porosity and bulk density samples were oven dried for 36 hours to ensure all samples were at similar moisture conditions for the analysis. Skeletal density, a component of porosity calculation, was measured on the dried, crushed sample in a helium pycnometer. Matrix permeability was measured on a uniform sized fraction of the crushed sample, sieved between 20 and 35 mesh screens (average particle size 0.67 mm) using the late time pressure decay data from a helium pycnometer (ResTech 1996). Measurements and calculations for porosity are based upon GRI standards (API 40 Recommended Core Practices: Section 5 – Porosity Determination) and protocol. A detailed explanation of the methods and experimental setup used is provided in **Appendix D**.

### *Results and Interpretation*

The unconfined porosity and matrix permeability were calculated on all 3 samples and are summarized in **Table 6**. The average values of the porosity, permeability and densities are included in the table for comparative purposes. Matrix permeability is reported in millidarcies (1.0 E-03 md = 1000 nd).

**Table 6.** Unconfined porosity and matrix permeability results from helium pycnometer and mercury immersion on samples.

Chevron Outcrop Project Unconfined Porosity and Permeability									
Well	Sample No.	Sample Type	Bulk Density (g/cc)		Skeletal Density (g/cc)		Porosity (%)	Matrix Permeability (md)	
			Avg	Std Dev	Avg	Std Dev		Avg	Std Dev
YG-Core	FX-60.72	Core	2.38	0.0037	2.69	0.0230	11.53	2.44E-04	6.14E-05
	FX-67.18 A	Core	2.45	0.0023	2.63	0.0109	6.75	5.46E-05	1.51E-05
	FX-73.7	Core	2.37	0.0019	2.60	0.0099	8.77	1.04E-04	2.61E-05

As shown, bulk density ranges from 2.37 g/cc to 2.45 g/cc. Porosity of the samples ranges from 6.75 % – 11.53 % with an average porosity of 9.01 %. Matrix permeability ranges from 5.46E-05 – 2.44E-04 md. In **Figure 4**, the matrix permeability of the samples is plotted against porosity and a positive relationship can be seen.

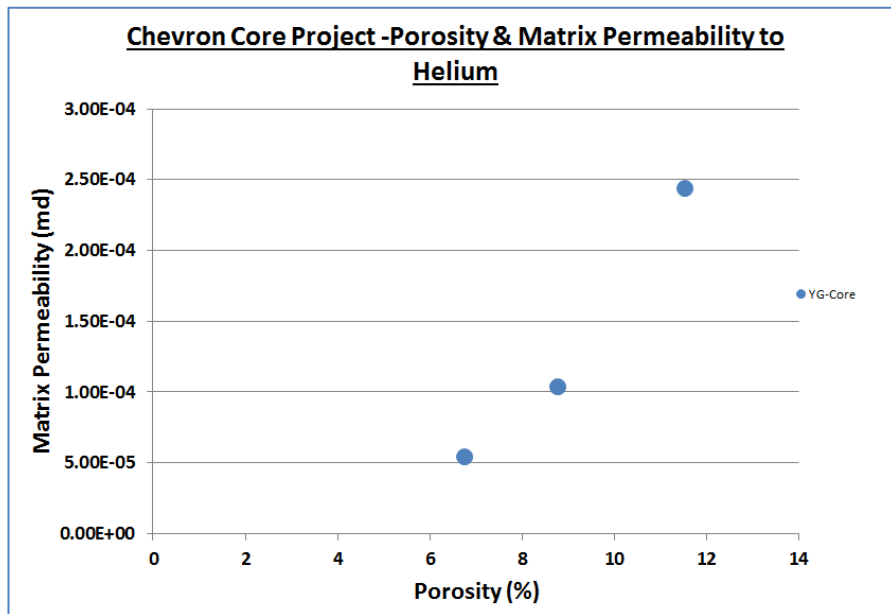


**Figure 4.** Relationship between matrix permeability and porosity to helium from the Chevron project.

## PORE SIZE DISTRIBUTION AND TOTAL POROSITY BY MERCURY POROSIMETRY

**No. of Samples Analyzed:** 3  
**Sample Type:** core samples  
**Analyses Completed:** mercury porosimetry

### *Summary of Findings:*

A series of samples from the Chevron Project were analyzed by mercury injection capillary pressure (MICP) to better understand the pore system in these shales and tight rocks. Mercury porosimetry analyses of 3 core samples from the Chevron Project were carried out in order to determine the pore size distribution and total porosity.

MICP methodologies have long been utilized to investigate reservoir rocks and particularly the relationship between pore volumes and pore throat size distribution. The details of the methodologies for reservoir rock analyses and used in this study are described in API (1998). Background information is provided in **Appendix E**. The application of MICP to shales has not been documented in the literature apart from published studies on the application of the techniques to analyses of petroleum cap rocks. The utility and extension of the MICP to shale studies must be done with caution. MICP is of necessity performed on dried samples whereas in most shales free moisture and clay bound water occurs and drying the samples may thus enhance the porosity by dissection of the samples and distort or destroy the pore fabric which is being investigated. If the samples are highly mature and at a reservoir temperature > 100°C and contain little free or bound water, the results of MICP reported are considered valid; however, there is no independent method to confirm the validity of the results. During experiments, Hg intrusion even at the highest pressures is limited to pore throats greater than about 3 nm. In many types of shale pore throats less than 3 nm occur and hence some porosity is not accessible to Hg.

Mercury porosimetry is based on the capillary law governing liquid penetration into small pores. Mercury porosimetry relies on the injection of mercury into a prepared sample at increasing pressure steps (up to 60,000 PSIA). The technique is capable of directly measuring pore volume by forcing mercury into the pore space. The technique is also capable of directly measuring pore diameters in the range of 3 to 360000 nm. Using the Washburn equation (defined below), the pore size distribution is determined. The use of the Washburn equation relies on the use of a non-wetting liquid (mercury) and the assumption of cylindrical pores. Despite the fact that pore systems are generally not cylindrical, mercury porosimetry has been accepted as a practical and reliable method for quantifying pore size distributions.

### Sample Selection and Preparation:

Selected samples are processed in a jaw-crusher and sieved to a uniform size fraction of 2-4 mm before being dried in a vacuum oven at 150°C for 24 hours to remove any liquids and volatiles. After drying, samples are weighed and recorded. Dried and evacuated samples are loaded into an appropriate size penetrometer, sealed and placed into a Micromeritics Autopore IV 9520 mercury porosimeter. A 5cc solid sample penetrometer was used for testing. Mercury is intruded into the sample at increasing pressure steps up to 60,000 PSIA. The volume of mercury intruded is measured as a function of the applied pressure.

Pore diameters are determined based on the Washburn equation:

$$D = - \left[ \frac{1}{P} \right] 4\gamma \cos\phi$$

Where D = pore diameter, P = applied pressure,  $\gamma$  = surface tension and  $\phi$  = contact angle.

Triple distilled mercury is used to ensure optimum test conditions and consistent physical properties. Testing under these conditions assumes a mercury surface tension of 485 dynes/cm and a contact angle of 130°.

### Results and Interpretation:

The results of the mercury intrusion analyses are provided in the following pages. The pore size distribution is displayed graphically in the following figures.

**Table 7** displays the total porosity of each sample. It is important to note that the porosity value is a measure of the TOTAL porosity as the sample has been dried and the assumption made that pore fluids have been evacuated.

**Table 7.** Total porosity determined using mercury porosimetry

Chevron Outcrop Project Hg Porosimetry Result						
Sample ID	Sample Type	Bulk Density g/cc	Skeletal Density g/cc	Porosity %	Peak Range (nm)	
					Peak Range	Modal Peak
FX-60.72	Core	2.4325	2.5409	4.27	<3.0 - 15	6.5
FX-67.18	Core	2.3583	2.4882	5.22	<3.0 - 15	7.0
FX-73.7	Core	2.3698	2.4922	4.91	<3.0 - 12	5.5

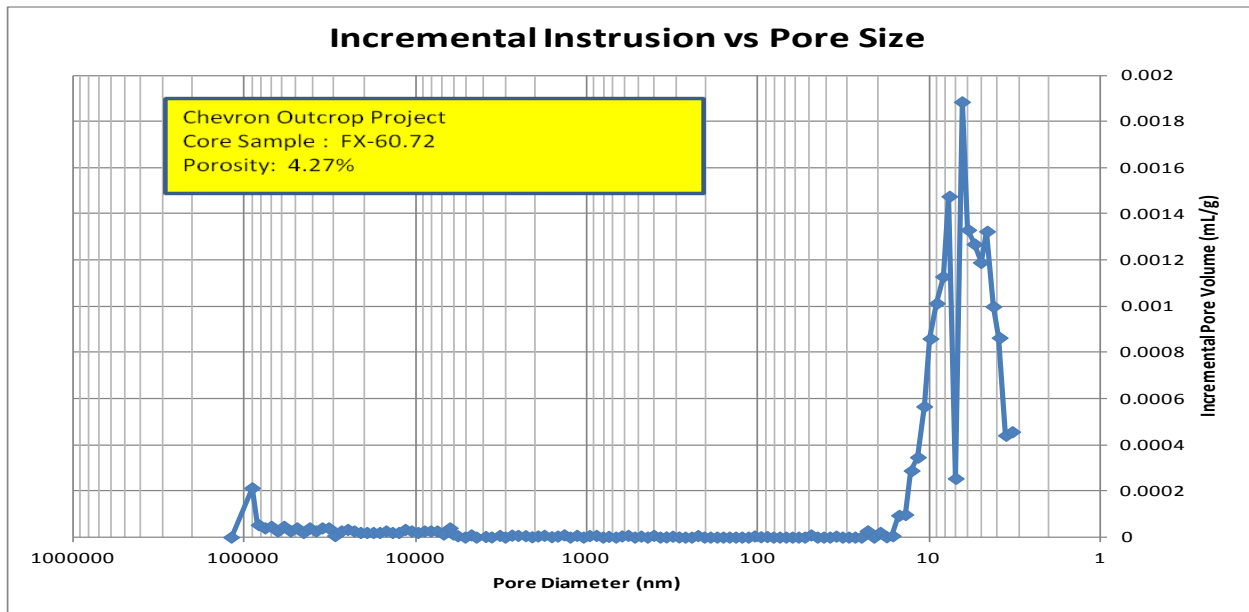


**Figure 5.** Pore size distribution for FX-60.72

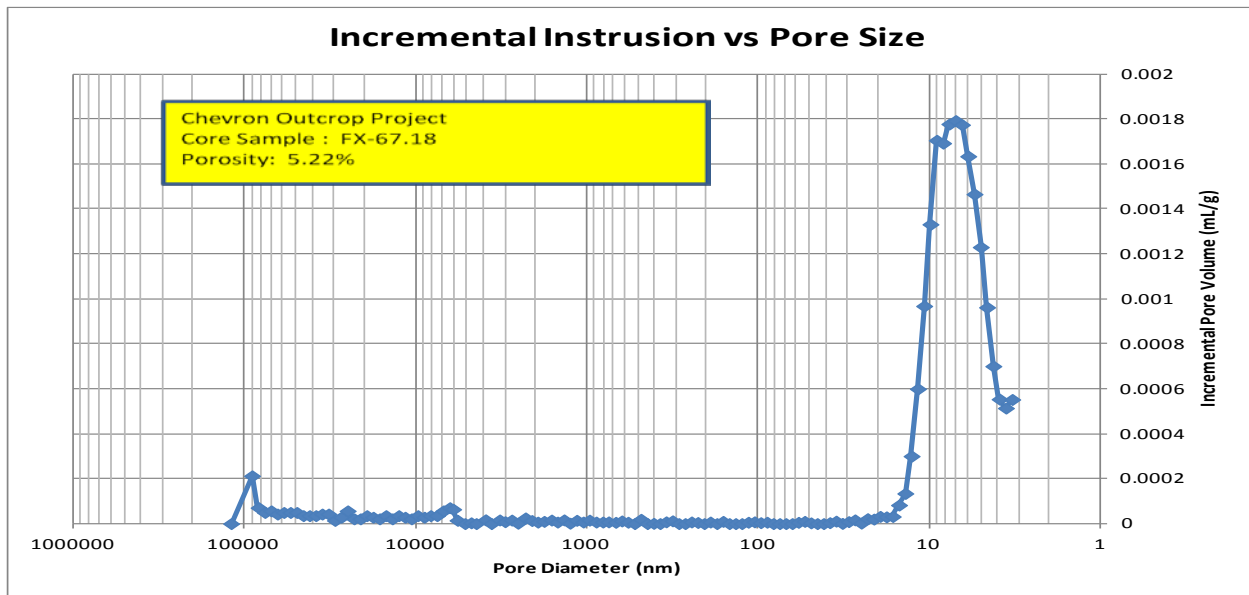


**Figure 6.** Pore size distribution for FX-67.18

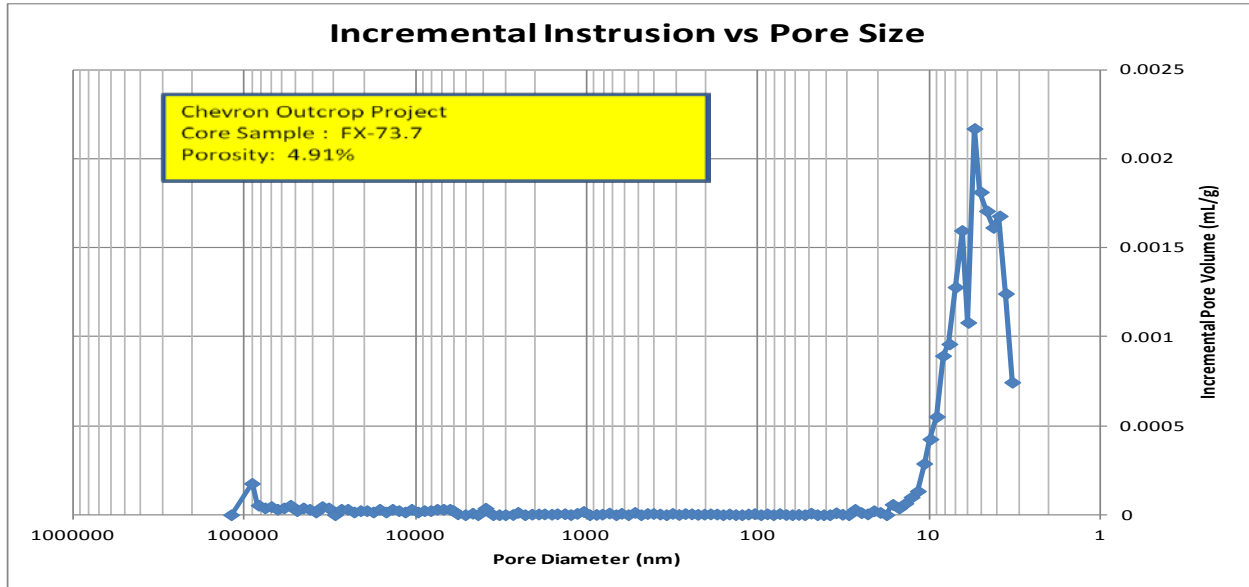


**Figure 7.** Pore size distribution for FX-73.7

## PETROGRAPHIC AND SEM DESCRIPTIONS

<b>Formation:</b>	Canol Formation
<b>Samples Analyzed:</b>	2 (petrography), 4 (SEM)
<b>Sample Type:</b>	core samples
<b>Analyses Completed:</b>	inorganic petrography and scanning electron microscopy (SEM)

### *Summary of Findings:*

Petrographic and scanning electron microscopy (SEM) analyses for 3 samples of the Chevron Core Project from the Canol Formation were performed in order to better understand textural and compositional variability (or homogeneity). Pore structures and diagenetic overprints were also investigated. All samples show characteristics of fissile, finely laminated organic-rich siliceous shales/mudstones. The investigations revealed that most of the samples contain high amounts of diagenetic quartz derived most likely from biogenic silica of phytoplankton debris. **Table 8** shows a summary of all rock samples with main characteristics. Both XRD data and petrographic/SEM data were incorporated.

The FX samples are black organic-rich (up to 14 wt-% TOC) shales/mudstones with 50-90% quartz and feldspars and clay minerals (mica, illite). Trace amounts of carbonates are also present. These rocks are very fine-grained (mostly <10 µm) with some silt-size grains of mica, feldspars, pyrite, quartz and carbonates (dolomite, calcite). Quartz permeates the entire sample and forms idiomorphic microcrystalline grains (0.5-3 µm) but also occurs as cements between grains and organic material (incl. bitumen). Some thin beds can exhibit a “silty appearance” which makes the rock samples look like siltstones (sample FX-67.18) but SEM analysis reveal that the “silty” grains are recrystallized microfossils (possibly tasmanite or dasycladacean cysts). The cements are dominated by quartz but carbonate material is also found along the margins (overgrowth- secondary diagenetic growth). Algal remains are the dominant component of the organic matter. Several other microfossils are occasionally observed including possible planktonic radiolarian, gastropods, pteropods. Most algal remains show replacement by quartz but mica and pyrite can also be observed within their structures together with abundant either dispersed or solid bituminous material. The paleoenvironmental setting of these samples may have been a shallow marine basin with restricted detrital influx (distal to the shoreline) and anoxic bottom water conditions. Detrital influx of feldspars, quartz, and mica occurred but only medium to fine silt-size particles (except for mica sheets) were transported and deposited at the location. Minimal bottom water currents disturbed the sediments resulting in these laminated shales/mudstone rocks.

In summary, these samples provide information about their origin and depositional settings. The high quartz and algal content of the samples together with the limited detrital component infers that these samples were deposited within a shallow marine basin with restricted detrital influx and highly stratified ocean where the bottom water was calm and anoxic due to the constant influx of organic matter. No bioturbation is evident in any of these rock samples. Some thin beds

with high amounts of plankton material are present but there is little evidence that prolific algal blooms similar to modern upwelling settings occurred. In contrary, normal algal growth appears to have been the norm in the past during the deposition of these sediments. During early diagenesis, dolomite and pyrite formation occurred, followed by burial and late diagenesis, resulting in silicification and microfossil replacements, as well as organic maturation and migration of certain HC fractions.



**Table 8.** Summary of all rock samples with main characteristics. Both XRD data and petrographic/SEM data were incorporated.

Sample	Minerals, organics, pores (%)						Organic matter	Algal material	Recrystallized microfossils	Additional comments
	quartz	carbs	clay mins	sulph	TOC	pore space				
<b>FX-67.18a</b> <i>SEM only</i>	50-60%	5-7%	10-15%	<5%	9.46	<2%	very fine, porous bituminous organic matter dispersed throughout;	no evidence in SEM analysis	no evidence in SEM analysis	abundant albite and orthoclase; granular matrix texture due to abundance of neofomed microcrystalline quartz grains
<b>FX-67.18b</b> <i>SEM only</i>	50-60%	10-15%	5-10%	<5%	/	<2%	stringers/lenses of solid bitumen, solid bitumen filling void space	no evidence in SEM analysis	repl. by quartz & calcite	25% apatite detected XRD but none by visual analysis (SEM/BSE); hand sample surface featured particles of organic matter possible planktonic microfossils
<b>FX-67.18c</b> <i>TS &amp; SEM</i>	70-85%	2-3%	<5%	<5%	/	<2%	very fine, porous bituminous organic matter dispersed throughout;	algal cysts	repl. by quartz & sphalerite	ubiquitous silt-sand size algal cysts composed of <b>sphalerite (ZnS)</b>
	60-70%	<1-2%	<5%	<5%	/		very fine, porous bituminous organic matter dispersed throughout; solid bitumen filling void space	silicified lenticular algal remains	repl. by qtz	<b>barite</b> micro crystals and <b>sphalerite</b> cements
<b>FX-73.7</b> <i>SEM only</i>	60-70%	2-3%	5-10%	5-10%	14.06	<2%	vf porous bituminous organic matter dispersed throughout;	no evidence in SEM analysis	possible quartz replaced microfossil of algal origin	granular matrix texture due to abundant neofomed microcrystalline quartz grains;

## *Sample Selection and Preparation*

Thin sections of 3 core samples were prepared by Calgary Rocks and then examined for the *Chevron Core Project* by transmitted light microscopy. Rock chips perpendicular to the bedding plane were also prepared for Scanning Electron Microscope analysis. This report includes information concerning sedimentary composition, cementation, diagenesis, and fracture characteristics. Each sample is reported individually.

### i) Petrographic Analysis

Most of the samples showed very brittle and friable characteristics and were impregnated before sample preparation with a UV-fluorescent epoxy. Once cured, a ~30 µm thick polished thin sections was made. Half of the thin section was stained with a dual-stain (Alizarin Red S – to distinguish between calcite and dolomite, and potassium ferricyanide – to distinguish carbonate minerals containing Fe<sup>2+</sup>). The stain helps to differentiate the carbonate, feldspar and quartz grains in fine-grained rocks and affects them as follows: calcite (pink- to red-brown), Fe-rich calcite (mauve to blue), dolomite (no stain), Fe-rich dolomite (ankerite) (very pale blue, turquoise or greenish). This staining resulted in some peeling of the samples off the glass slides so the sodium cobaltinitrite (to distinguish between K and Na Feldspars) stain was not applied. That stain would affect the feldspars in the following ways: K feldspar (bright to pale yellow with an etched surface), Na feldspar (faint red to pink). The thin sections were examined in transmitted light (PPL: plain; XPL: x-polarized; and UV: UV light) and photomicrographs taken at various magnifications (40x, 100x, 200x and 400x) to document structure, porosity, organic matter, composition and nature of optically resolvable grains and matrix. An *Olympus BX51* research microscope with an EXFO (x-Cite Series 120Q) fluorescence illuminator (TRITC filter) was used for the analysis. In some cases pertinent details are more visible at low or intermediate magnifications and as such are noted.

The rock classification scheme used by Trican is summarized in **Appendix F**

### ii) Scanning Electron Microscopy Analysis

Four core samples were evaluated by SEM by Trican

A FEI Quanta 250 environmental scanning electron microscope (ESEM) was used to determine surface characteristics at micron-levels. Polished billets and fresh rock chips from the samples were selected for the analysis. The polished billets and chip fragments were mounted on stubs and Au-coated. For elemental analysis, the attached EDS (Energy Dispersive Spectroscopy) System was utilized, which is an EDAX system containing an SDD (silicon drift detector).

In scanning electron microscopy, an electron beam is scanned across a sample's surface. When the electrons strike the sample, a variety of signals are generated and it is the detection of specific signals which produces an image or a sample's elemental composition. The three signals which provide the greatest amount of information in SEM are the secondary electrons (SE), backscattered electrons (BSE) and X-rays (EDS).

Secondary electrons are emitted from the atoms occupying the top surface and produce a readily interpretable image of the surface. The contrast in the image is determined by the sample morphology. A high resolution image can be obtained because of the small diameter of the primary electron beam.

Backscattered electrons are primary beam electrons which are 'reflected' from atoms in the solid. The contrast in the image produced is determined by the atomic number of the elements in the sample. The image will therefore show the distribution of different chemical phases in the sample. Because electrons are emitted from a depth in the sample, the resolution in the image is not as clear as for secondary electrons.

Interaction of the primary beam with atoms in the sample causes shell transitions which result in the emission of an X-ray. The emitted X-ray has an energy characteristic of the parent element. Detection and measurement of the energy permits elemental analysis (Energy Dispersive X-ray Spectroscopy or EDS). EDS can provide rapid qualitative, or with adequate standards, quantitative analysis of elemental composition with a sampling depth of 1-2 microns. X-rays may also be used to form maps or line profiles, showing the elemental distribution of a sample surface.

## *Results and Interpretation*

### SAMPLE FX-60.72

---

An overview image below (Figure 8) shows a scan of the sample thin section under two different light conditions (standard scan and open cover) in order to show the natural texture visible in thin section. The overview reveals a dark, fine grained sedimentary rock with very fine laminations. The dark colour is the result of elevated concentrations of organic matter.



**Figure 8.** Thin Section of sample FX-60.72 under standard scan (left) and overexposed light (right) revealing subtle lamination within an organic-rich mudstone/shale.

The mineralogical composition of **sample FX-60.72** determined by X-ray diffraction techniques is comprised of mainly quartz (76%), with lesser amounts of feldspar (13%), mica/illite (6%), calcite (2%). The remaining 5% is comprised of small amounts of pyrite and natrolite (zeolite). Total organic carbon content of the sample is very high at 7.08 wt-%.

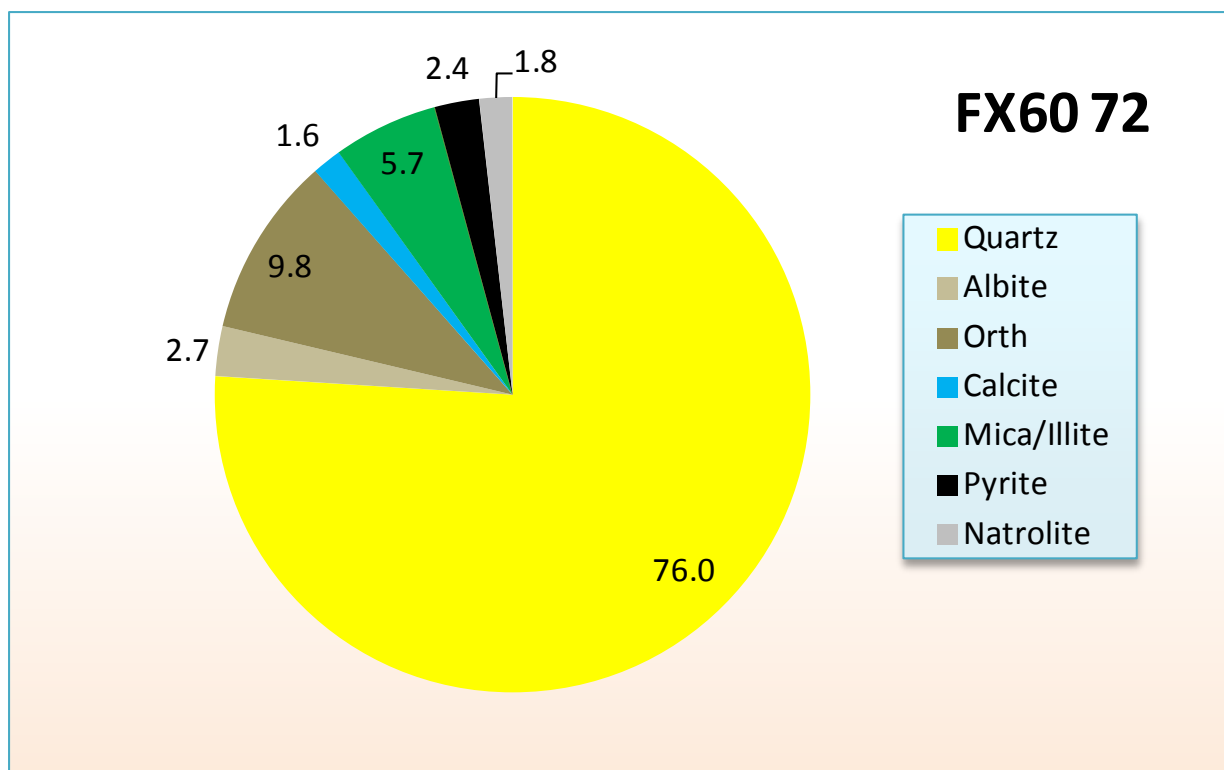


**Figure 9.** Pie-diagram of the mineralogical composition of sample FX-60.72 determined by XRD analysis. This composition is dominated by quartz, with lesser amounts of feldspar and mica/illite.

---

## THIN SECTION ANALYSIS

---

**OVERVIEW** *Sample FX-60.72* is an organic-rich black mudstone/shale, where the fine-grained nature of the sample is obscured by abundant opaque organic matter. Subtle lamination is defined by discontinuous lenses and stringers of silicified algal remains. In addition, the matrix contains clusters of quartz recrystallized microfossils, authigenic quartz and carbonate cements, and mica lathes embedded mostly parallel to the bedding.

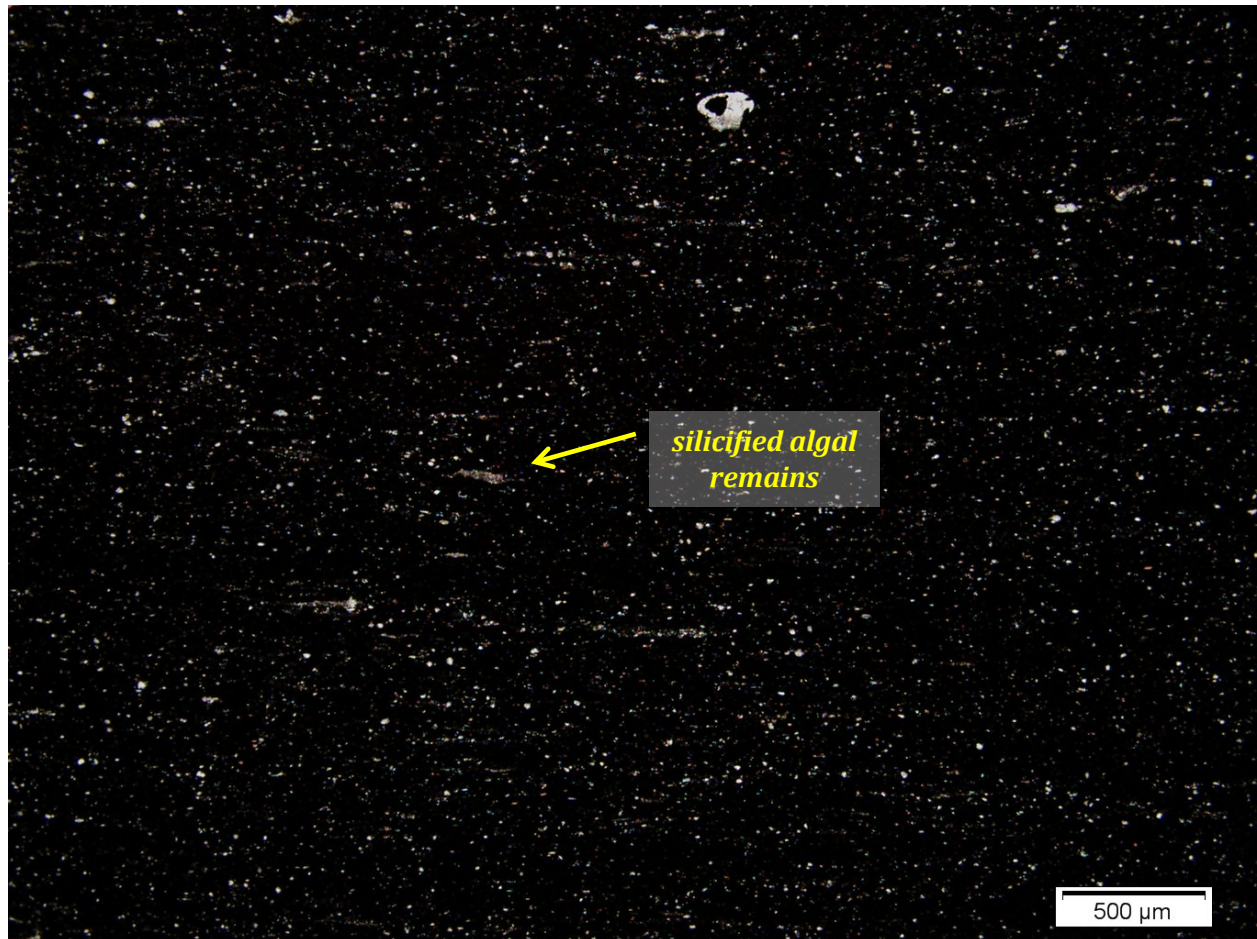


**Figure 10.** Photomicrograph in PPL showing subtle algal laminae within a dark organic-rich matrix of sample FX-60.72. Bright grains are primarily comprised of authigenic quartz and represent former microfossils. See **Figure 11** below for magnification of bioclast at top of image.

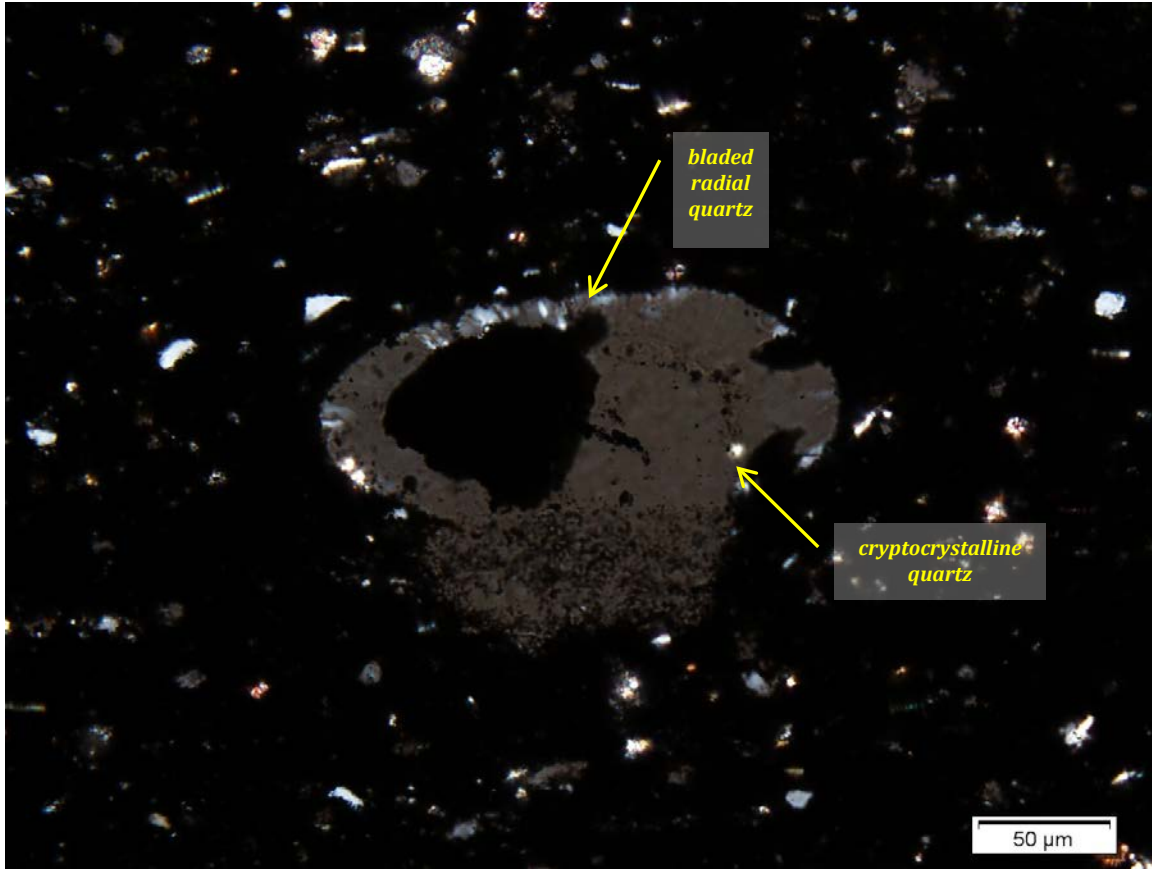


**Figure 11.** Photomicrograph in XPL showing large recrystallized microfossil with opaque (organics or pyrite) inclusion. Extinction reveals bladed radial quartz cements on upper edge, and some carbonate cements also on left edge. The rest of the grain is cemented by cryptocrystalline quartz. Note abundant quartz grains pseudomorph after dolomite and mica sheets (often <math><15\ \mu\text{m}</math>) within matrix.

**FRAMEWORK** The primary framework constituent is composed of quartz. Quartz grains are observed as silicified algal remains, recrystallized microfossils, and angular cemented grains. Silicified algal laminae have an average length of 80-250  $\mu\text{m}$ , but may be up to 600  $\mu\text{m}$ , and thickness of 10-40  $\mu\text{m}$ . The former algal clusters contain quartz grains, calcite, and mica sheets, bound together by microcrystalline quartz, fine clay minerals, and organic matter.

The sample also contains rounded to sub-rounded microfossils with recrystallized quartz ranging in size from 5-40  $\mu\text{m}$ , with one exception of a bioclast at 200  $\mu\text{m}$  size (Figure 11). Some recrystallized microfossils are composed of microcrystalline quartz that features inclusions and/or thin rims of carbonate (e.g. 2-4  $\mu\text{m}$  inclusions in a 20  $\mu\text{m}$  grain) and/or opaque (organics and sulfides) material. The sample also contains angular monocrystalline quartz cement grains (average 5-15  $\mu\text{m}$ , up to 30  $\mu\text{m}$ ) that sometimes feature concave grain boundaries. Frequently these microfossils/grains are clustered and/or included in algal mats that are held together by microcrystalline quartz overgrowth cements. Common quartz pseudomorphs after dolomite are observed, ranging in size from 7-15  $\mu\text{m}$ , with quartz and/or carbonate overgrowths. Finally, the framework contains abundant mica sheets, ranging in size from 5-30  $\mu\text{m}$ .

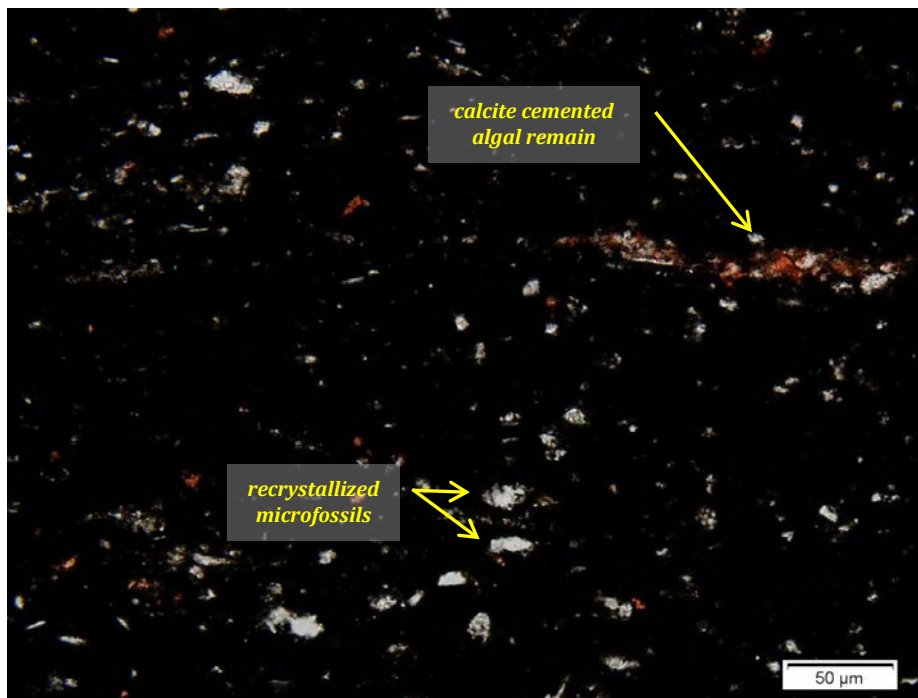


**Figure 12.** PPL photomicrograph showing calcite cemented algal remain at right of center, which also contains quartz grains and a mica sheet. Within the dark organic-rich matrix occurs other algal remains, recrystallized microfossils, quartz pseudomorphs after dolomite, mica sheets, and microcrystalline quartz and calcite cements.

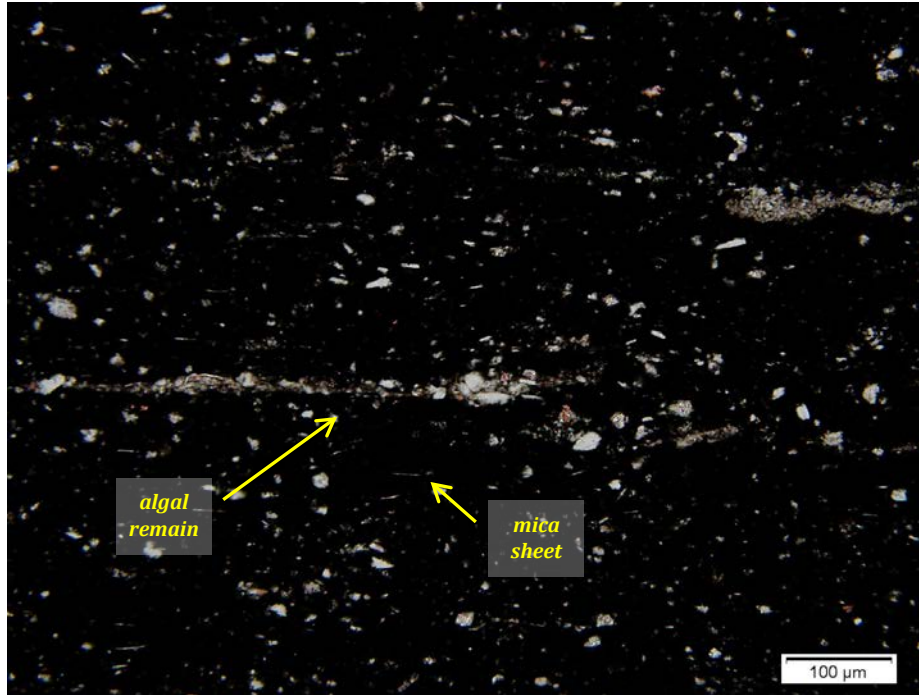


**Figure 13.** Photomicrograph in PPL showing algal remains composed of quartz grains, mica sheets bound together by quartz and carbonate cements, organic matter and fine clay minerals.

**GROUNDMASS** The fine grained nature and the high finely dispersed organic matter of this sample make interpretations and identifications of minerals phases and cements within the groundmass difficult. Using overexposed light techniques, the matrix contains clusters of microcrystalline authigenic quartz and abundant organic material with possibly some clay minerals (mica sheets are apparent in thin section). Trace amounts of feldspar are detected within the matrix, where unobscured by organics.

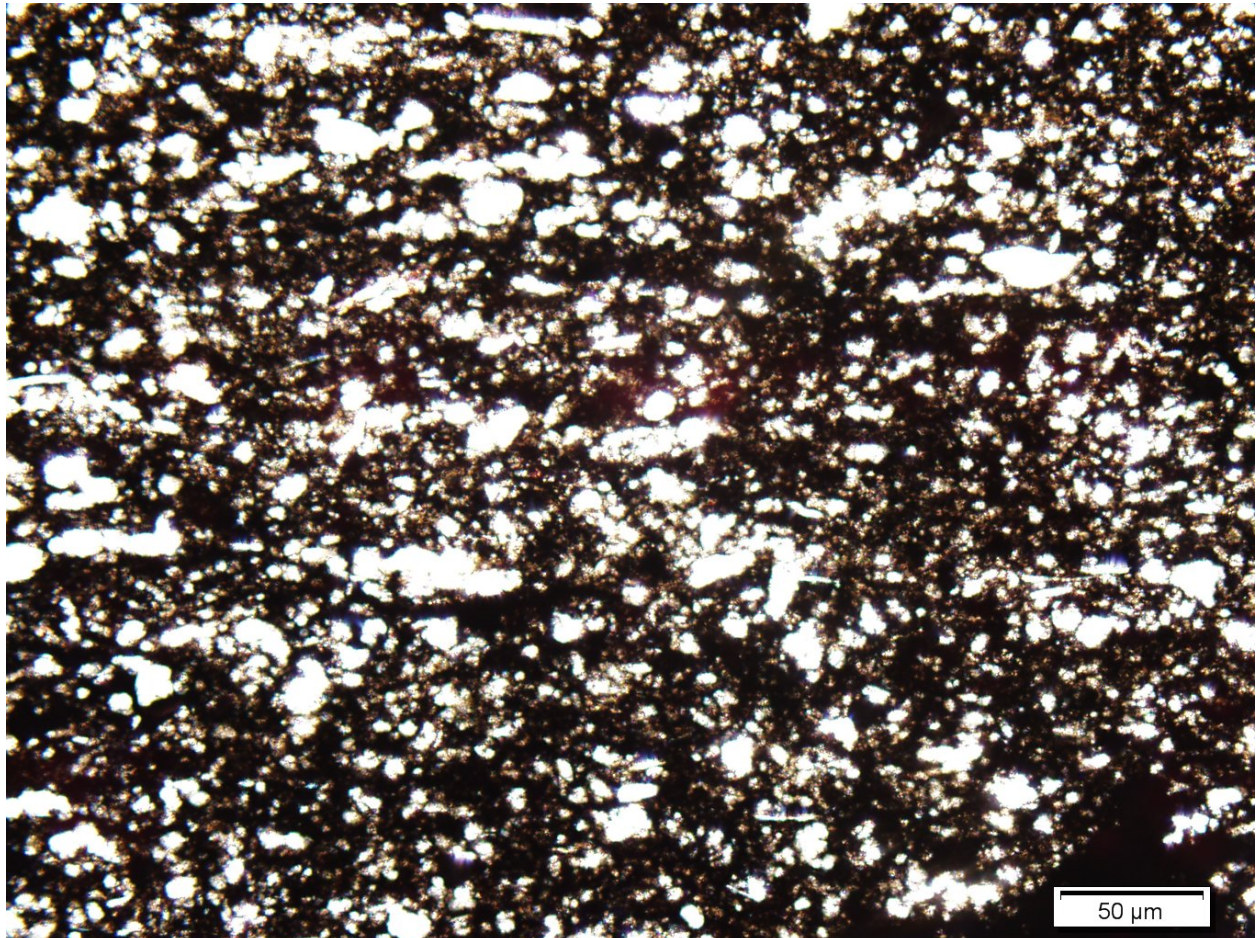


**Figure 14.** PPL overexposed photomicrograph revealing abundant silt-size microfossils and quartz grains, with ubiquitous concealing organic matter in the matrix. Silicified algal remains and bituminous stringers impart a subtle lamination within the sample. Few mica lathes (elongate sheets) are observed.

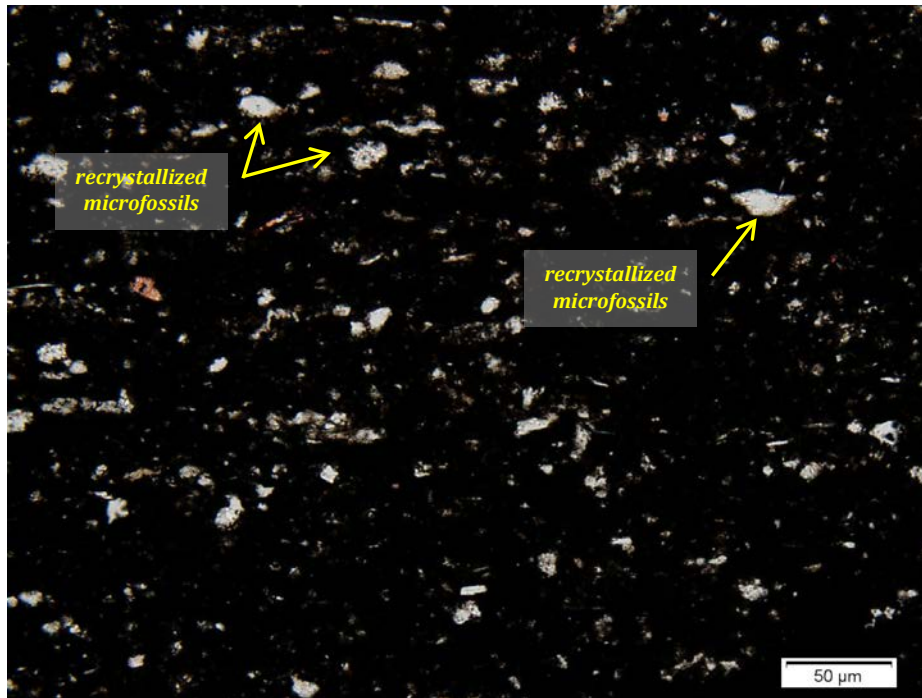


**Figure 15.** PPL photomicrograph showing abundant silt-size microfossils composed of monocrystalline and/or microcrystalline quartz, within a dark organic-rich matrix. The framework components also include some calcite grains (pink stain).

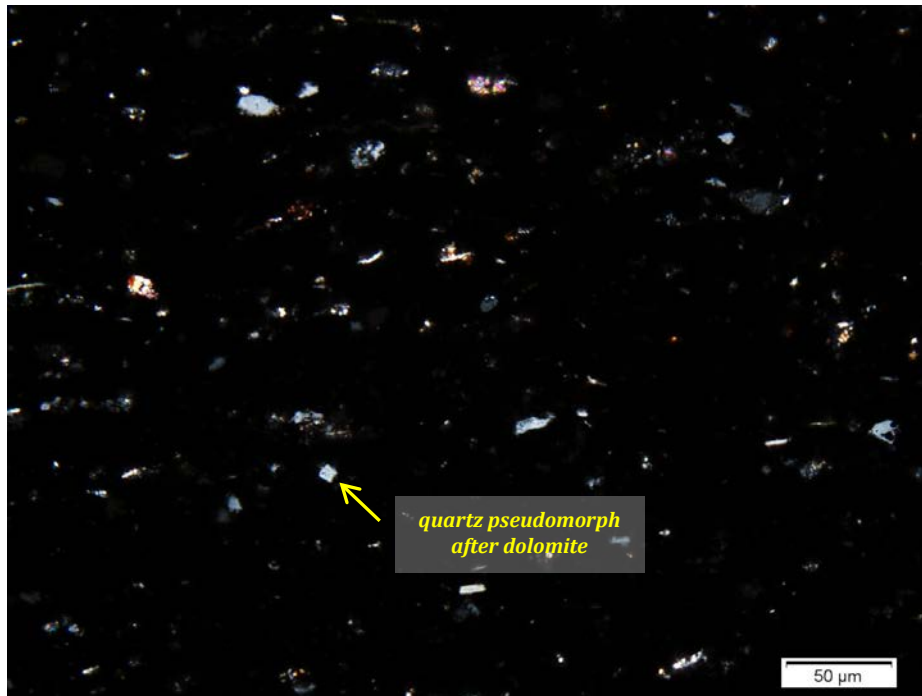


**Figure 16.** XPL photomicrograph from Figure 15 showing grey extinction of the abundant quartz grains and pleochroic extinction of the carbonates. Note quartz pseudomorph after dolomite left of centre and abundant mica sheets. Bioclast in upper right corner is replaced with mono- and microcrystalline quartz cement.

**PORE SPACE** Little pore space was observed in this thin section which may be due to the opaque nature of the abundant organic material. Overexposure under UV Light reveals some extremely fine (<1 μm) healed fractures associated with algal laminae (see **Figure 17**). Overall, porosity may be very small and possibly <2%. It is possible that abundant bituminous organics are both preserving and concealing additional pore space.

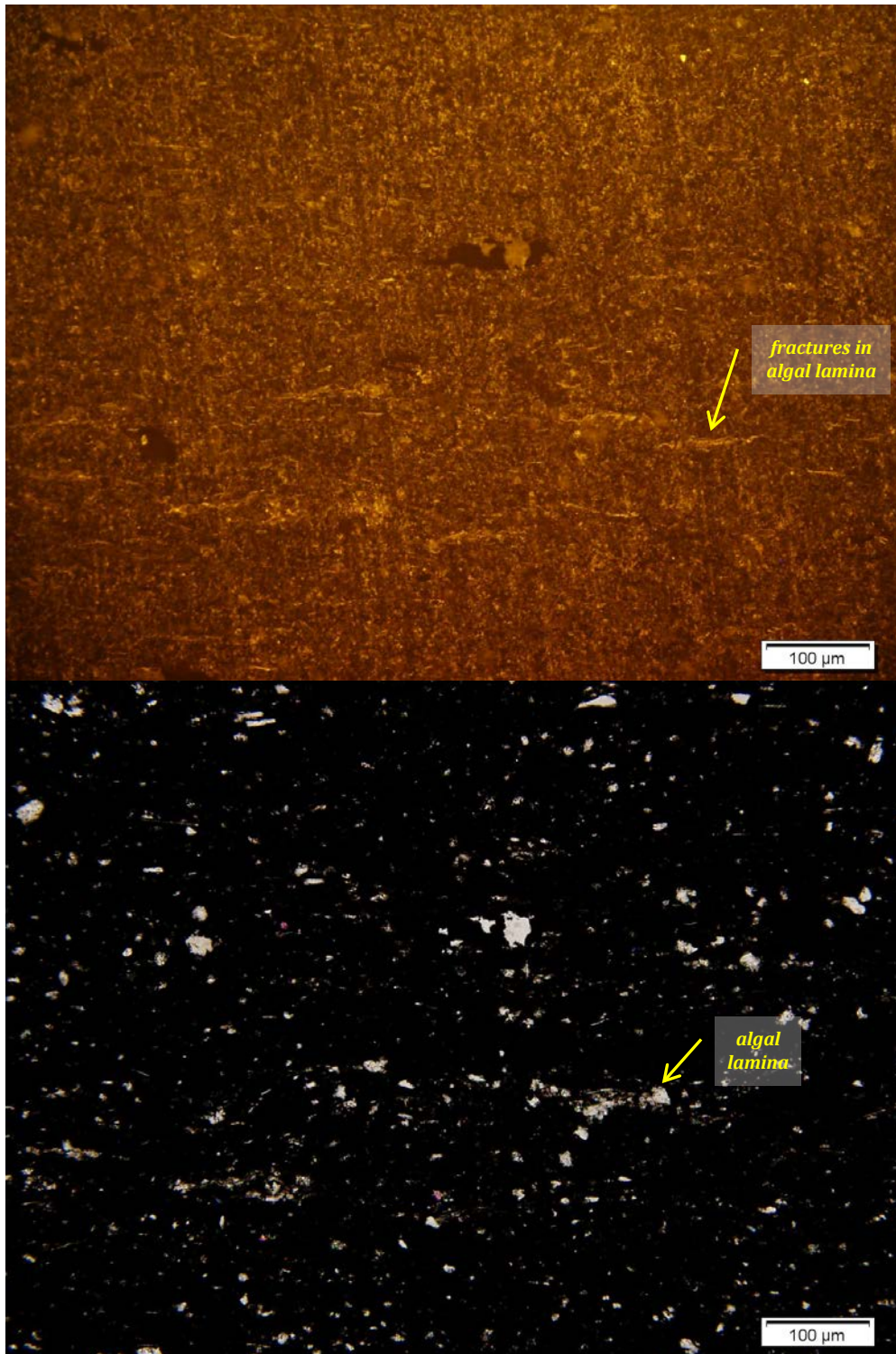


**Figure 17.** UV light overexposed (upper) and PPL (lower) photomicrographs showing extremely fine healed fractures associated with algal material, as well as some bitumen globules.

**PARAGENESIS** Deposition of organic-rich biogenic material composed of abundant algal material and algal debris. Compaction and diagenesis including neof ormation of quartz grains and cementation of bioclasts. Fluid migration and further cementation with mostly quartz and reducing porosity. Organic matter maturation. Uplift and exposure resulted in alteration (zeolites – not observed in thin section).

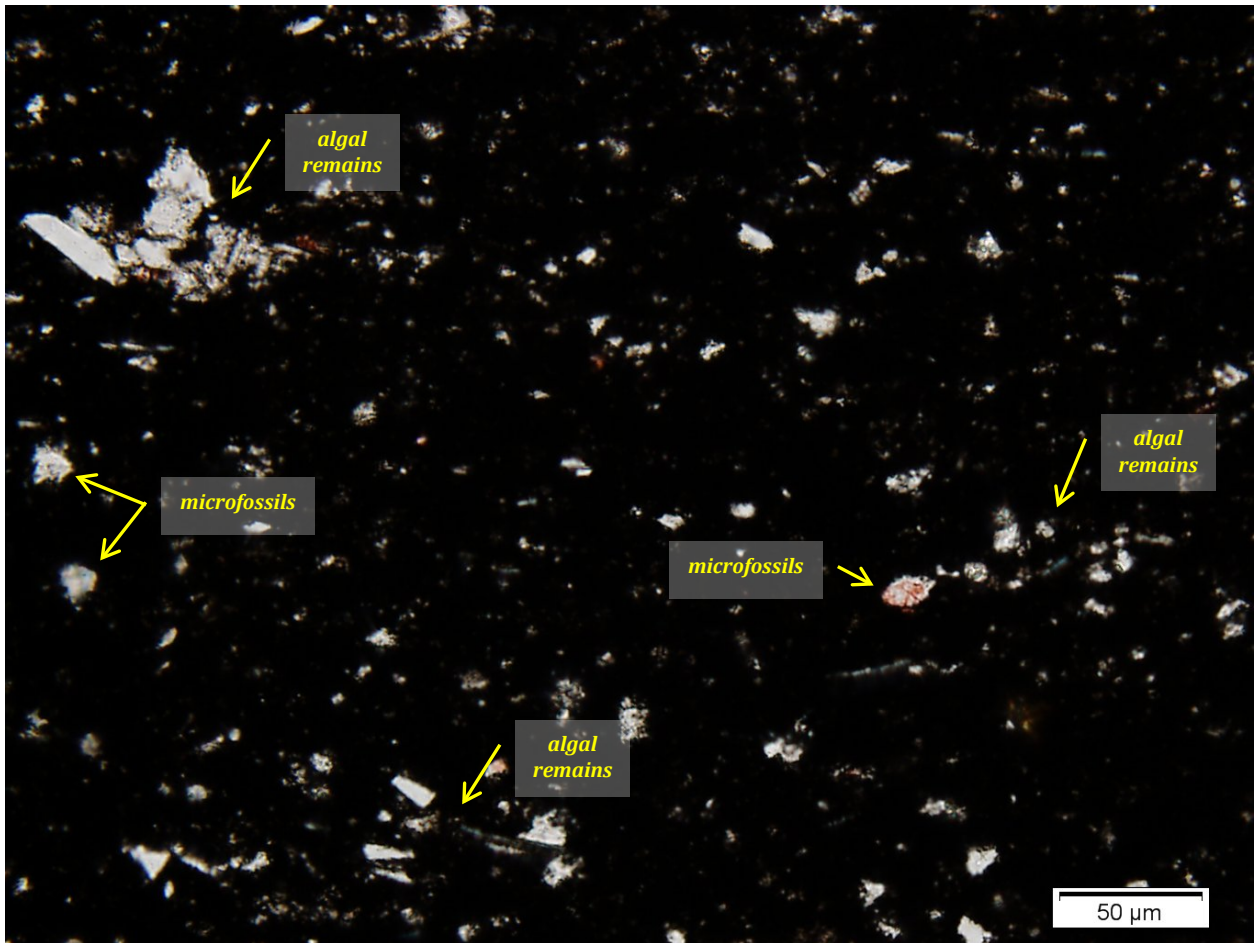


**Figure 18.** PPL photomicrograph showing clustered algal remains (yellow arrows) comprised of quartz cement grains and recrystallized microfossils, held together by microcrystalline quartz cements, fine clay minerals and organic matter. Note abundant sub spherical microfossils (blue arrows) and angular cements floating within dark organic-rich matrix.

## SAMPLE FX-67.18A

---

The mineral composition of **sample FX-67.18a** by XRD refinement is comprised of mainly quartz (52%) and feldspar (26), with lesser amounts of mica/illite (12%), pyrite (6%), and natrolite (zeolite group) (4%). Trace amounts of calcite was detected by XRD refinement. The total organic carbon content of the sample is very high at 9.46 wt-%.

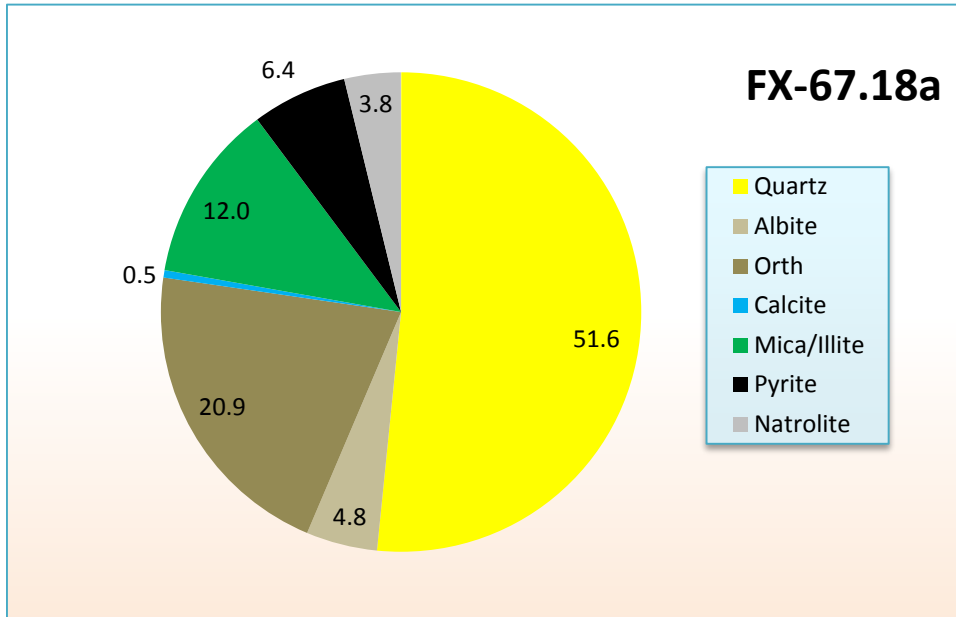


**Figure 19.** Pie-diagram of the mineralogical composition of sample FX-67.18a determined by XRD analysis. This composition is dominated by quartz and feldspar, with lesser amounts of clay minerals, pyrite, and natrolite. Only trace amounts of calcite is detected, while up to 10% calcite and dolomite is observed in sample.

Visual analysis using SEM reveals the mineralogical composition of **sample FX-67.18a** to be composed of mainly quartz (~50-60%), with abundant feldspar (20-30%), illite/mica (10-15%), carbonates (5-7%), and pyrite (up to 5%). The remainder of the sample is comprised of pyrite, fine grained clay minerals, and organic matter. Overall, visual estimation corresponds well with XRD refinement results, with the exception of increased carbonates and absence of natrolite within SEM fresh chip sample.

---

## SEM ANALYSIS

---

**OVERVIEW** SEM analysis of the fresh chip samples reveals some fine to coarse silt-sized (10-40  $\mu\text{m}$ ) quartz, feldspar, and carbonate particles; as well as mica sheets (up to 60  $\mu\text{m}$ ), embedded within a very fine silt to clay size matrix. Larger silt-size grains have smooth surfaces which imply diagenetic growth (i.e. secondary origin). Spherical recrystallized bioclasts are few and are replaced by calcite or quartz.

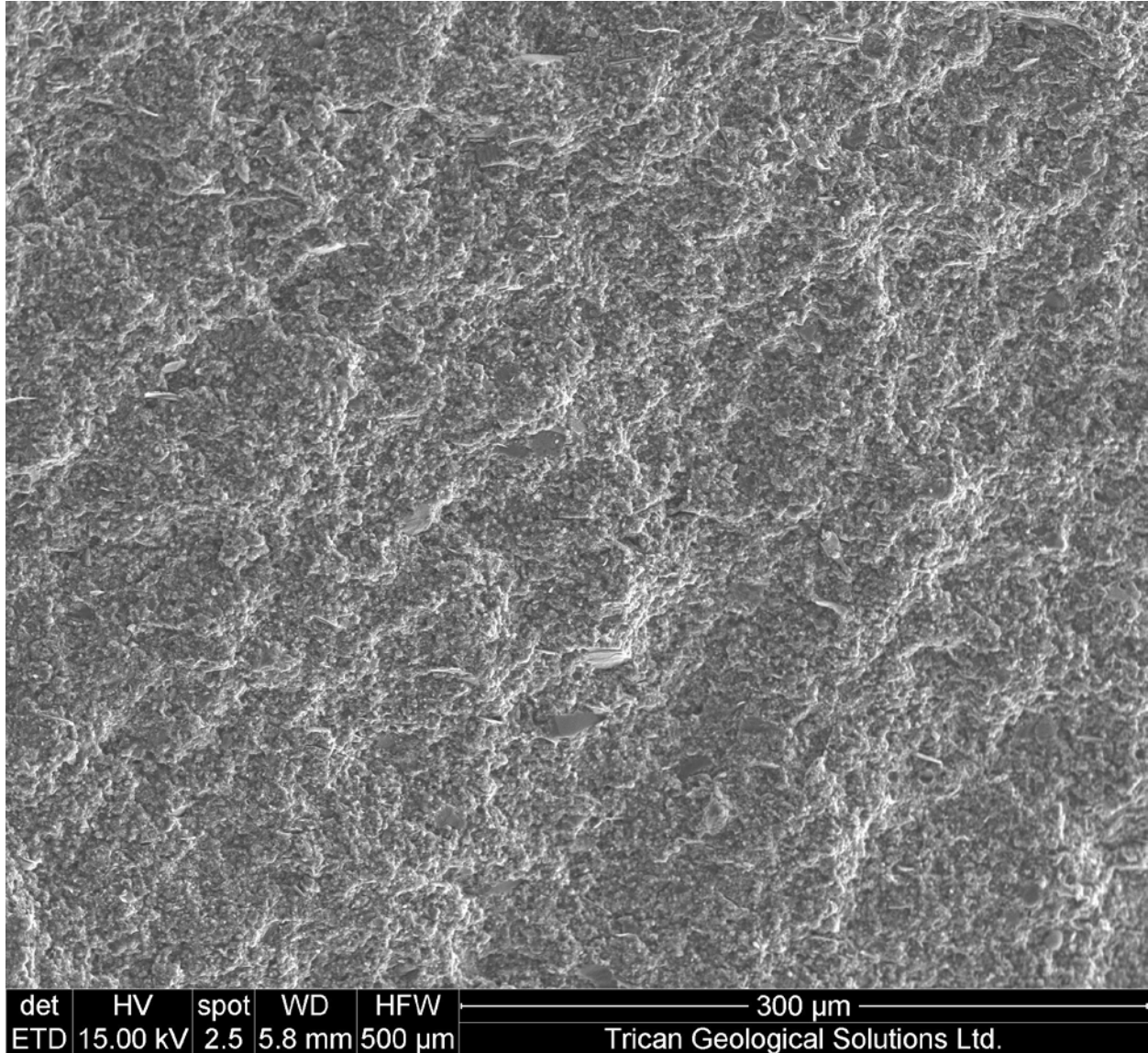


**Figure 20.** SE photomicrograph showing overview of texture and lamination within sample FX-67.18a. Sample features silt-size quartz, feldspar, carbonates, and mica grains, within very fine silt to clay-size matrix of neoformed quartz, clay minerals, and organic matter.

**FRAMEWORK** The primary framework constituent of **sample FX67.18a** is quartz, comprising approximately 50-60% of the sample volume. Quartz is observed predominately as very fine silt to clay size neformed crystals within the matrix, with lesser amounts of silt-size framework cement particles (as shown in Figure 22). This most abundant clay size neomorphic quartz is discussed further in the matrix description.

The remaining silt-sized particles include feldspar (predominately albite), carbonates (calcite and dolomite), mica, and pyrite. Albite particles dominate the silt-size component, ranging in size from 5-25  $\mu\text{m}$ , and more abundant than quartz of comparable size (majority of quartz very fine silt to clay size matrix). K-feldspar is the next most frequent framework grain forming 5-25  $\mu\text{m}$  grains. Both feldspars exhibit both blocky or anhedral habits. Dolomite rhombs are observed ranging in size from 3-20  $\mu\text{m}$  and are estimated to comprise 5-10% of the sample volume. Anhedral calcite grains are less abundant than dolomite, ranging in size from 5-10  $\mu\text{m}$  and are estimated to comprise less than 5% of the sample volume. The size of mica sheets vary widely, with the average sheet size 5-15  $\mu\text{m}$ , but ranging up to 80  $\mu\text{m}$

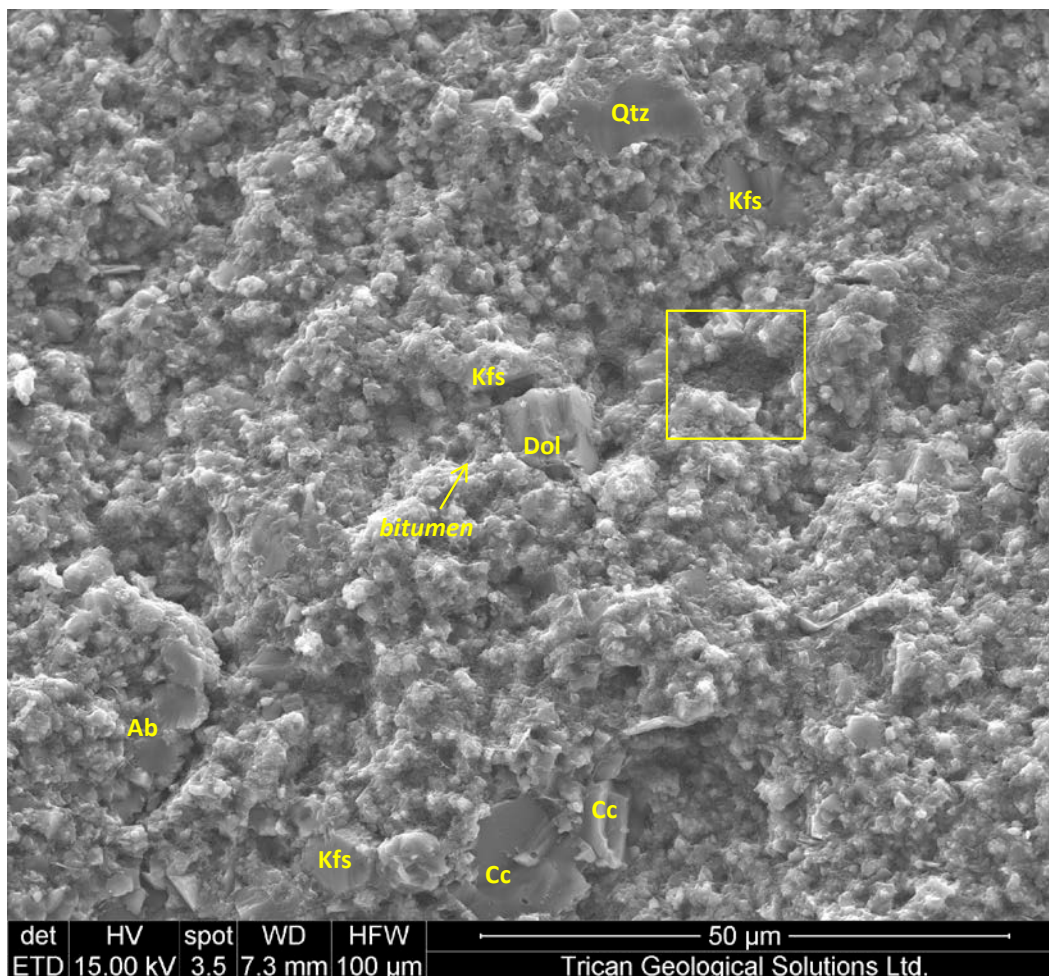


**Figure 21.** SE photomicrograph showing silt-size framework cement grains composed of feldspar, carbonates, and quartz. Note sugary texture of matrix imparted by fine silt to clay size neformed quartz crystals, organic matter, and clay minerals. Yellow box is magnified in Figure 22.

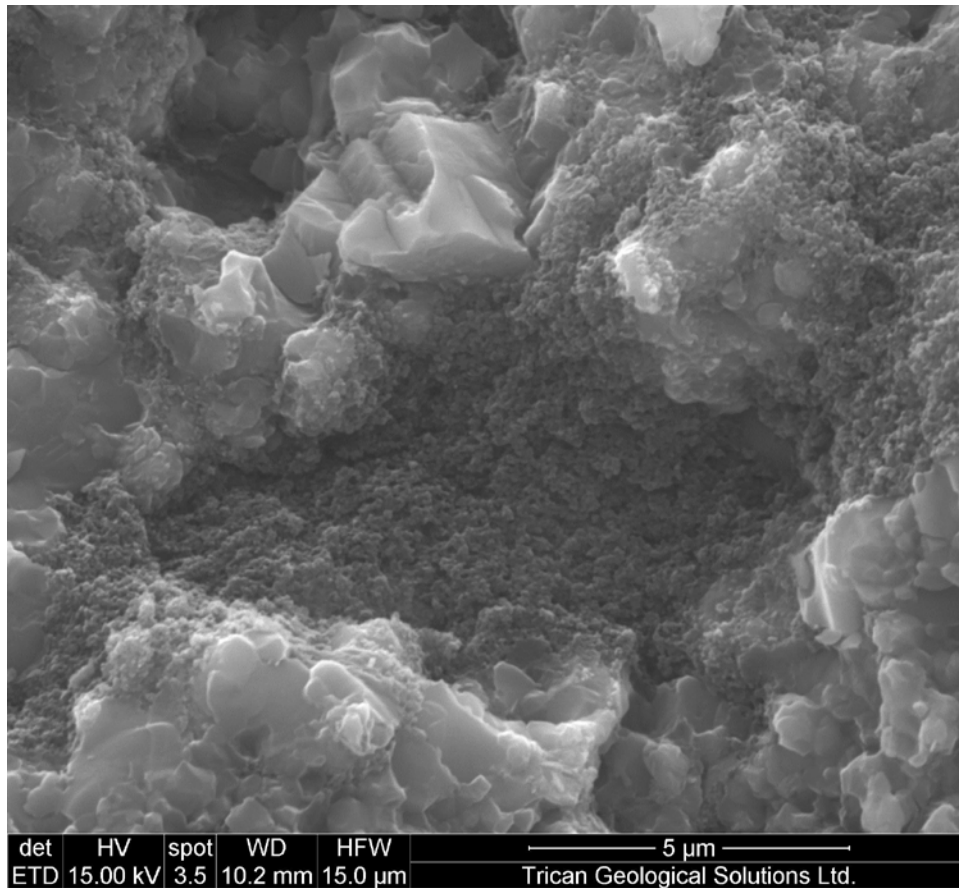


**Figure 22.** SE photomicrograph showing very fine low-density organic material lining a cavity remnant of a larger grain removed during sample prep. The cavity is surrounded by authigenic quartz cements.

**GROUNDMASS Sample FX67.18a** features silt-size grains embedded within a groundmass of clay to very fine silt-size neofomed quartz, clay minerals and bituminous organics. The ubiquitous microcrystalline quartz crystals range in size from 200 nm up to 1-2 μm. Fine grained illite is dispersed within the sample. “Super-fine” low-density bituminous organics line cavities and fill pore space, while fine clays tend to coat grains.

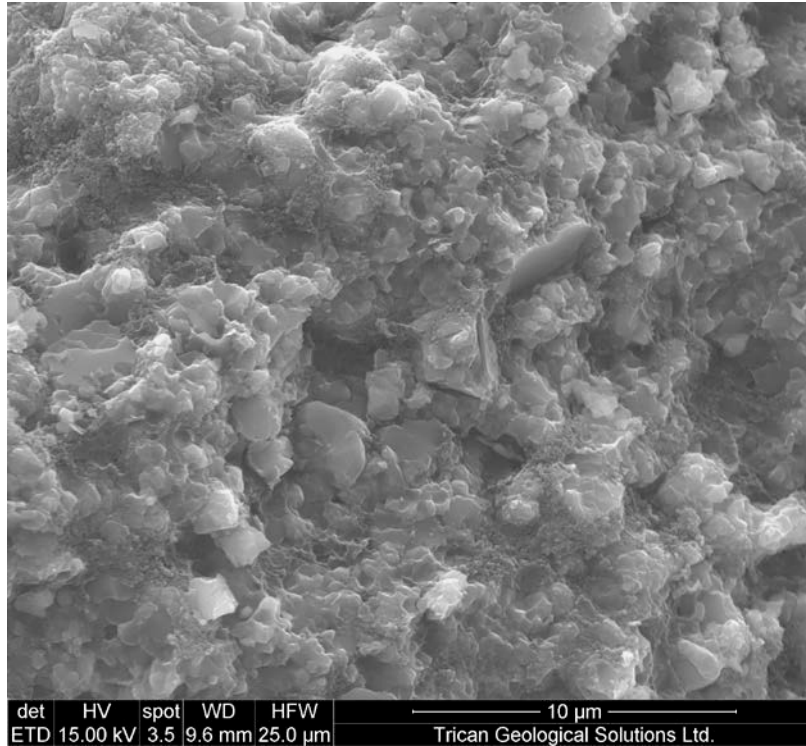


**Figure 23.** SE photomicrograph showing fine silt- to clay-size authigenic quartz grains and anhedral feldspar cements, within fine clay minerals and organic matter.

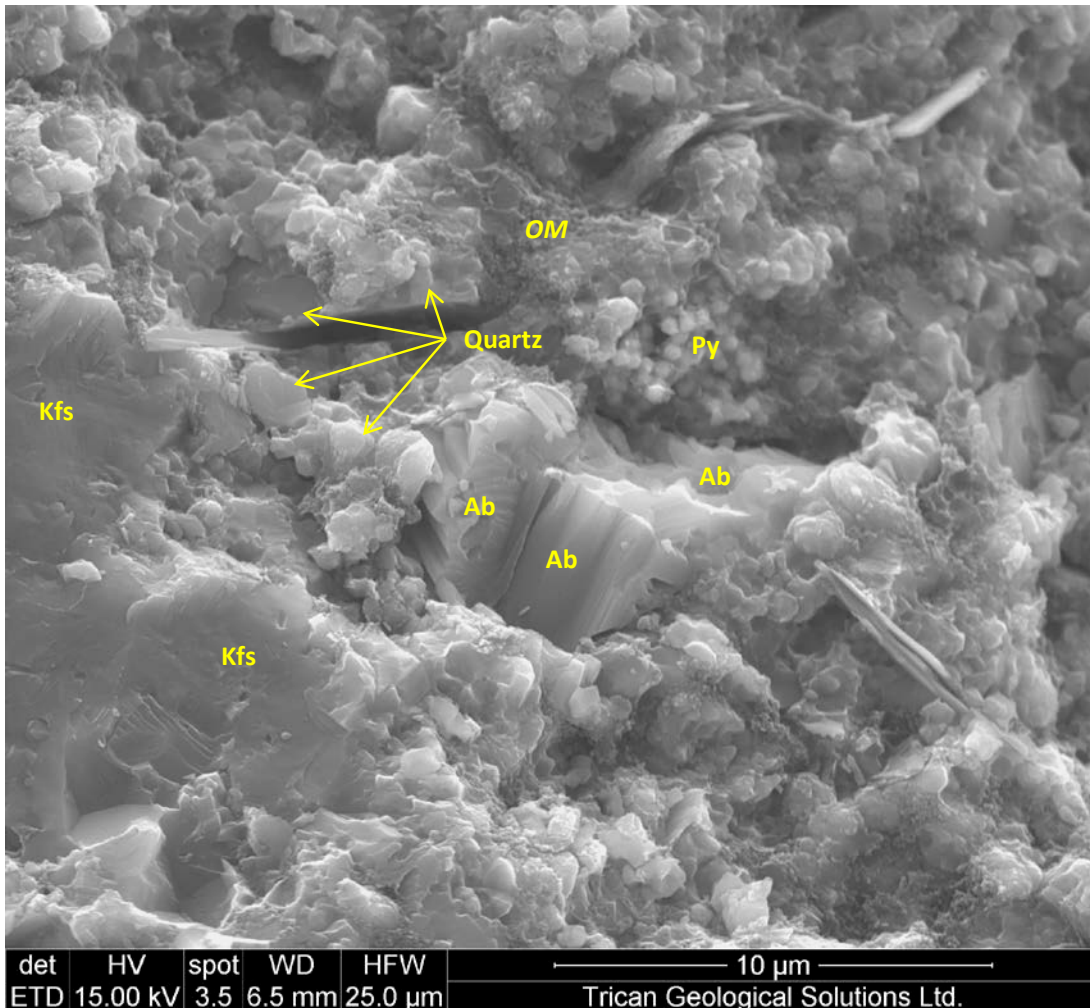
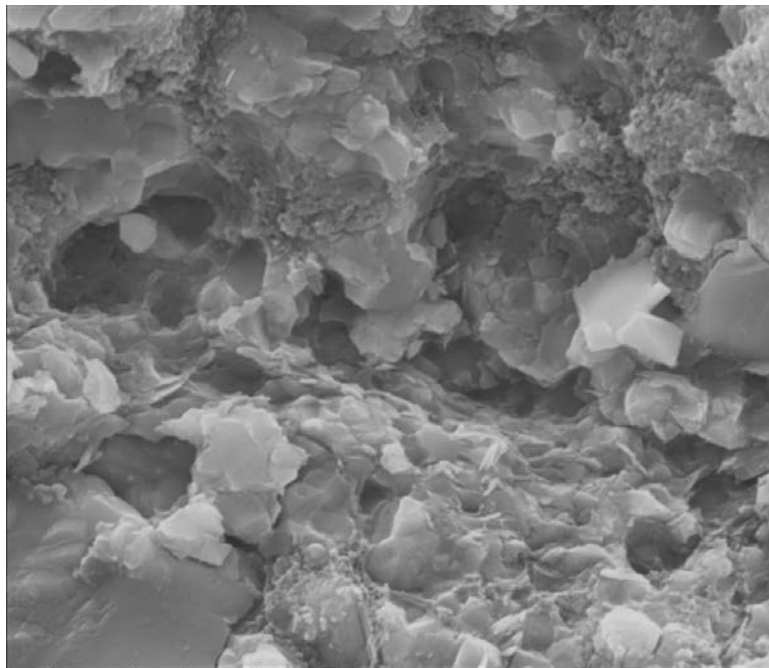
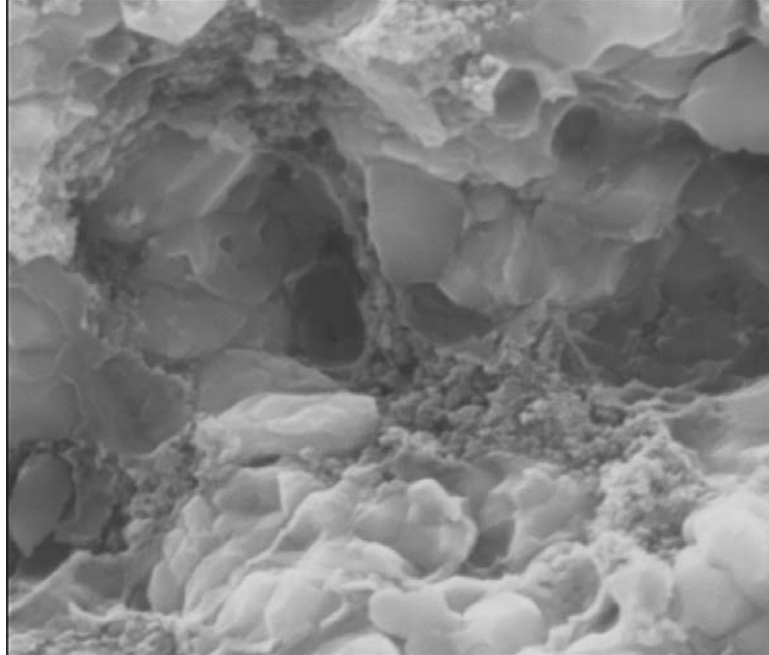


**Figure 24.** SE photomicrograph showing anhedral feldspar grains (K-feldspar bottom left and albite at center) surrounded by fine silt to clay size neoformed quartz, pyrite, organic matter and clay minerals.

**POROSITY** Pore space in sample FX67.18a is predominately intercrystalline, with the largest voids observed associated with mica sheets. Large dissolution pores and grain plucked void spaces (500nm-3 μm) reveal true intercrystalline pore space in the minerals surrounding (often less than 20-200nm). Intracrystalline pores, in the form of residual growth pores, are observed in grains <1 μm in size with pores as small as 5-50 nm. Ubiquitous low density porous organic matter both conceals and preserves additional porosity by coating and filling void space and featuring 5-50 nm pores within the organic matter network.



det	HV	spot	WD	HFV	5 $\mu$ m
ETD	10.00 kV	3.0	9.9 mm	10.0 $\mu$ m	Trican Geological Solutions Ltd.



det	HV	spot	WD	HFV	2 $\mu$ m
ETD	10.00 kV	3.0	9.9 mm	5.00 $\mu$ m	Trican Geological Solutions Ltd.

**Figure 25.** SE photomicrographs showing intercrystalline porosity in matrix composed of microcrystalline quartz, organic matter and clay minerals. Note texture of porous organic matter, likely both preserving and concealing additional porosity.

## SAMPLE FX67.18B

The mineralogical composition of **sample FX67.18b** determined by X-ray diffraction techniques is comprised of mainly quartz (56%) and apatite (25%), with lesser amounts of feldspar (6%), illite/mica (6%), and pyrite (4%). The remaining 3% is comprised of small amounts of calcite, dolomite, and natrolite (zeolite). Trace amounts of hydroxyl apatite are also detected.

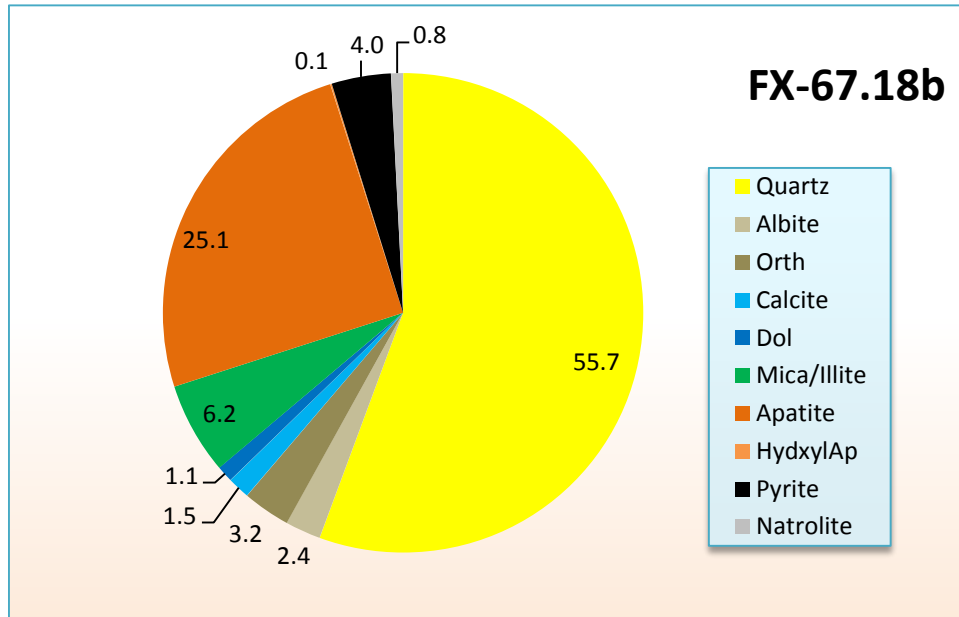


**Figure 26.** Pie-diagram of the mineralogical composition of sample FX-67.18b determined by XRD analysis. This composition is dominated by quartz and apatite, with lesser amounts of clay minerals, feldspar, pyrite, carbonates, and zeolite natrolite.

The mineralogical composition of **sample FX-37.18b** determined by visual analysis under SEM is comprised of mainly quartz (~50-60%), with lesser amounts of carbonates (10-15%), feldspar (10-15%), and illite/mica (5-10%). The remainder of the sample is comprised of pyrite, fine grained clay minerals, and organic matter.

The mineral composition determined by visual analysis under SEM does not correspond to the mineralogical composition represented in Figure 26 above, determined by X-ray diffraction techniques. While both contain comparable quartz content, the SEM sample does not contain any apatite as identified in the XRD trace pattern (~25 wt-%).

---

## SEM ANALYSIS

---

An overview image below (*Figure 27*) shows a photograph of the hand sample in order to show the texture of the sample visible to naked eye. The surface of **sample FX-67.18b** features medium grey shale with dark silt-sized “specks” that appear to be grains. The habit of the hand sample disc separated along plane of weakness created by horizon containing silt-sized particles of organic matter.



**Figure 27.** Photograph of hand sample (8x magnifications) showing medium grey shale with dark silt-sized particle and white speckles.

SEM analysis of the surface of **sample FX-67.18b** revealed 5-60  $\mu\text{m}$  particles composed of low-density carbon material.

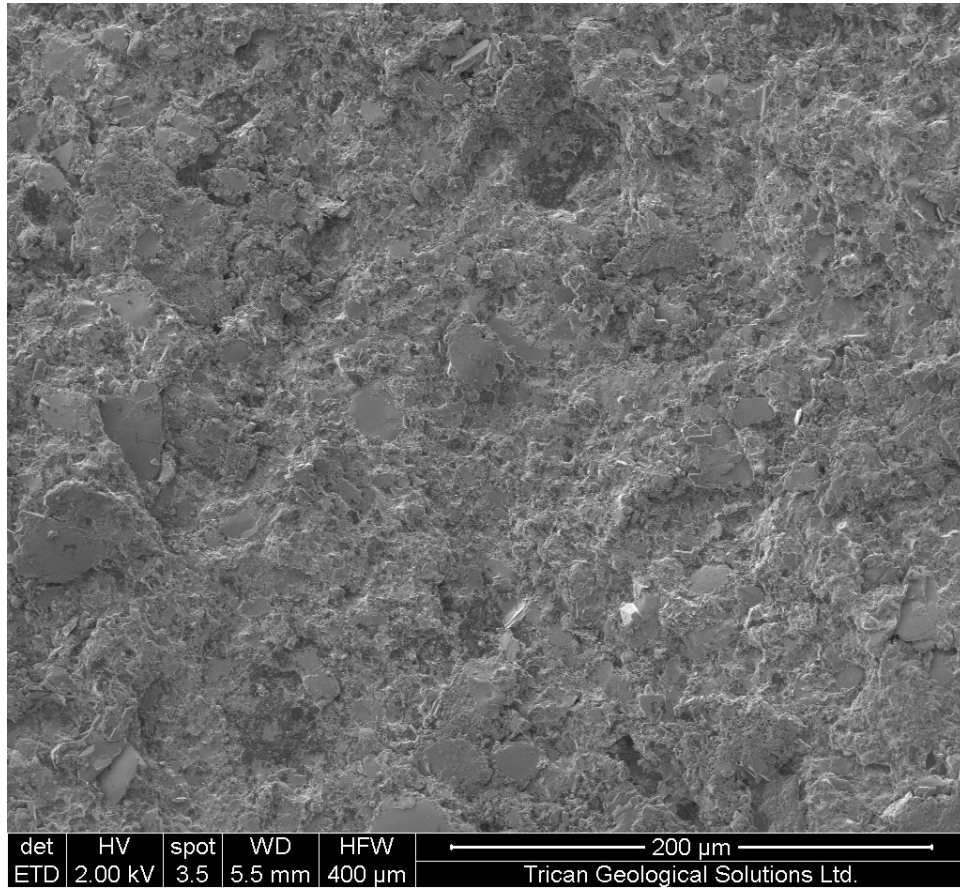


**Figure 28.** SE photomicrograph revealing surface texture of sample FX67.18b leading to broad classification as a siltstone, and further SEM investigation. Overall, the surface of the sample is covered in material with high O-contents (EDS analysis) and dark low-density carbon material. The low density spot at top of image is carbon and may represent a planktonic microfossil.

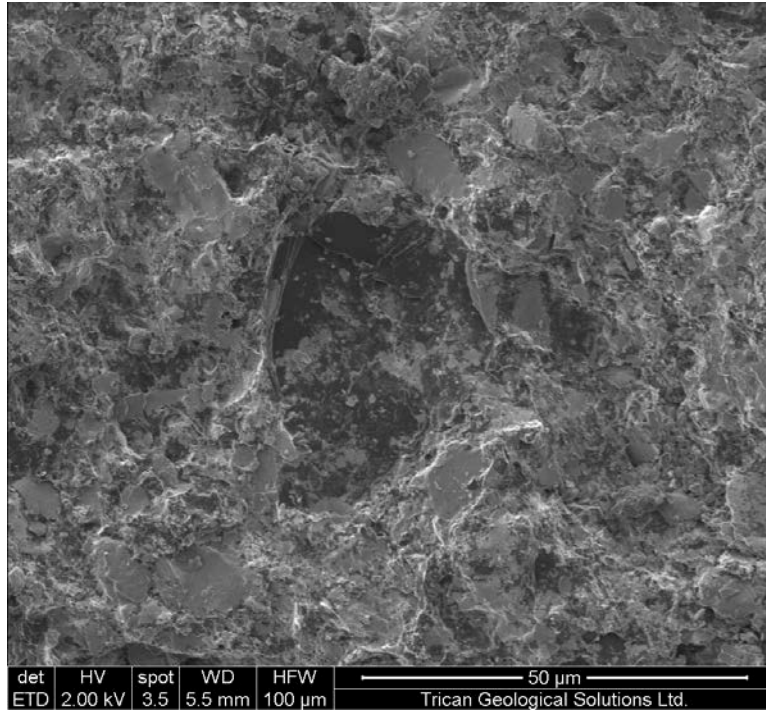


**Figure 29.** SE photomicrograph showing C-coated angular depression. This may represent a mould or cast of a microfossil.

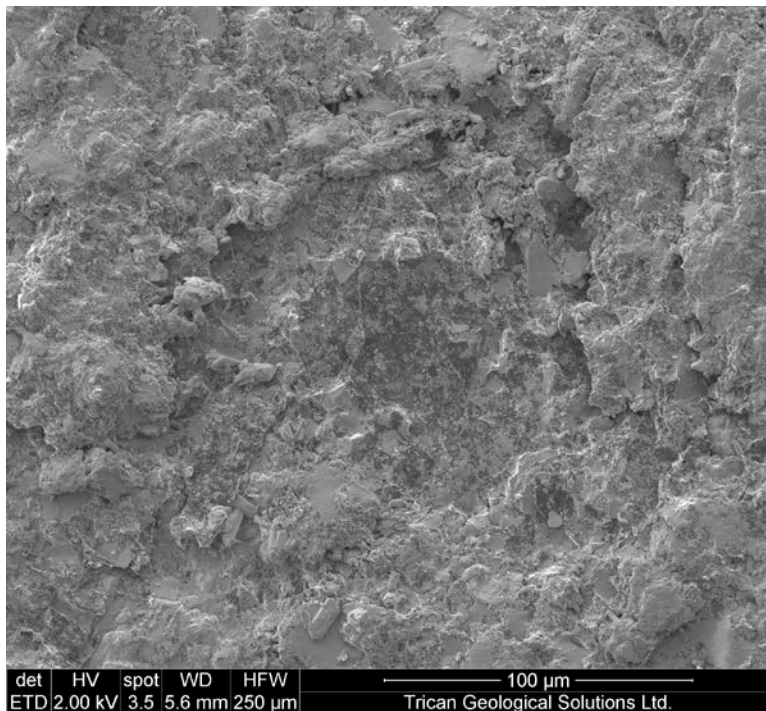


**Figure 30.** SE photomicrograph showing C-coated imprint of spiral microfossil.

**OVERVIEW** SEM analysis of the fresh chip samples reveals some fine to coarse silt-sized (10-40  $\mu\text{m}$ ) feldspar, mica (up to 60  $\mu\text{m}$ ), and carbonate particles embedded within a very fine silt to clay size matrix. Most silt-size grains have smooth surfaces which imply a late diagenetic growth (i.e. secondary origin). Few recrystallized bioclasts are recognized between the fine grains and show replacement (infill) cements of calcite or quartz. Few detrital feldspars with clay and organic coatings are observed.

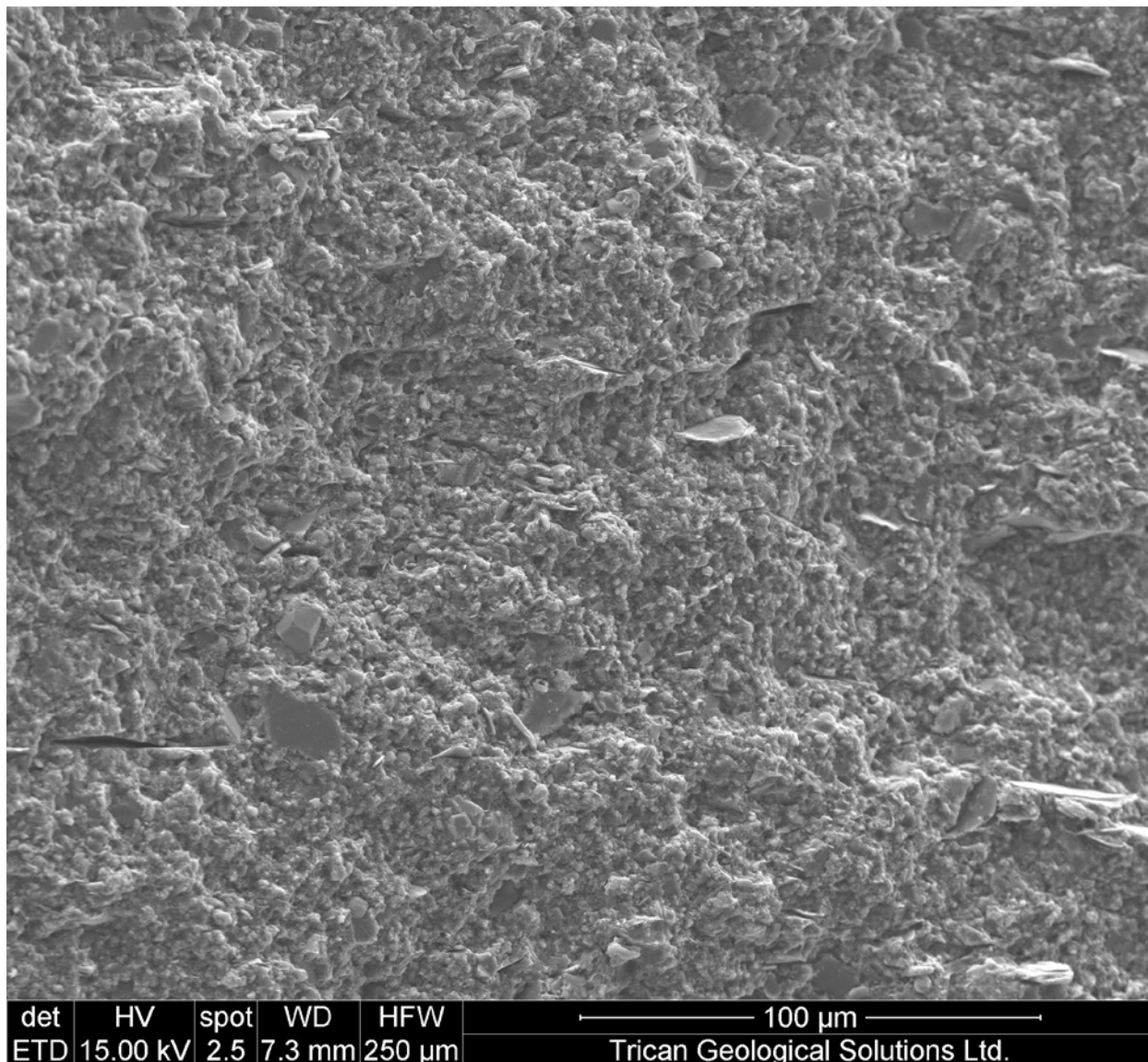


**Figure 31.** SE photomicrograph showing overview of texture and lamination within sample FX67.18b. The sample features silt-sized particles of mica, feldspar, quartz, and carbonates within a fine matrix of neoformed quartz, clay minerals, and organic matter.

**FRAMEWORK** The primary constituent of **sample FX67.18b** is quartz, comprising more than 50% of the sample volume. The silt-size “larger” quartz is observed as idiomorphic grains up to 20 µm, with abundant microcrystalline grains forming a “mass”. The most abundant grain size of quartz is less than 5 µm, with grains larger than 5-10 µm less frequently observed. Occasionally large patches of late diagenetic quartz cements are observed.

The silt-sized cement particles include quartz, dolomite, calcite, feldspar, mica, and pyrite. Quartz cements range in size from less than 2-20 µm, and feature 100-500 nm residual growth pores. Some quartz recrystallized spherical bioclasts are (radiolarians?) observed. Blocky patches of dolomite cements range in size from 5-20 µm, with 500 nm – 1 µm cubic residual growth pores. Calcite particles range in size from 5-25 µm and often feature 200-600 nm intracrystalline microporosity. Some spherical calcite recrystallized microfossils (radiolarian) are observed. Evidence of carbonate cements growth contemporaneously with quartz (usually smaller in comparison) is observed. Detrital and authigenic feldspar is present and ranges in size from 2-17 µm. The size of mica sheets vary widely, from 10-50 µm and define a clear bedding direction.

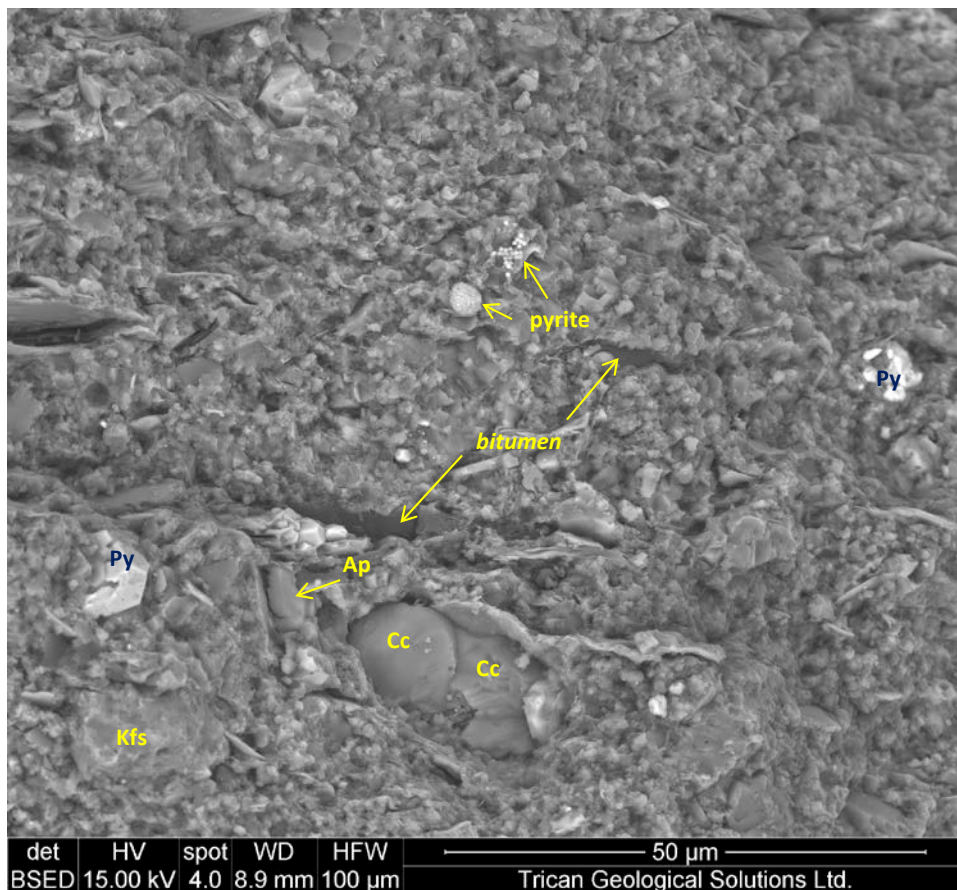


**Figure 32.** BSE photomicrograph featuring a variety of silt-sized (authigenic) particles (calcite, K-feldspar, pyrite, and quartz) and detrital mica sheets, within a fine matrix composed of neoformed microcrystalline quartz, organic matter, and fine clay minerals. Note spherical nature of calcite cement.

**GROUNDMASS** **Sample FX-67.18b** features silt-size grains embedded within a groundmass of clay to very fine silt-sized neoformed quartz, clay minerals, and bituminous organics. The

abundant clay-size quartz crystals range in size from 200 nm up to 1-2  $\mu\text{m}$  (see Figure 33 and 34). Fine-grained illite is dispersed within the sample as is “super fine” bituminous organic material.

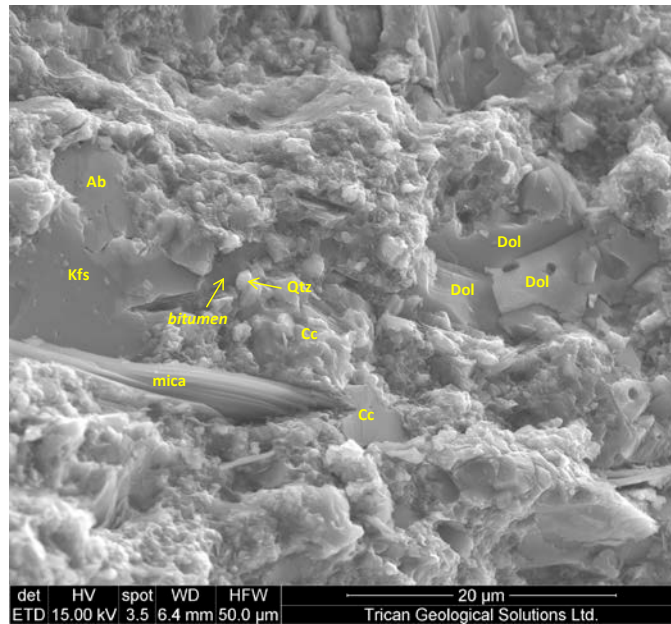


**Figure 33.** SE photomicrograph featuring feldspar and carbonate authigenic grains (angular, smooth surfaces) within a fine matrix of microcrystalline quartz, organic matter, and clay minerals.

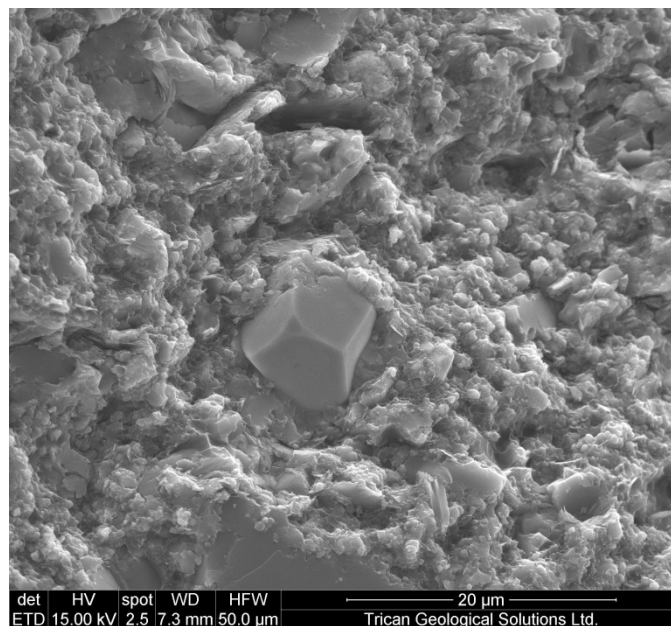


**Figure 34.** SE photomicrograph showing an octahedral pyrite crystal observed in sample FX-67.18B, contributing to framework grains composed of late diagenetic cements.

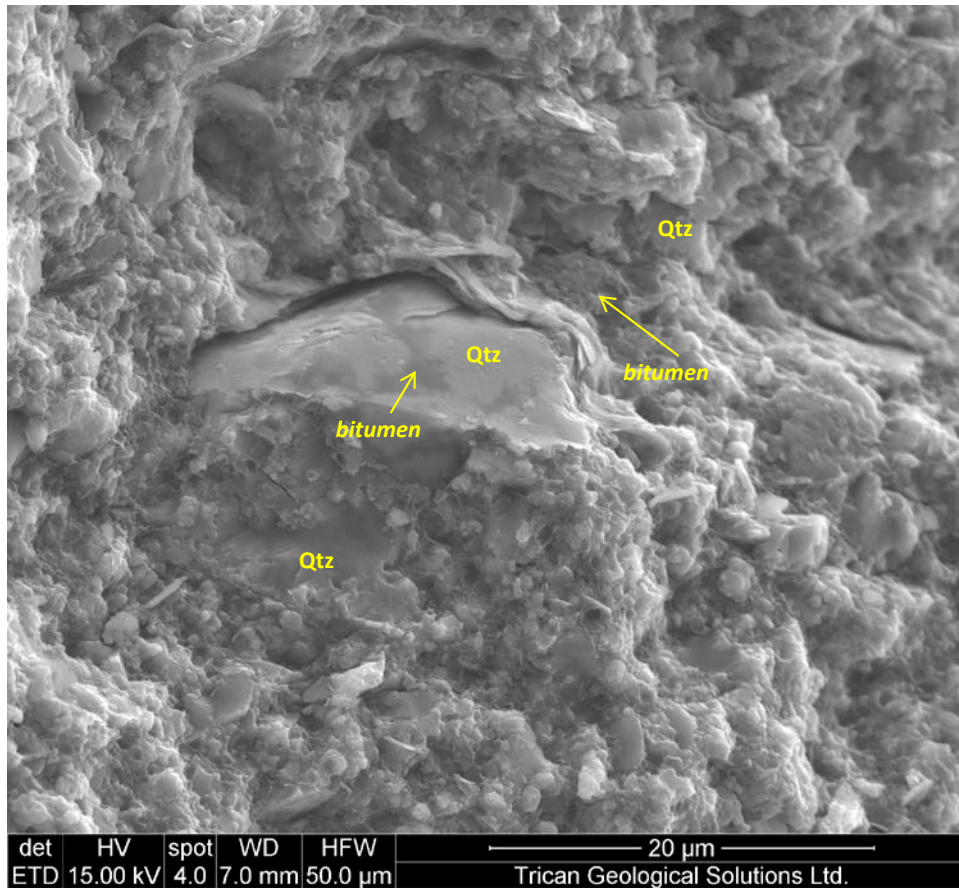


**Figure 35.** SE photomicrograph revealing bitumen and quartz “sheets” filling a void space bounded by a flat mica sheet that has been removed leaving a planar cavity above remaining clay sheets. Note quartz cement below, as well as clay-size microcrystalline quartz crystals within matrix.

**POROSITY** Pore space in this sample is predominately associated with intercrystalline space surrounding grain boundaries. Intercrystalline pore space ranges from 100-200 nm up to 600-1000 nm surrounding mica sheets. Intercrystalline pore space is often observed surrounding cement crystals that have been “dislodged” from original cavity due to sample prep and unloading. Open dissolution voids are observed throughout the sample, revealing intercrystalline space exposed by grain plucking during sample preparation. These cavities reveal lining of fine clay minerals and organics, and range in size from 700nm - 1.5  $\mu\text{m}$ . A single fracture was observed, featuring porosity ranging from 100-400 nm between cement filling fracture and surrounding matrix. (Figure 36)

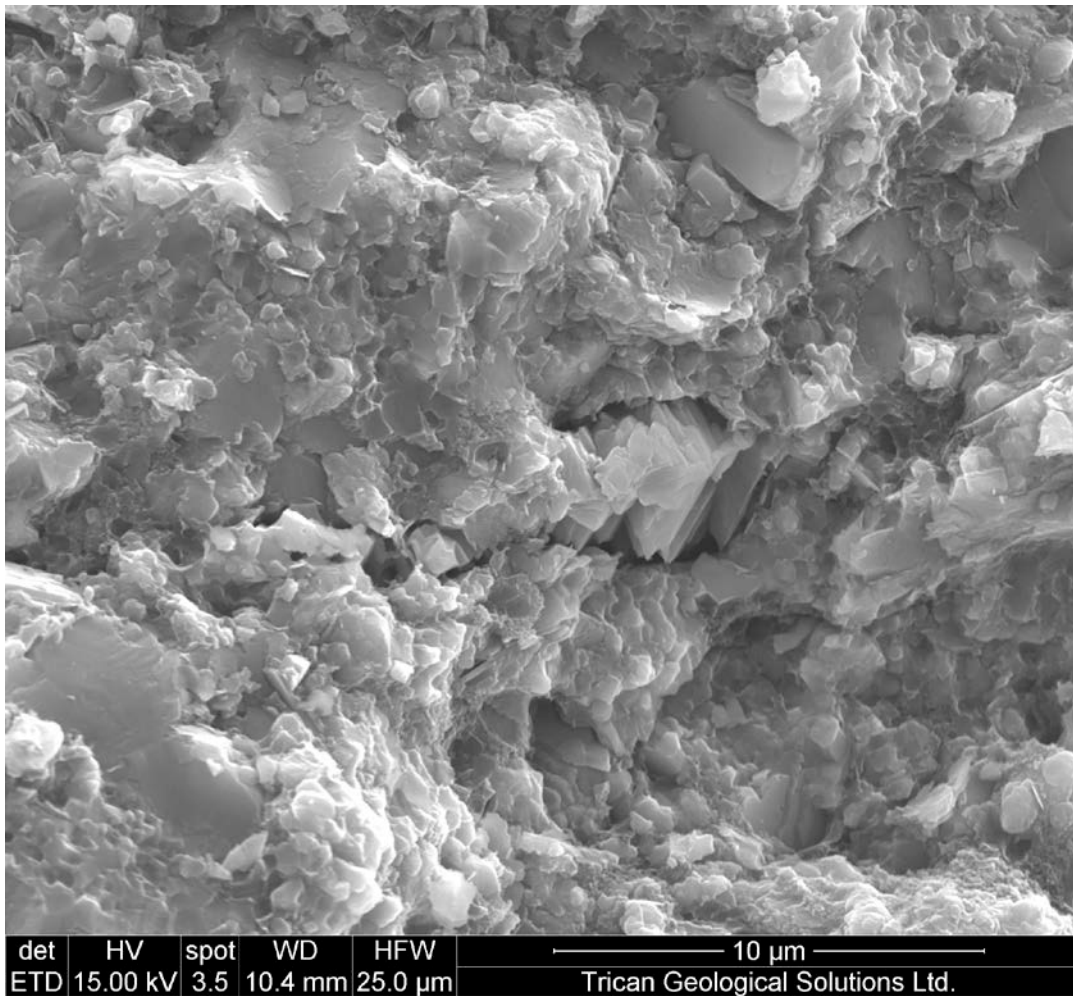


**Figure 36.** SE photomicrograph showing porosity surrounding albite cement within a fracture. Note microcrystalline quartz crystals <1  $\mu\text{m}$  with thin sheets of clay minerals and organic matter at bottom center in contrast with massive quartz grains and clay sheets in upper left. Note very fine organic matter at bottom right.

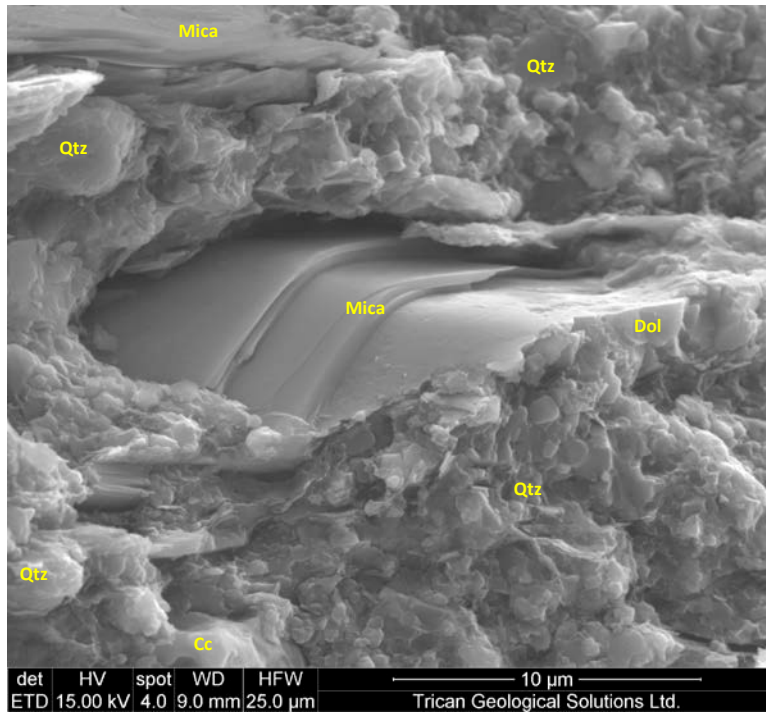


**Figure 37.** SE photomicrograph showing mica sheets embedded between quartz and carbonate microcrystals.

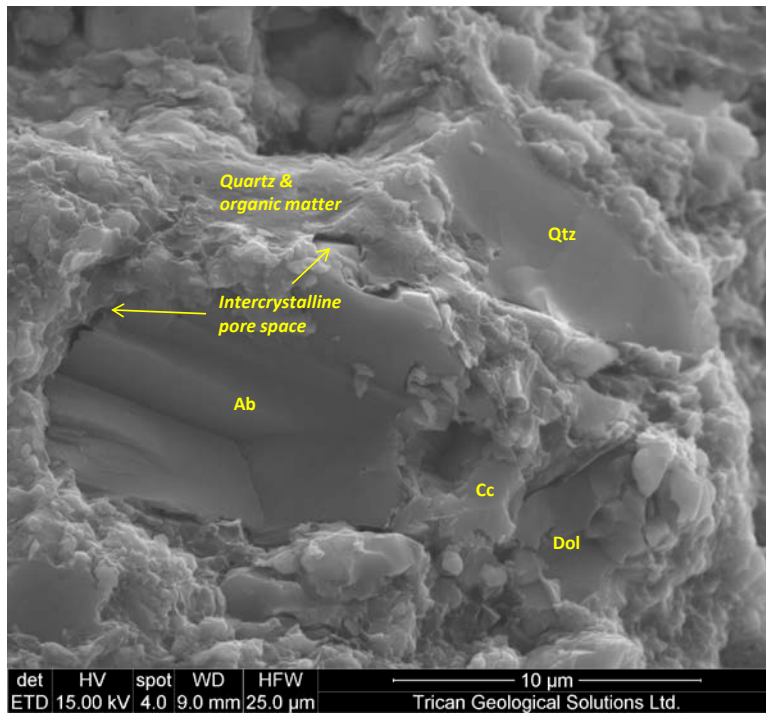


**Figure 38.** SE photomicrograph revealing an authigenic albite surrounding a former euhedral crystal and massive authigenic quartz, calcite, and dolomite grains.

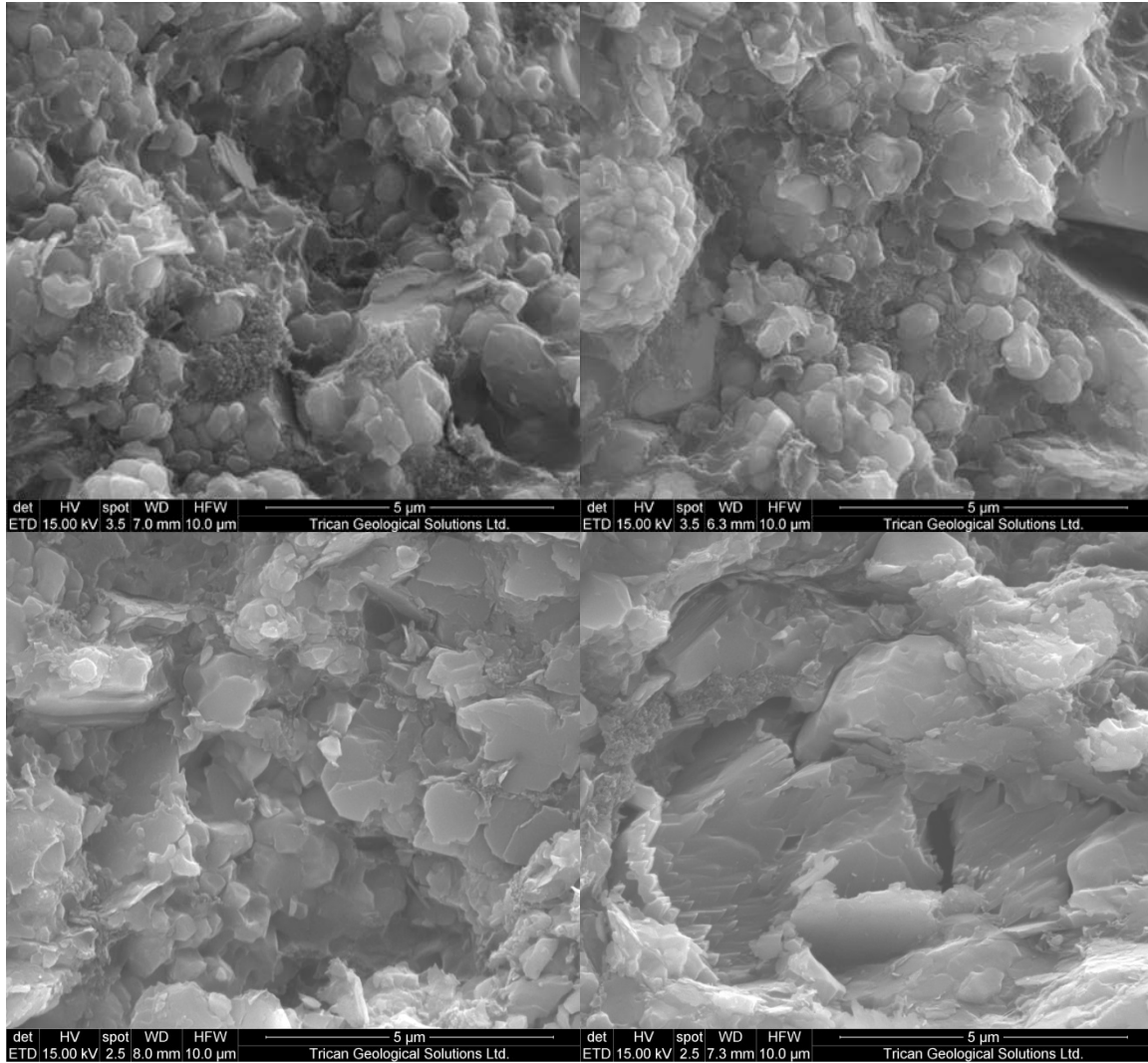


**Figure 39.** Collection of SE photomicrographs revealing fine grained organic matter (top left), clay-size neofomed quartz (top right), clay minerals (bottom left), and carbonate cements (bottom right).

## SAMPLE FX-67.18C

---

### THIN SECTION ANALYSIS

---

The photo below shows scans of the thin section under standard (left) and overexposed light (right) to provide information about the natural texture of the rock. The thin sections reveal a contact between an organic-rich black mudstone/shale and an overlying “sandy siltstone”.

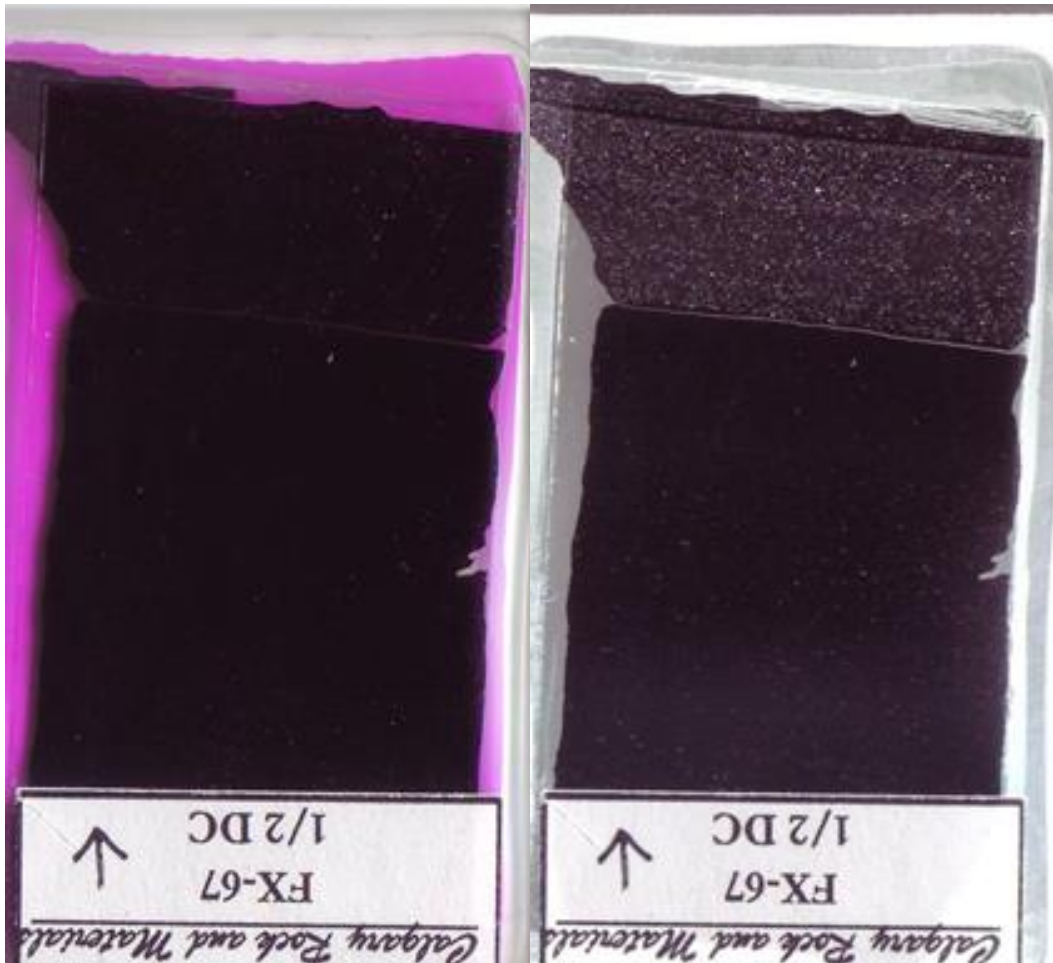


**Figure 40.** Thin sections scans of sample FX-67.18c under standard (left) and overexposed (right) light revealing a finely laminated organic-rich mudstone/shale underlying a “sandy siltstone”.

The mineral composition of **sample FX-67.18c** determined by XRD refinement is dominated by quartz (66%), with lesser amounts of feldspar (16%), mica/illite (12%), pyrite (4%), and dolomite (3%). The total organic carbon content of the sample is very high and is estimated to be between 7-10 wt-%.

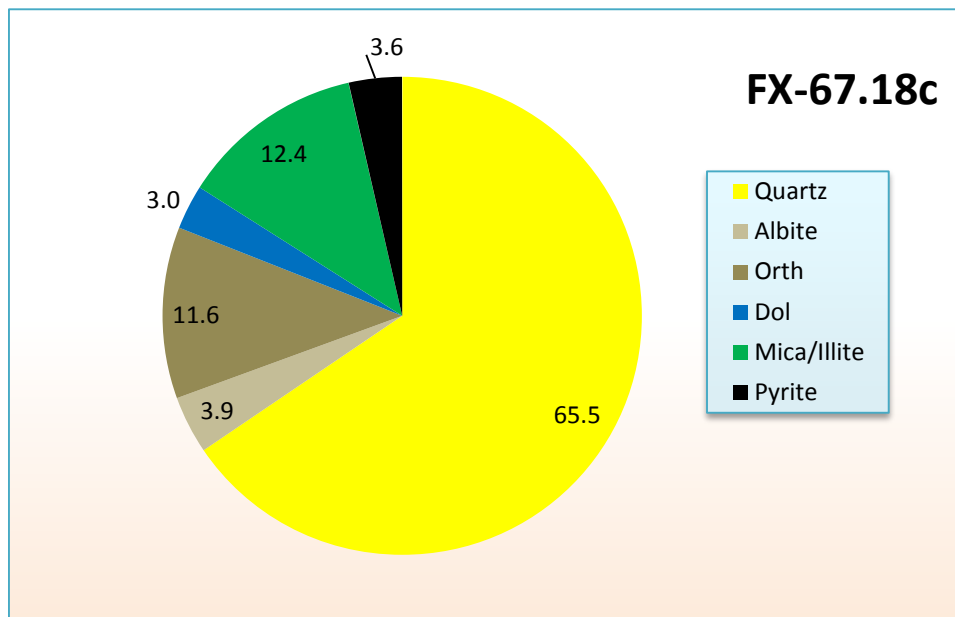


**Figure 41.** Pie-diagram of the mineralogical composition of sample FX-67.18c showing the dominance of quartz (~66 wt-%), with lesser amounts of feldspar and clay minerals in this sample.

Analysis of fresh chip samples using SEM reveals minor amounts of calcite cements not quantified by XRD refinement, as well as silt-sand size algal cysts composed of sphalerite (ZnS) within upper siltstone/sandstone. No dolomite was observed in either composition.

**OVERVIEW** **Sample FX-67.18c** features a contact between two compositions: a lower black organic-rich mudstone/shale and an upper organic-rich siltstone/sandstone. The lower unit features silicified lenticular algal remains, recrystallized bioclasts, and authigenic quartz grains that impart a subtle lamination to the sample with bedding parallel orientation. The silt-sand sized particles of the upper unit are quartz and sphalerite replaced algal cysts. Subtle lamination is defined by bedding parallel orientation of abundant algal cysts and minor lenticular algal remains. Much of the framework and matrix is obscured by abundant opaque organic matter.

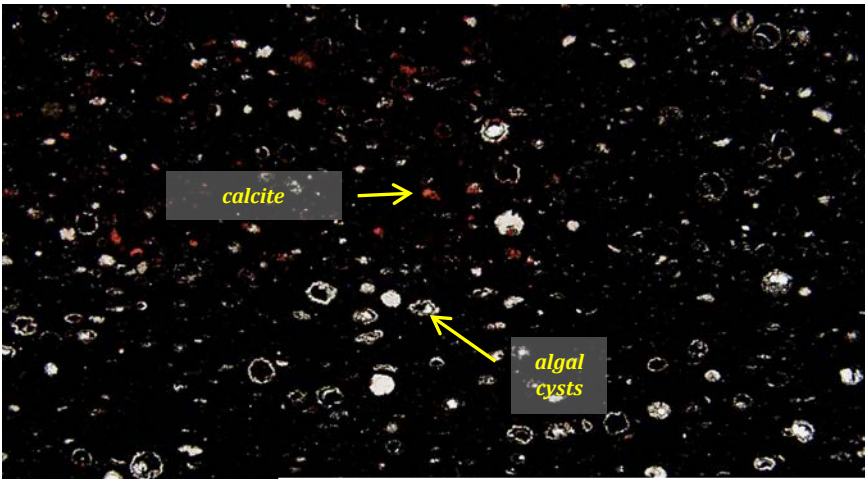


**Figure 42.** Photomicrographs in PPL. Left: showing ubiquitous algal cysts with organic and/or quartz cement filled cores, within an organic-rich matrix. Below: showing contact between an organic-rich algal cyst mudstone/shale and an organic-rich mudstone/shale. Bright white grains in mudstone/ shale are quartz replaced microfossils (authigenic quartz cements).

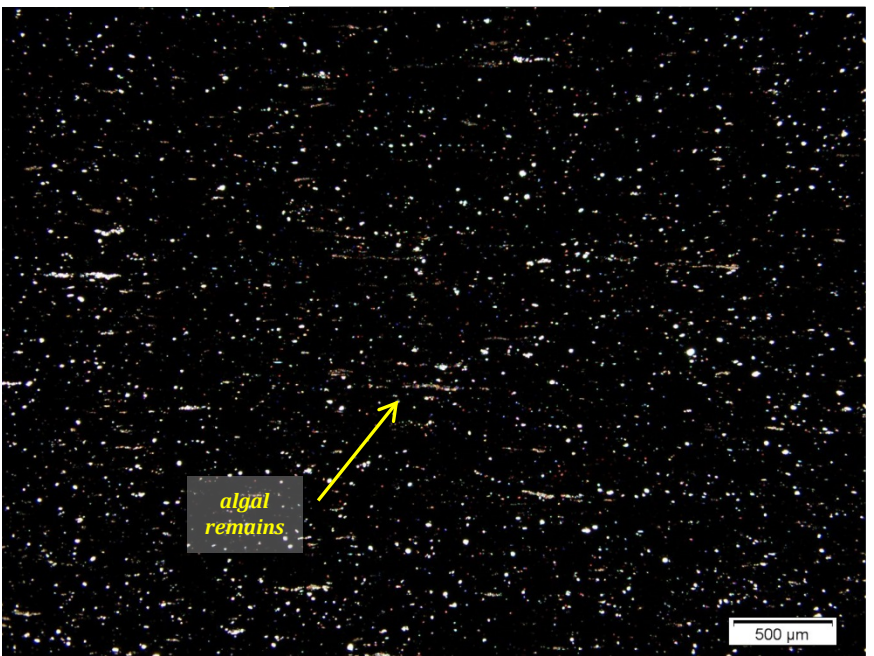
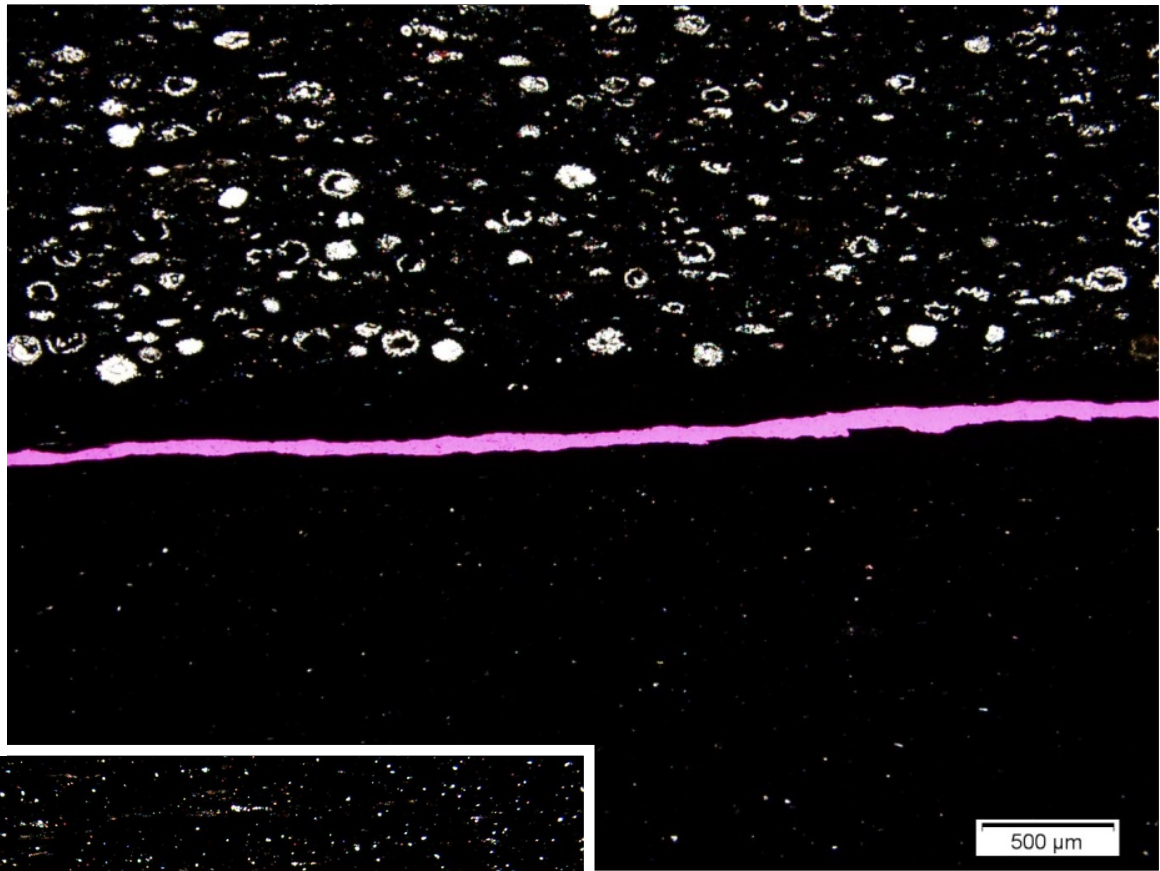


**Figure 43.** Left: Photomicrograph under overexposed PPL showing lenticular algal remains oriented parallel to bedding, within an organic rich matrix of microcrystalline quartz grains (secondary cement).



**FRAMEWORK** The primary framework constituent of **sample FX-67.18c** is quartz, observed as abundant recrystallized algal cysts (possible tasmanites, dasyclads, and radiolarians), lenticular algal remains, recrystallized microfossils, and authigenic cements.

The ubiquitous algal cysts in the **upper unit** range in size from 30-170  $\mu\text{m}$ . Algal cyst cell walls are replaced by mostly polycrystalline quartz and occasional by calcite and dolomite (cements) where pore space was left open after the quartz cementation. Cysts are often deformed or partially crushed with irregular amoeboid shapes. Algal cysts feature cementation by solid cements, polycrystalline and/or microcrystalline quartz, and/or solid bituminous organics. Variations in between include geopetal structures (center of Figure 44), sub-rounded to sub-angular "nucleus" at center surrounded by bituminous organics, and blocky quartz cements. Often quartz crystals exhibit undulose extinction indicating stress deformation. Carbonates (mostly calcite) fill in jagged outer edges of blocky crystalline algal cysts as well as fully recrystallizing other bioclasts and particles. The red stained grains in Figure 44 is calcite material. In addition to algal cysts, the sample also contains many other quartz recrystallized microfossils ranging in size from 5-15  $\mu\text{m}$ .

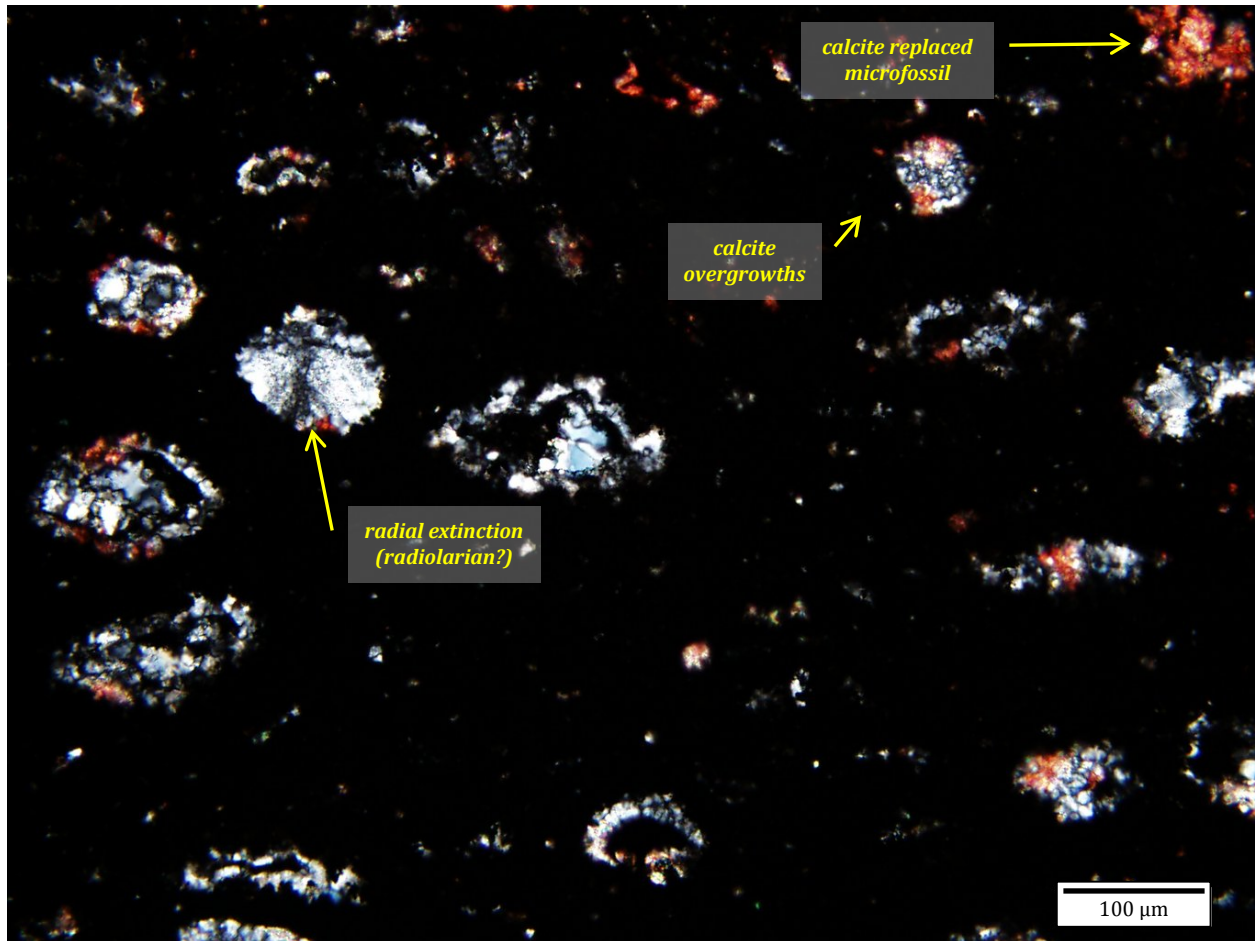


**Figure 44.** XPL photomicrograph showing abundant algal cysts (tasmanites, dasyclads?) featuring predominately quartz cements, with some calcite overgrowths. Note variable structure of microfossils, including possible radiolarian exhibiting radial extinction as well as geopetal features (center). Cysts cavities contain combinations of quartz cement and/or opaque bituminous inclusions.

The primary framework component of the **lower unit** is also quartz. Quartz grains are observed as silicified algal remains, recrystallized microfossils, and angular cements. Silicified algal laminae present range in size from 50-500  $\mu\text{m}$  long and <10- 50  $\mu\text{m}$  thick. The silicified algal remains contain quartz grains and mica sheets that are bound together by microcrystalline quartz, clay minerals, and organic matter.

The sample also contains rounded to sub-rounded quartz recrystallized microfossils, ranging in size from 15-70  $\mu\text{m}$ . frequently these quartz recrystallized microfossils form clusters or are included in algal mats (50-200  $\mu\text{m}$ ) that are connected with microcrystalline quartz overgrowth cements. Some quartz pseudomorphs after dolomite are observed, ranging in size from 10-15  $\mu\text{m}$ , and feature partial dissolution with quartz overgrowths. Finally, the framework contains abundant mica sheets, ranging in size from 3-30  $\mu\text{m}$ .

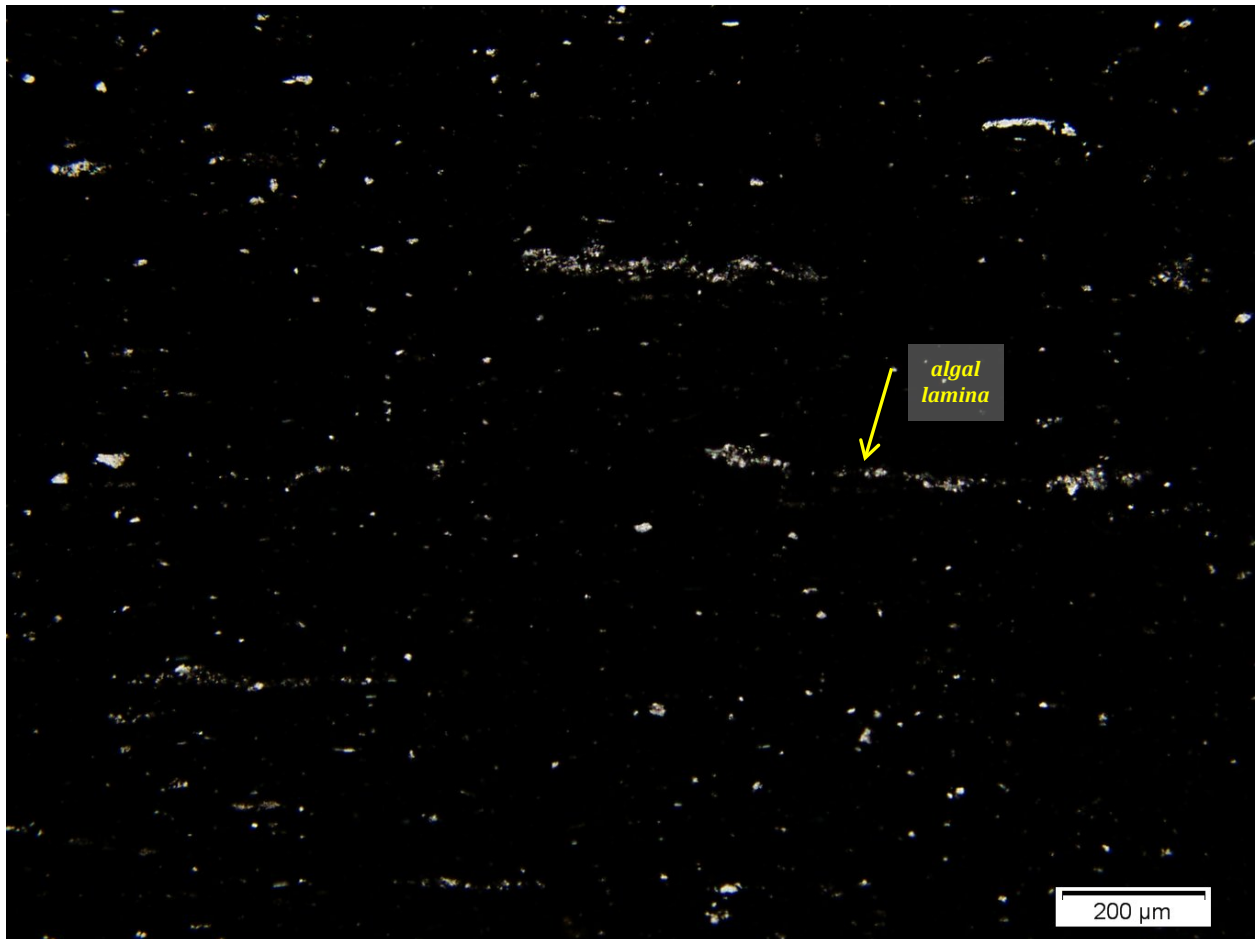


**Figure 45.** Photomicrograph in PPL showing silicified algal remains, recrystallized microfossils, and angular quartz cements (pseudomorph after dolomite) within an organic-rich matrix.

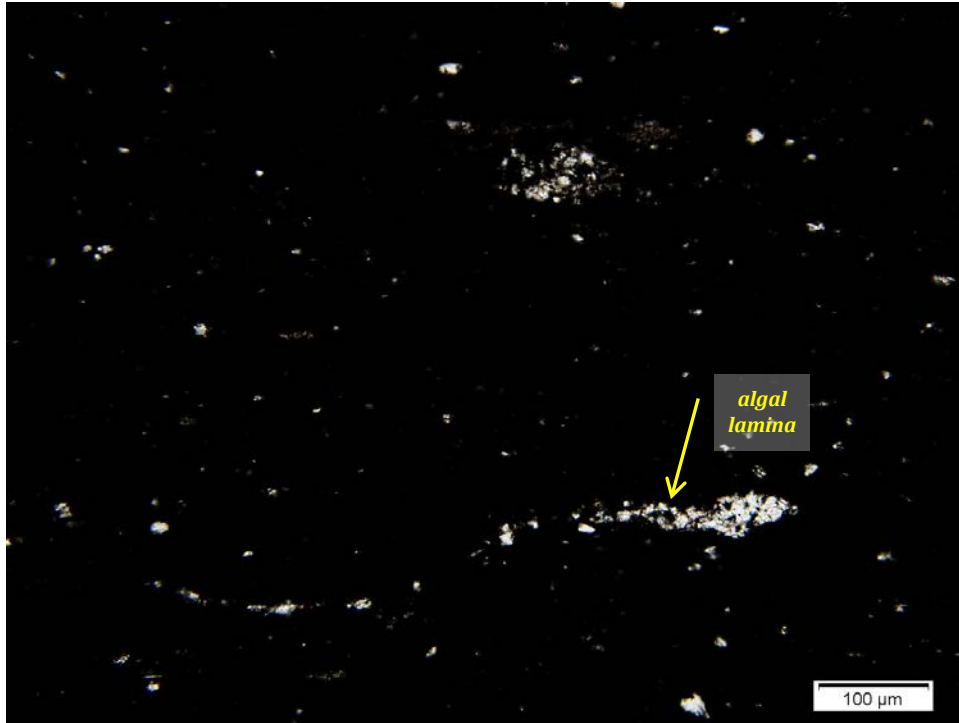


**Figure 46.** Photomicrograph in PPL showing silicified algal remains. Note variable length and thickness of remains,

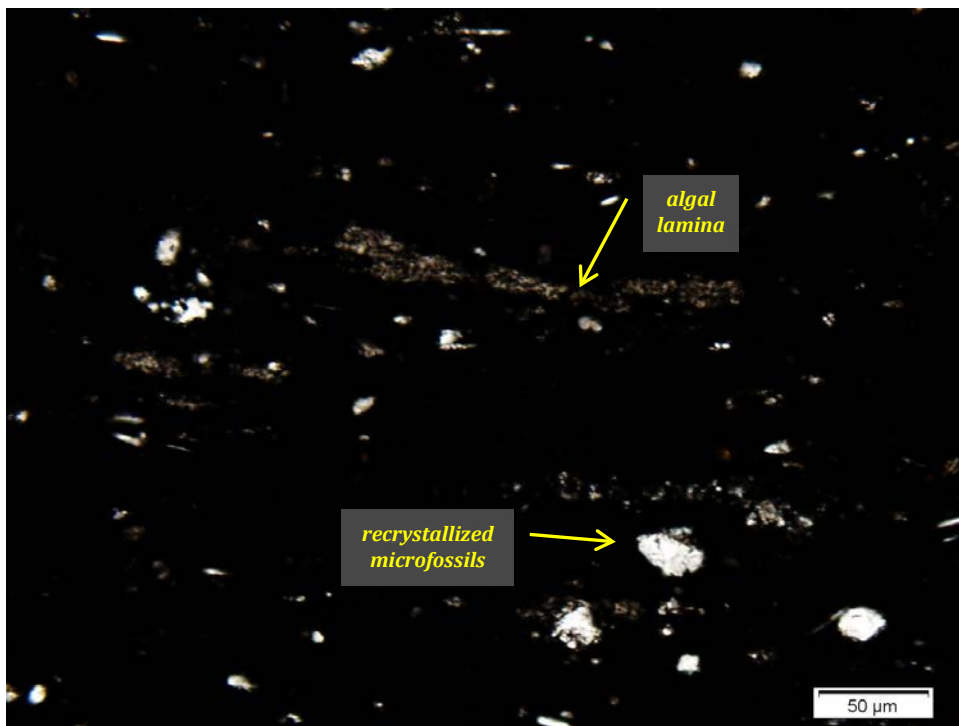


**Figure 47.** Photomicrograph in PPL showing clay-rich and/or organic stained algal remains, with quartz recrystallized microfossils and mica sheets in black organic-rich matrix.

**GROUNDMASS** The fine grained nature and the high finely dispersed organic matter of this sample make interpretations and identifications of minerals phases and cements within the groundmass difficult. Using overexposed light techniques, the matrix contains clusters of microcrystalline authigenic quartz and abundant organic material with possibly some clay minerals (mica sheets are apparent in thin section). Few feldspar grains are detected within the matrix.

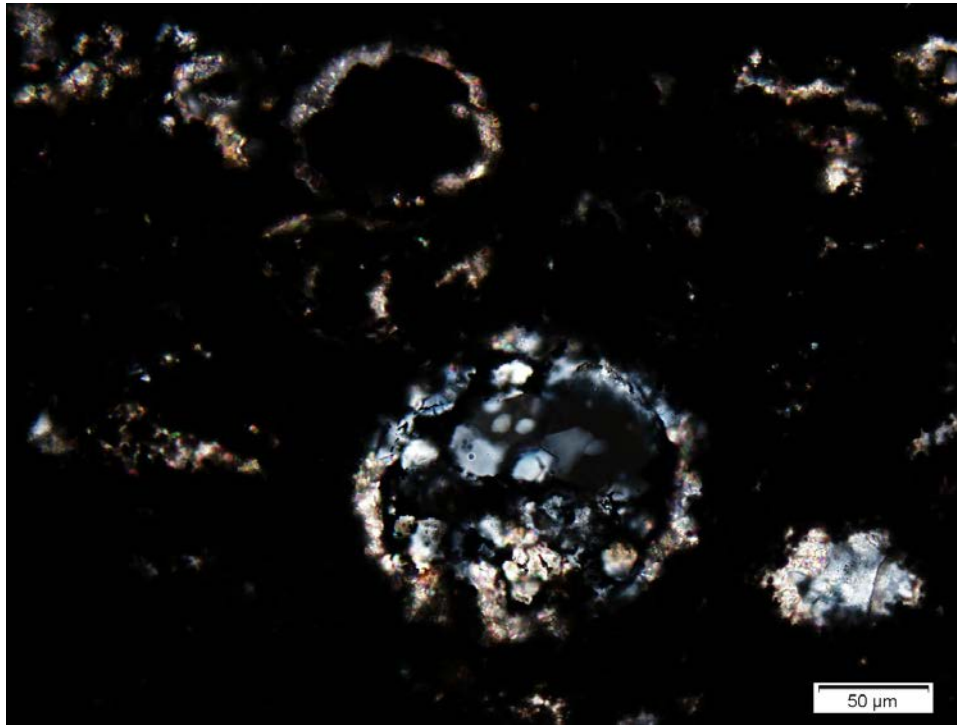


**Figure 48.** XPL photomicrograph showing an algal cyst (tasmanite, dasyclad?) featuring both quartz and carbonate cements. At bottom right a recrystallized microfossil with both quartz cements and carbonate cements (possibly an overgrowth).

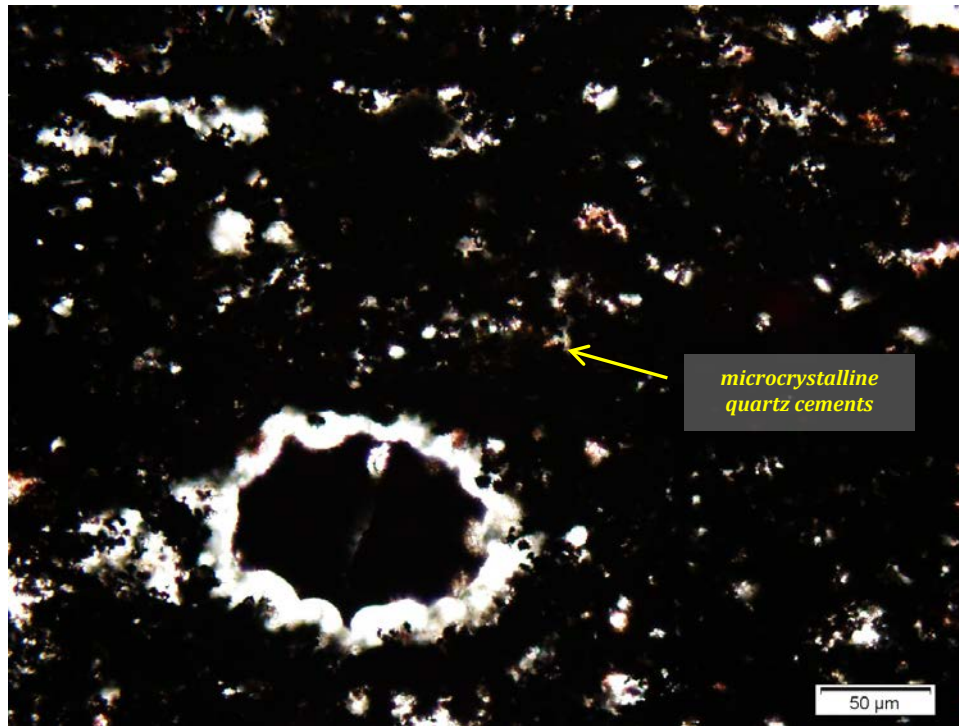


**Figure 49.** Overexposed photomicrograph showing microcrystalline quartz cements within matrix. Note groundmass still predominately concealed by ubiquitous opaque organics.

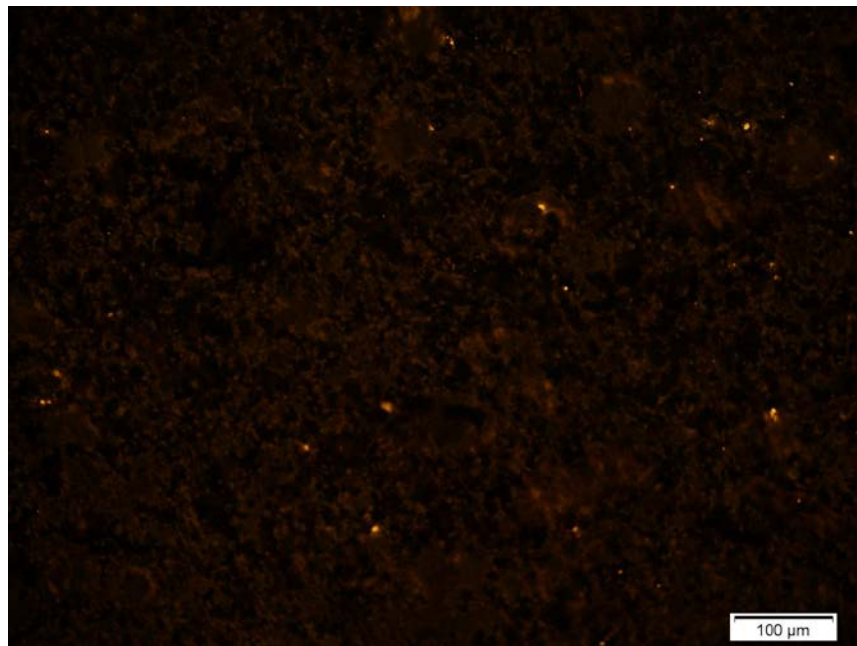


**Figure 50.** Photomicrograph under UV light showing minimal porosity (yellow bright spots). Bright spots are not 100% epoxy indicating that they only represent partial porosity (of the 30μm thick slide).

**POROSITY** Little pore space was observed in this thin section which may be due to the opaque nature of the abundant organic material. Overall, porosity may be very small and possible <2%. It is possible that abundant bituminous organics are both preserving and concealing additional pore space.

**PARAGENESIS** Deposition of organic-rich biogenic material composed of abundant algal material and algal debris. Compaction and diagenesis including neof ormation of quartz grains and cementation of bioclasts. Fluid migration and further cementation with mostly quartz grains and reducing porosity. Overprint with calcite cementation. Organic matter maturation. Uplift and exposure results in corrosion.

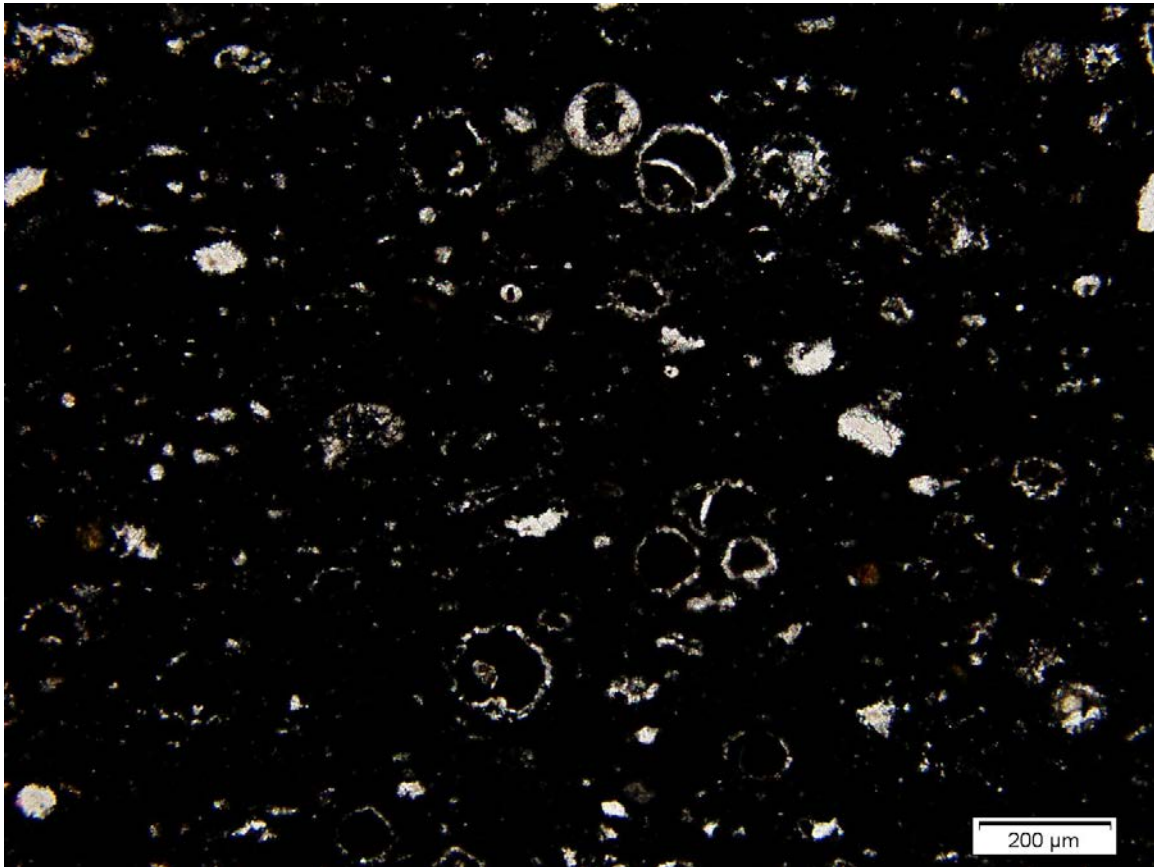


**Figure 51.** Photomicrograph in PPL showing abundant algal cysts, recrystallized microfossils, and quartz cements, within an opaque organic-rich matrix.

---

## SEM ANALYSIS

---

### UPPER UNIT: SILT/SANDSTONE

---

**OVERVIEW** SEM analysis of the fresh chip sample reveals very fine to medium silt-sized quartz grains (5-25  $\mu\text{m}$ ) and mica sheets (5-30  $\mu\text{m}$ ) embedded within a fine matrix of permeating quartz cement, neoformed microcrystalline quartz grains, feldspar, fine clay minerals, and pyrite. Most silt-size grains have smooth surfaces which imply a late diagenetic growth (i.e. secondary origin).

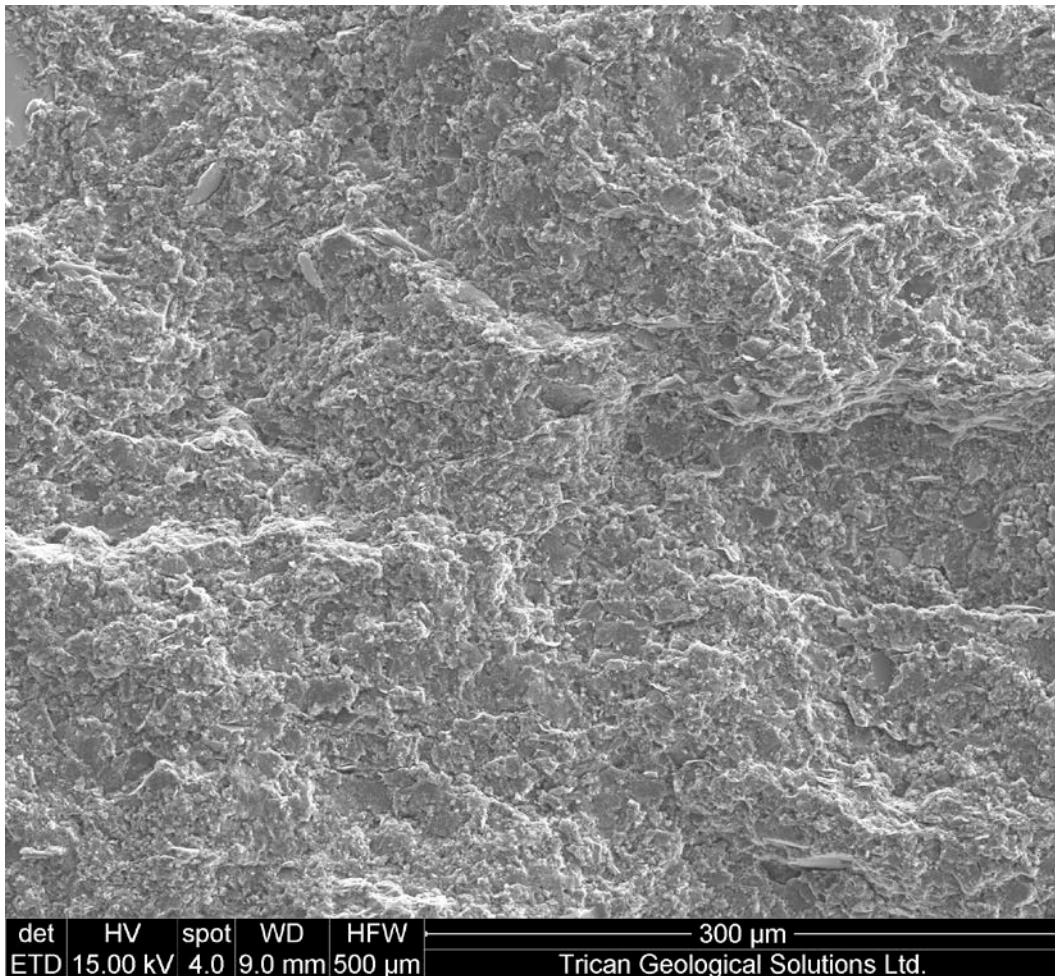


**Figure 52.** SE photomicrograph showing overview of texture and lamination within sample FX-67.18c. Sample features silt-sized quartz cements and mica sheets, embedded within a granular organic- and quartz- rich micrometer-scale grain matrix.

**FRAMEWORK** The primary framework component of **sample FX-67.18c** is quartz, comprising of approximately 60-70% of the sample volume. Inspection under back scatter detector reveals abundant algal cysts composed of high-density sphalerite (ZnS), ranging in size from 50-150  $\mu\text{m}$  (Figure 53). In contrast, siliceous algal cysts blend in with quartz-rich matrix and are more difficult to recognize (Figure 55). Both types of cysts are filled with porous quartz and/or sphalerite cement or only low-density bituminous organics. Few instances of solid bitumen particles at 3-35  $\mu\text{m}$  are observed, most commonly occur filling intercrystalline space. The framework also contains spherical quartz recrystallized bioclasts of 15-20  $\mu\text{m}$  in size. The remainder of quartz framework grains are observed as silt-size grains with smooth surfaces (cements) ranging in size from 5-35  $\mu\text{m}$ , as well as abundant neofomed microcrystalline quartz grains which form the “matrix”.

The second most abundant framework component next to quartz is mica, with sheets ranging in size form 3-30  $\mu\text{m}$  average, but can be up to 50  $\mu\text{m}$  with a maximum thickness of 2  $\mu\text{m}$ . Mica sheets impart a subtle lamination on the sample and are orientated sub parallel relative to bedding. Few K-feldspar grains are observed, exhibiting a blocky irregular habit, in comparison to quartz grains within the sample.

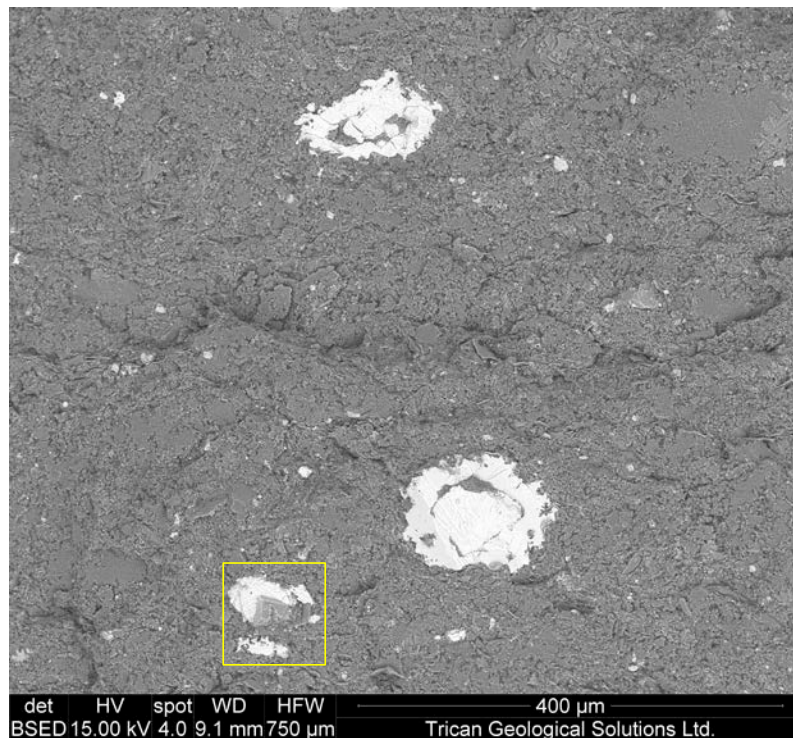


**Figure 53.** BSE photomicrograph showing two algal cysts composed of sphalerite (ZnS) embedded within a silica rich matrix. Note left wall (slightly darker) of bottom cyst features twin indicating different orientation of crystal growth.

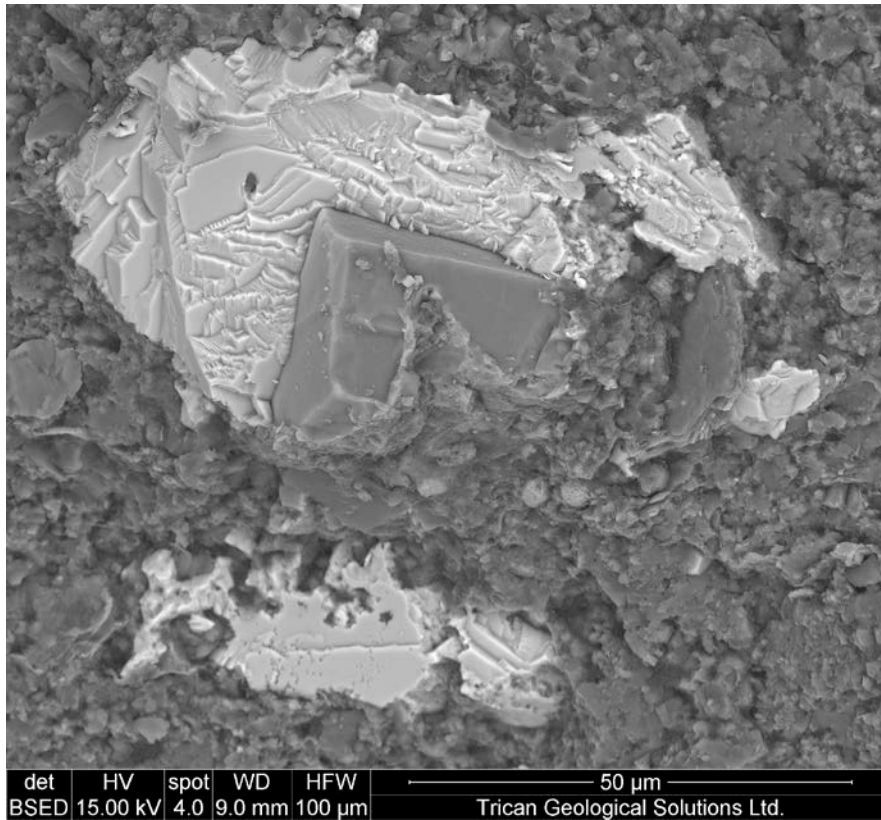


**Figure 54.** BSE photomicrograph showing an authigenic K-feldspar grain embedded within a sphalerite recrystallized microfossil. Note brighter colours represent denser minerals (ZnS and Kfs) in backscatter, compared with its surrounding silica rich matrix. EDS analysis of the K-feldspar reveals some barium present.

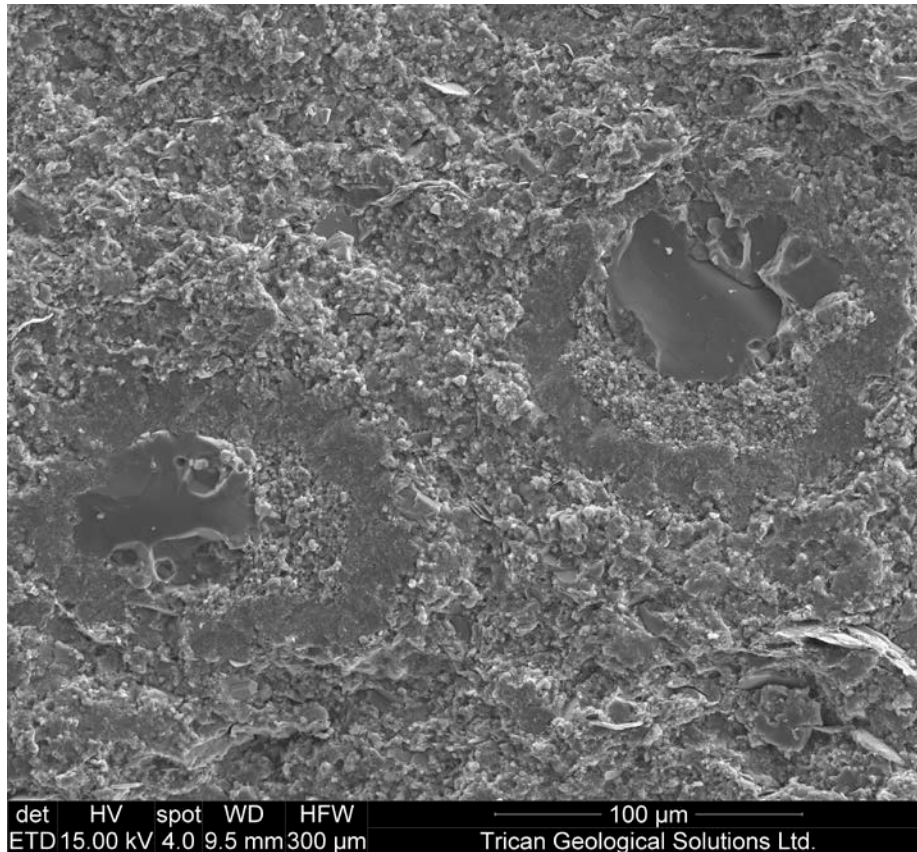


**Figure 55.** SE photomicrograph showing two siliceous algal cysts containing a solid cement core and porous quartz cement with bituminous organics surrounding core. Walls of cyst feature intracrystalline porosity.

The remaining framework components are comprised of pyrite and feldspar. Pyrite is estimated to comprise 1-2% of sample composition. Pyrite is observed most commonly as octahedral crystals 3- 15 µm in size, but is also present in framboidal form 5-10 µm in size (diagenetic origin). Feldspar grains are less common, but EDS analysis of the K-feldspars (5-35 µm) often shows that these grain have small amounts of barium (*diagenetic origin due to Ba from the organic matter/seawater interaction?*) These grains are lighter colour than normal (usually similar tone to quartz) and are found associated with sphalerite.

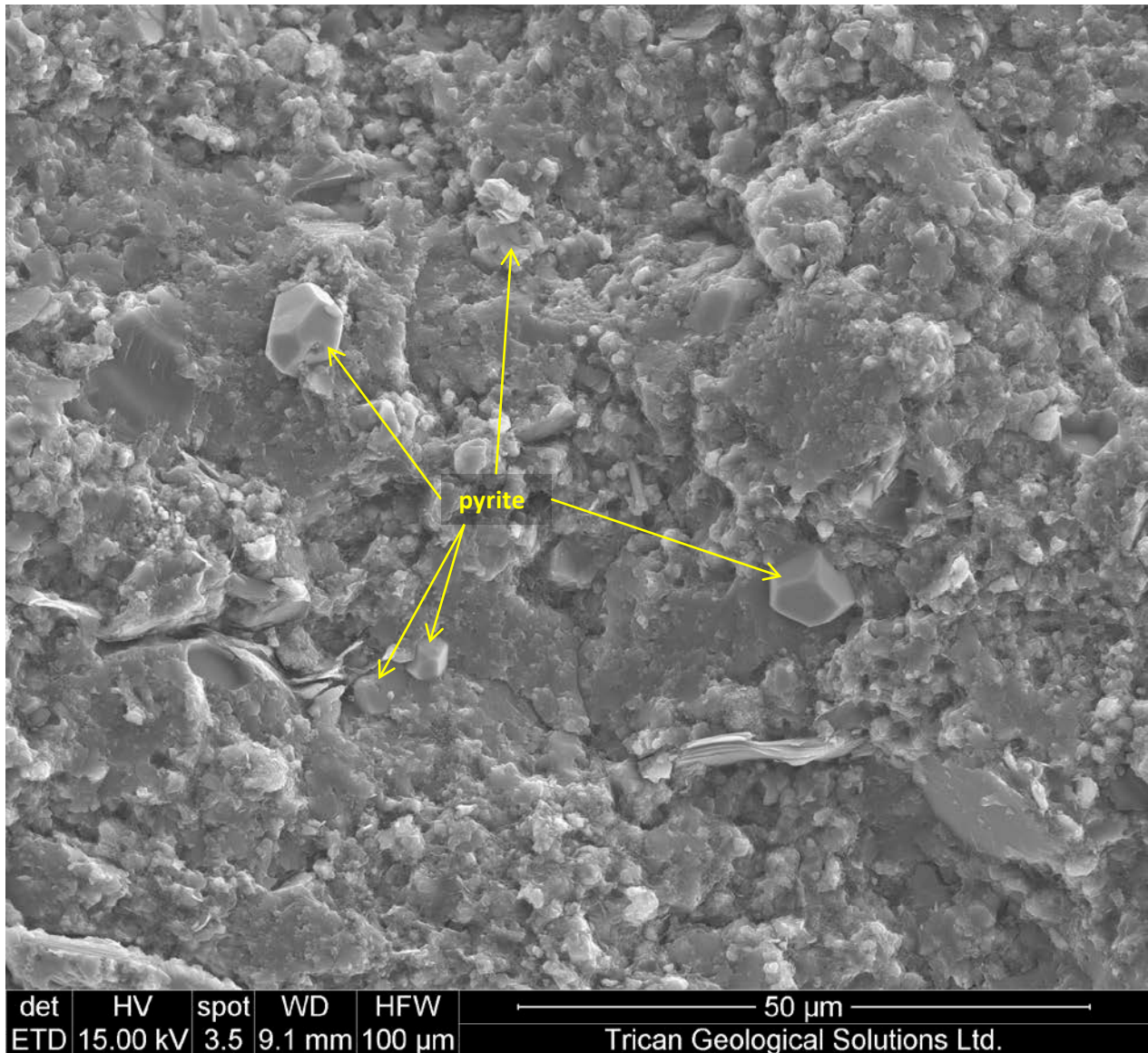


**Figure 56.** SE photomicrograph showing euhedral octahedral pyrite crystals embedded within a quartz- and organic- rich matrix. The image also features mica sheets protruding from quartz cements.

**GROUNDMASS** The “matrix” in this sample is dominated by abundant neofomed quartz “mass” (cements) that encompass microcrystalline quartz grains (<1 μm) and mica sheets. Cements are more pervasive and advanced in comparison to other samples. Any significant intercrystalline void space at cement grain contacts is lined by bituminous organic matter. The matrix also contains calcite (irregular habit) and feldspar (blocky habit), both grains of size under <5-10 μm.

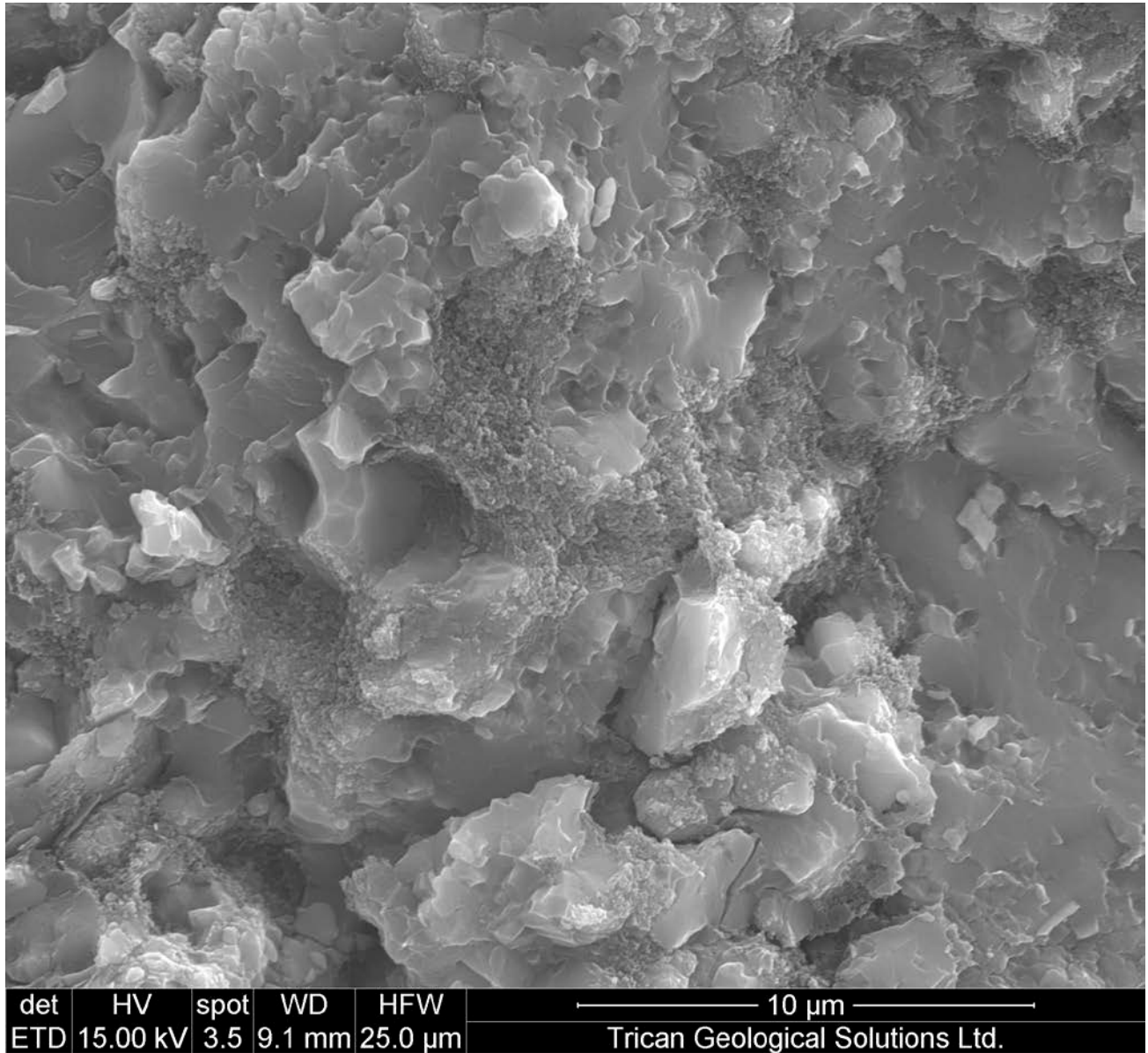


**Figure 57.** SE photomicrograph showing ubiquitous quartz cements with abundant bituminous organic matter, and some fine clay minerals. Note how organics line and fill dissolution void spaces.

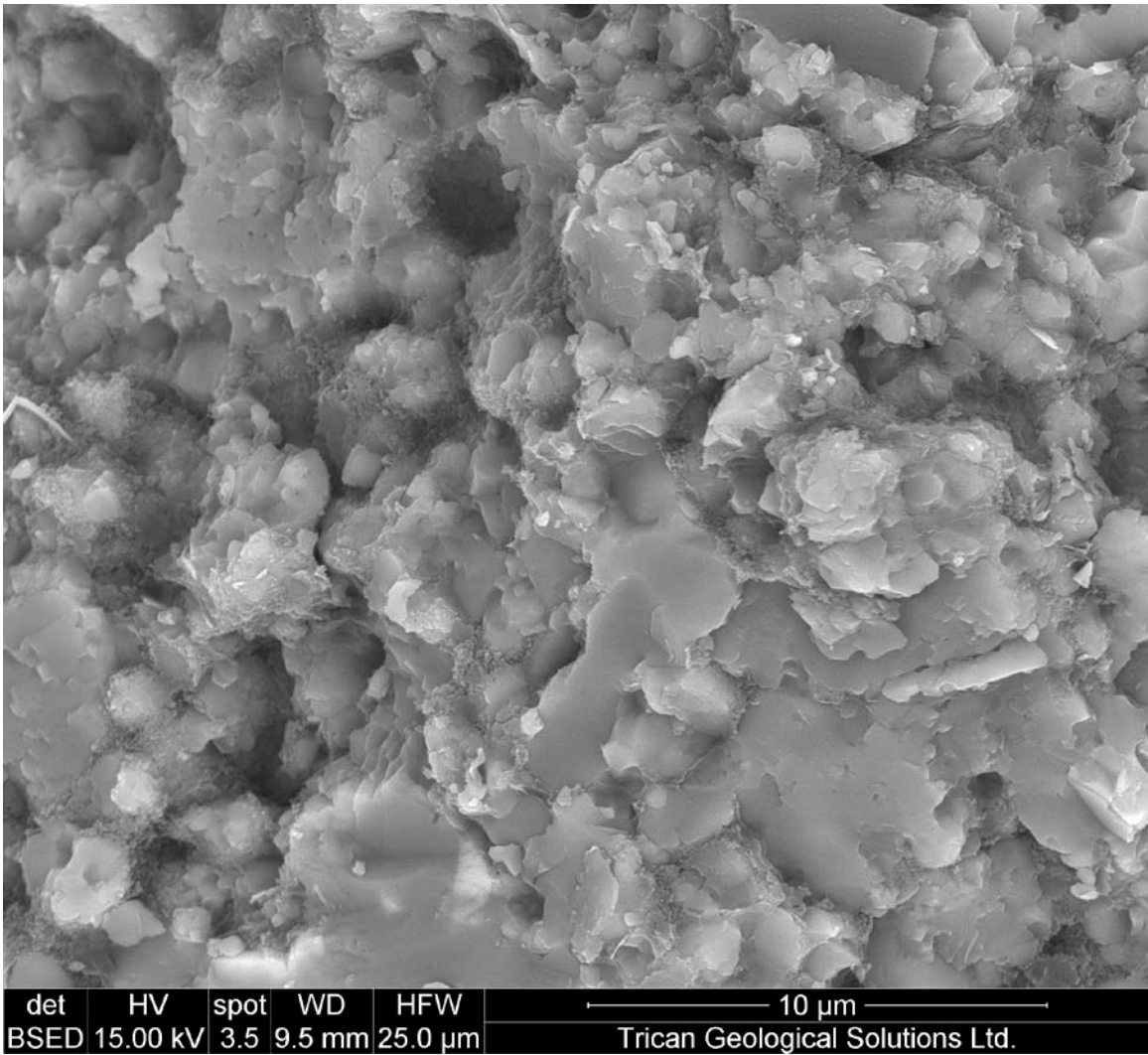


**Figure 58.** BSE photomicrograph showing ubiquitous quartz cements, with abundant bituminous organic matter, and some fine clay minerals. Note how organics line and fill dissolution void spaces.

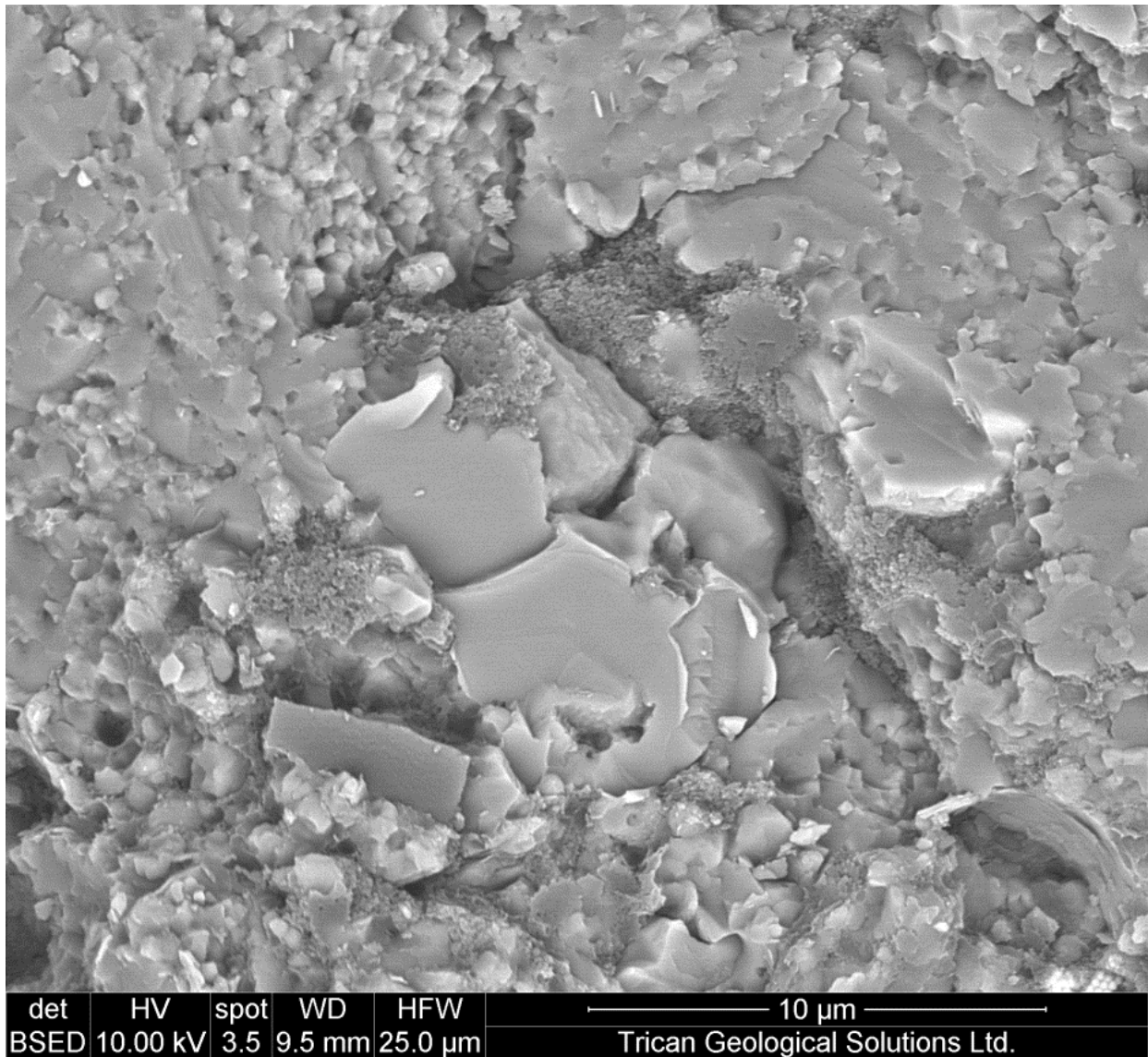


**Figure 59.** BSE photomicrograph showing a cluster of calcite grains at center surrounded by abundant bituminous organic matter, within a quartz-rich matrix. Note solid bitumen particle SW of calcite cluster.

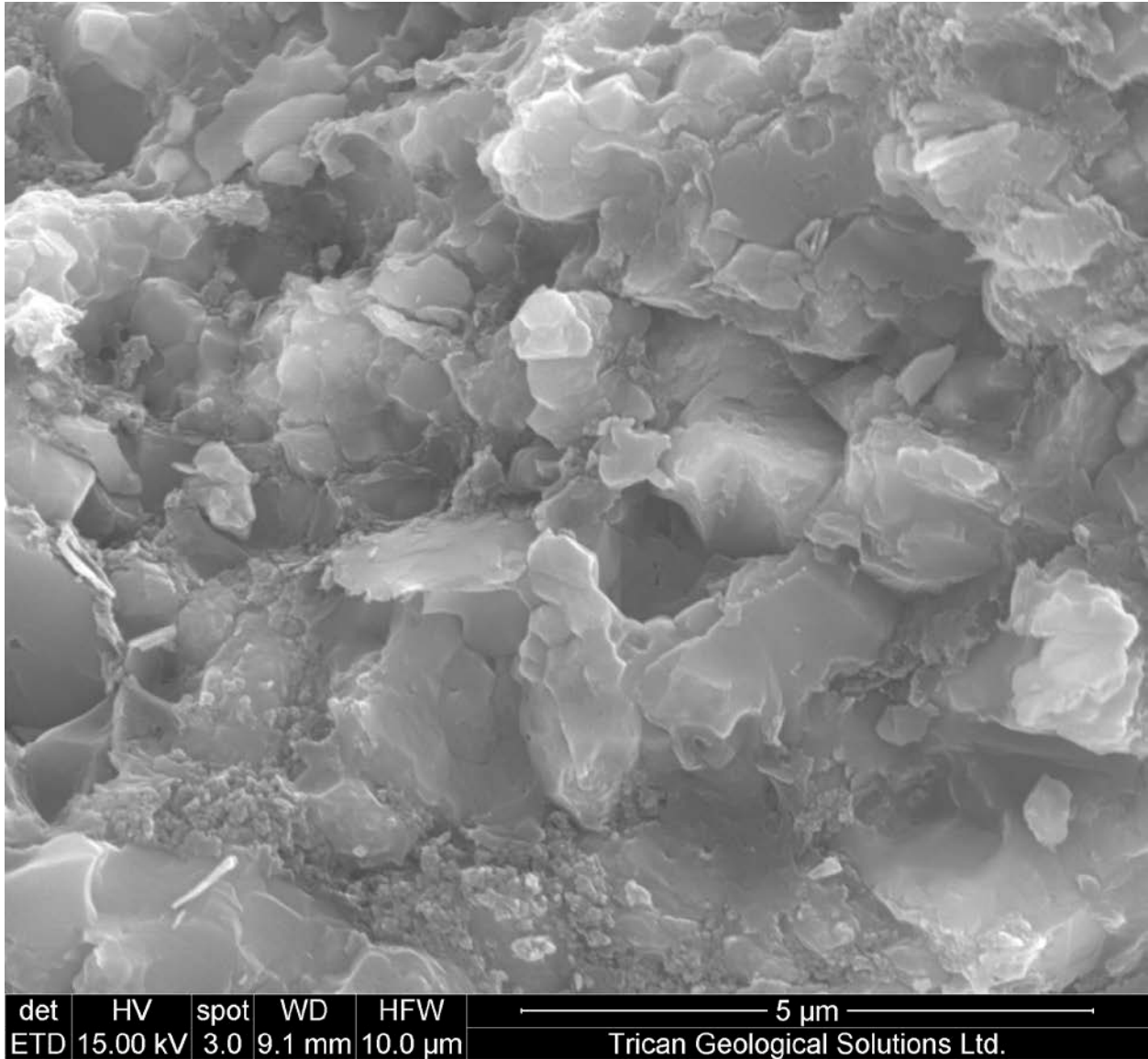


**Figure 60.** SE photomicrograph showing ubiquitous quartz grains/cements with some fine clay minerals and bituminous organic matter. Note dissolution void space and nm-scale intracrystalline pores in quartz.

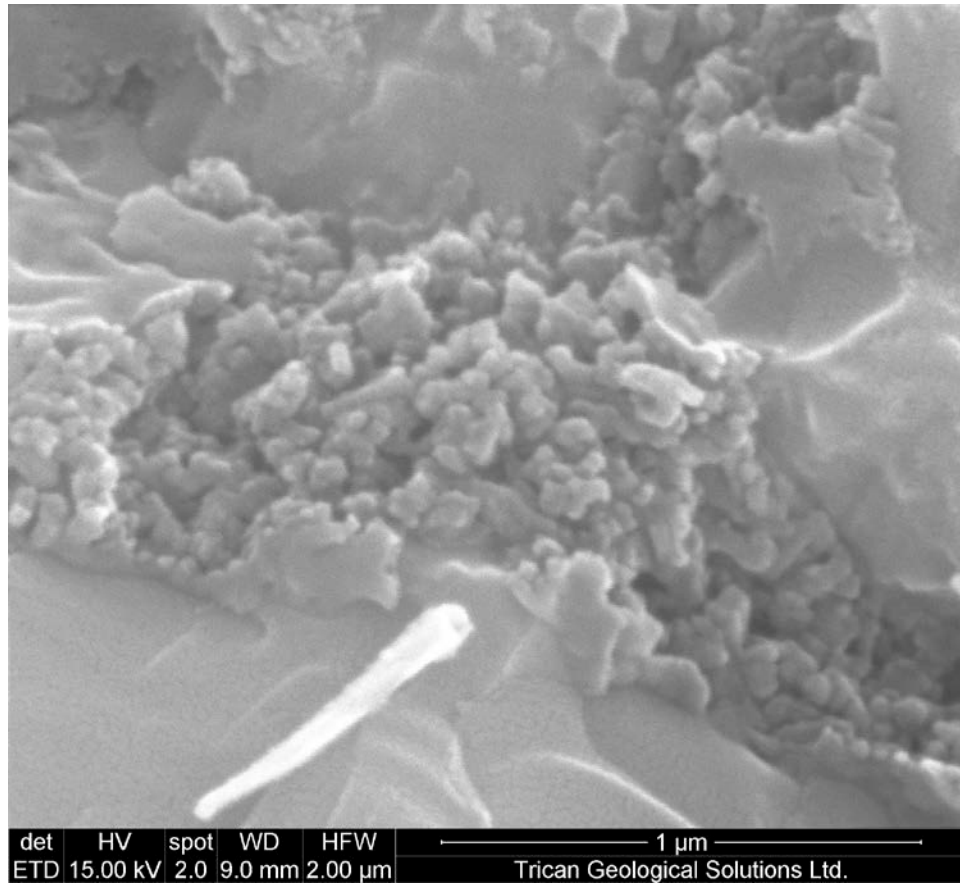


**Figure 61.** SE photomicrograph of organic matter that permeates the quartz rich matrix between grains. Note intraorganic porosity present.

**POROSITY** Pore space within **sample FX-67.18c** is predominately intercrystalline and intraorganic, with the largest voids observed associated with removal (i.e. plucking) of grains during sample preparation. Intercrystalline void space, ranging from 1-12  $\mu\text{m}$  and average size of 1-3  $\mu\text{m}$ , reveals true intercrystalline porosity in material moulded around it. True Intercrystalline porosity within the matrix ranges from 50 nm -1  $\mu\text{m}$ . Ubiquitous low-density bituminous organic matter both conceals and preserves additional porosity by coating and filling void space.

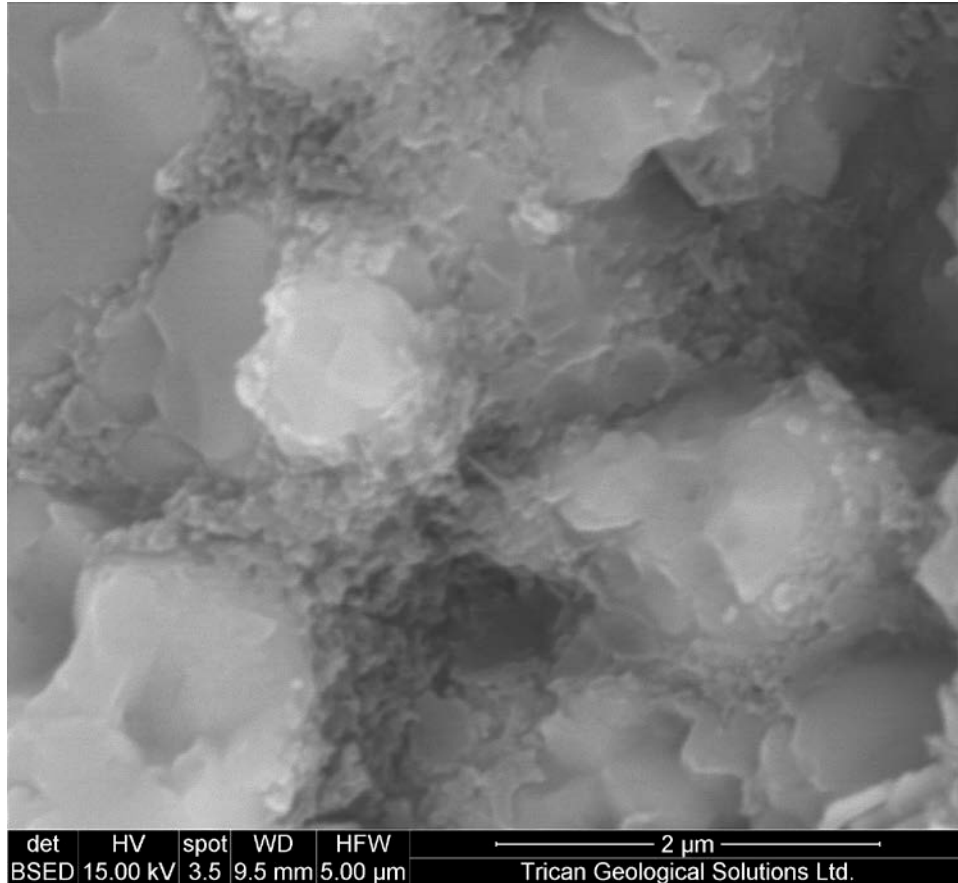


**Figure 62.** BSE photomicrograph showing details of neoformed microcrystalline quartz grains coated with bituminous organic matter and fine clay minerals. Note porous texture of organic matter between grains.

## LOWER UNIT: MUDSTONE/SHALE

---

**OVERVIEW** SEM analysis of the fresh chip samples reveals some fine to coarse silt-sized quartz/feldspar grains (5-25  $\mu\text{m}$ ) and mica sheets (<10-15  $\mu\text{m}$ ) and, embedded within a matrix of permeating quartz cement, neoformed microcrystalline quartz grains, fine clay minerals, feldspar, and pyrite. Most silt-size grains (quartz and feldspar) have smooth surfaces which imply a late diagenetic growth (i.e. secondary origin).

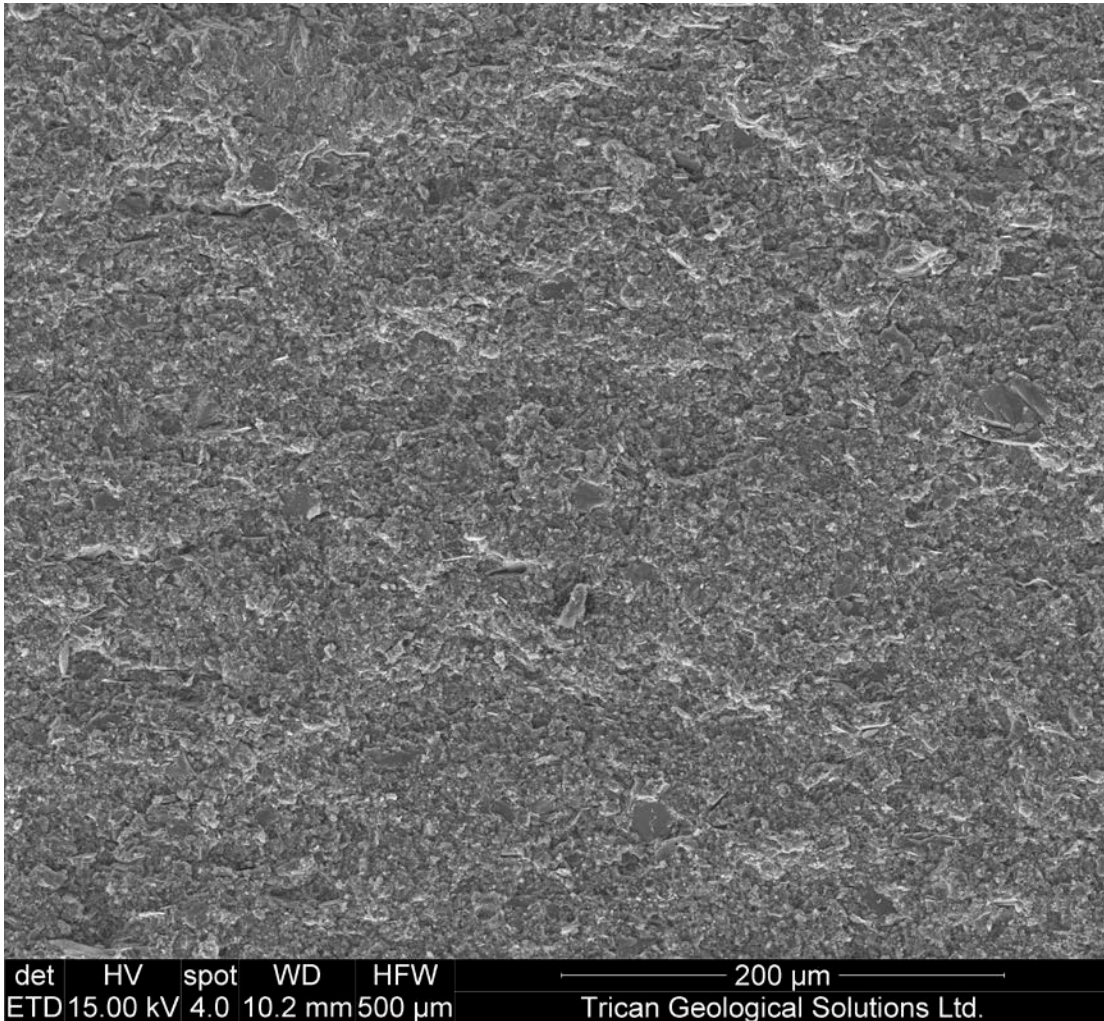


**Figure 63.** SE photomicrograph showing overview of texture and lamination within sample FX-67.18c. Sample features silt-size mica sheets and cements, embedded within a granular organic- and quartz-rich nanometer-scale grain matrix.

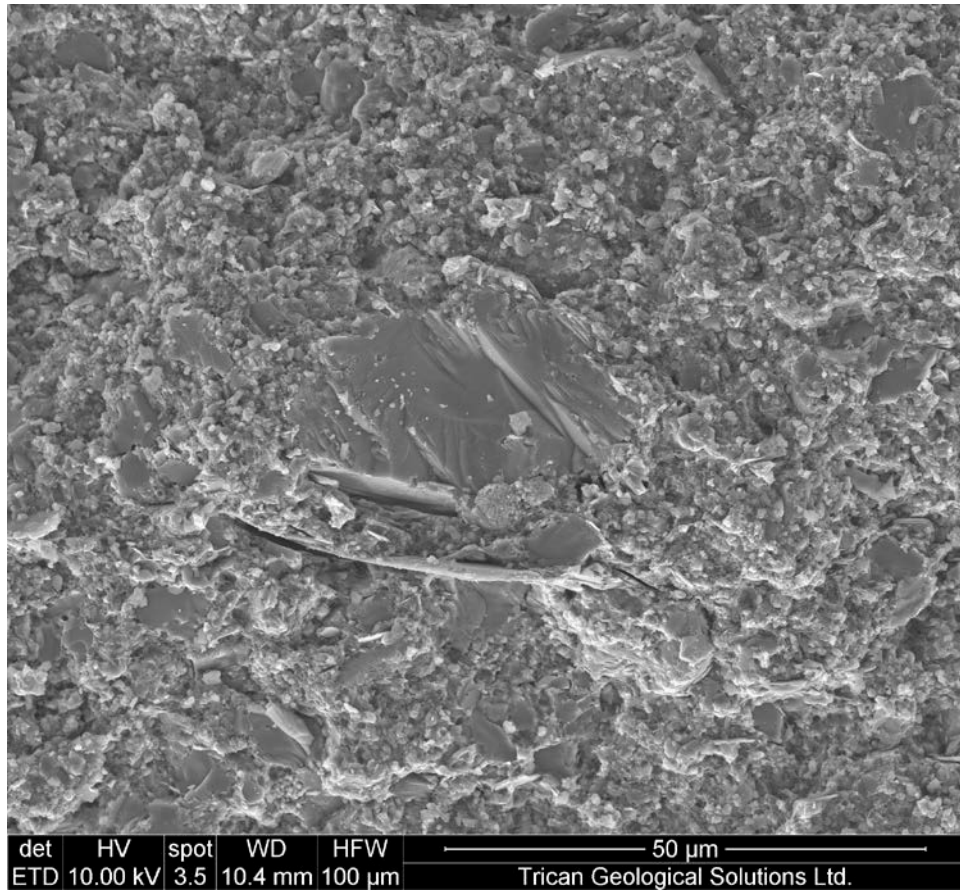


**Figure 64.** SE photomicrograph showing neomorph K-feldspar infilling possible an elongate former microfossil. Framboidal pyrite at base of feldspar is also observed as well as voids left by removal of mica sheets during sample prep.

**FRAMEWORK** The primary framework component of **sample FX-67.18c** is quartz, comprising approximately 60-70% of the sample volume. Most of the quartz is observed as silt-size grains with smooth surfaces (cements), ranging in size from 3-20 μm, as well as abundant neofomed microcrystalline quartz grains which form the “matrix”. Because these grains are so small, petrographic thin sections, which are ~25-30 μm thick, provide information only about the largest grains and the overall texture in this sample.

The second most abundant framework components in this sample are feldspar grains and mica sheets. Feldspar grains range in size up to 30 μm, and tend to be larger than quartz grains. Feldspar often exhibit bladed or blocky habit, with intracrystalline porosity (150-500 nm). Mica sheets (5-40 μm) impart a subtle lamination on the sample and are oriented parallel (larger sheets) and sub parallel (smaller flakes) relative to the planar bedding.

The remaining framework components are comprised of framboidal or octahedral pyrite (average 3-10 μm), barite micro crystals or cements (2-5 μm), and sphalerite (ZnS) cements (5-15 μm). Barite is observed as blocky euhedral crystals and platy chips filling dissolution void space ranging in size from 2-5 μm. Figure 65 shows an example of some concentrated lenses of Barite observed (75-100 μm), which are often associated with pyrite. A single pyrite replaced microfossil 8 μm is observed, filled with low density bituminous organics.

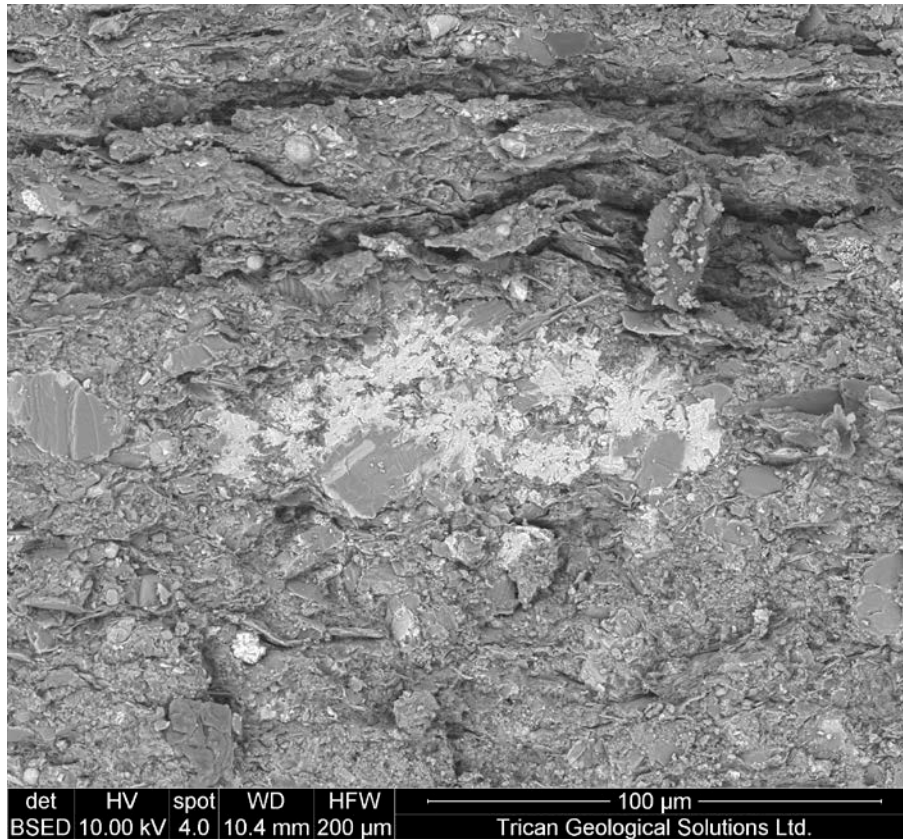


**Figure 65.** BSE photomicrograph showing lenses of barite cementation, intergrown with K-feldspar crystals.

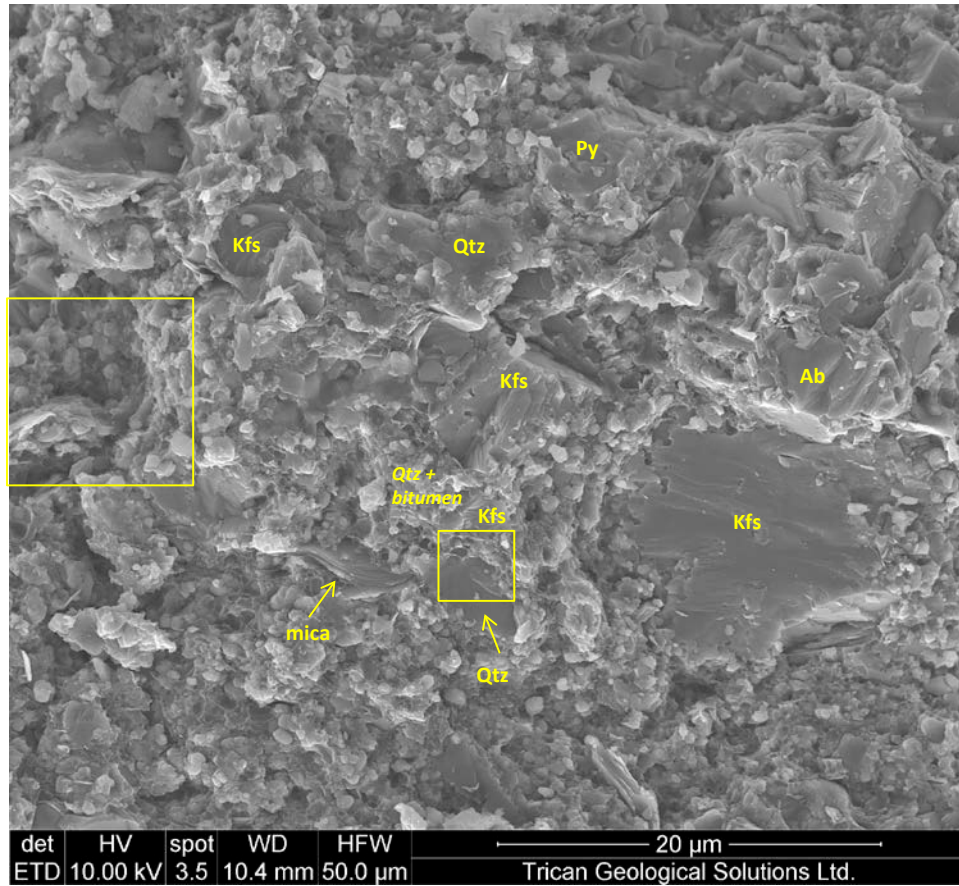


**Figure 66.** SE photomicrograph showing neomorphic K-feldspar, quartz, albite, and pyrite crystals within a matrix of microcrystalline quartz grains, clay minerals, and organic matter. Yellow boxes are featured in Figures 67 and 68.

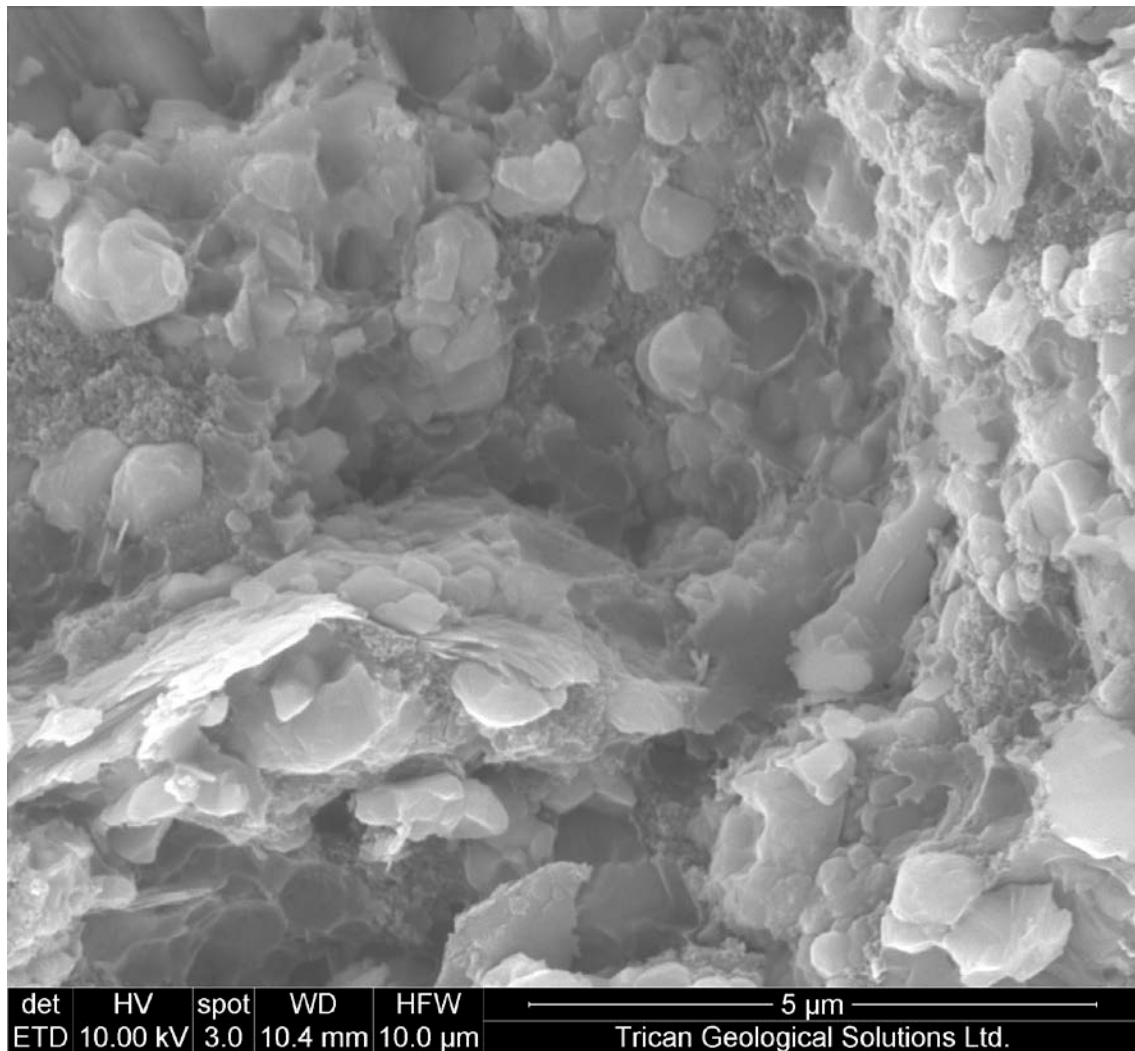


**Figure 67.** SE photomicrograph showing neofomed microcrystalline quartz grains, and low-density porous bitumen with clay sheets, all surrounded by permeating quartz cements.

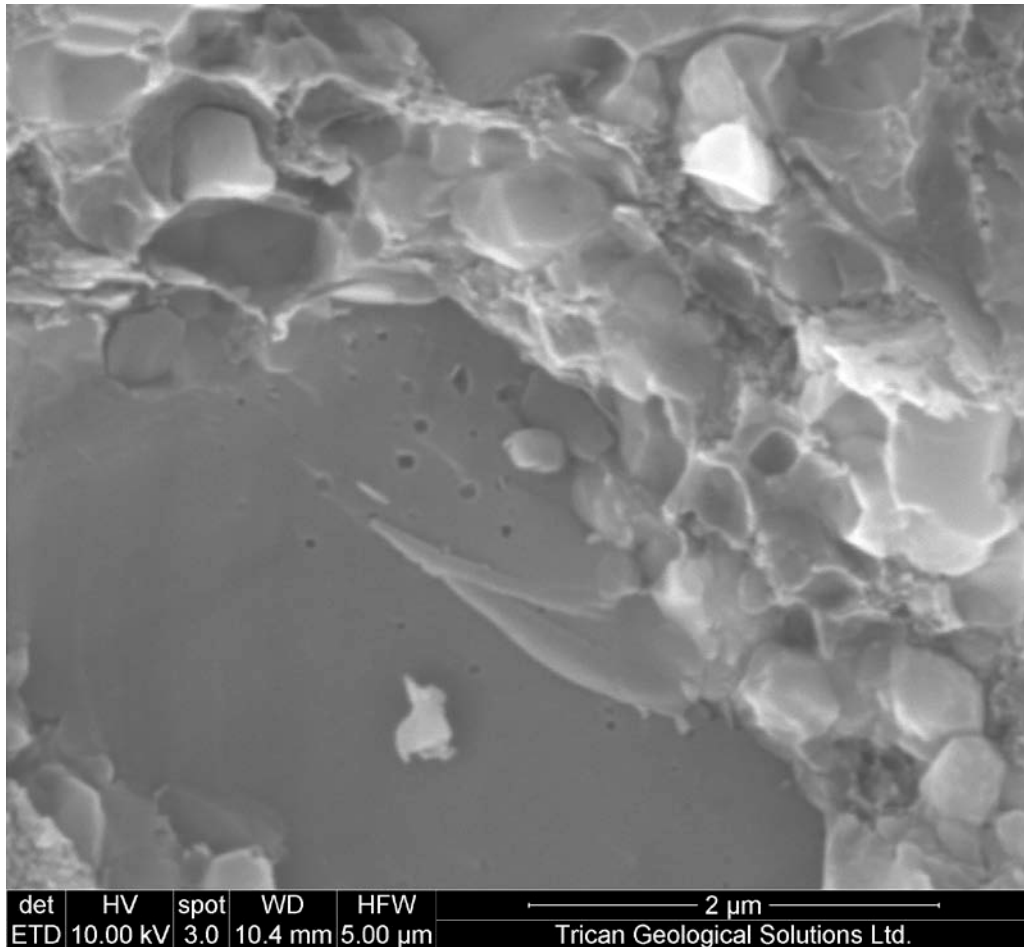


**Figure 68.** SE photomicrograph showing intracrystalline porosity in neomorph quartz grain. Flat surface likely produced by removal of mica sheet. Note microcrystalline quartz grains, and bitumen surrounding, filled by permeating quartz cements in matrix.

**POROSITY** Pore space within **sample FX-67.18c** is predominately intercrystalline, with some intracrystalline porosity within cements. The largest voids observed are associated with grain plucking of mica sheets during sample prep. Intercrystalline porosity associated with mica sheets in-situ (not removed) ranges from 100-800 nm. Intercrystalline porosity in the matrix ranges from 50 nm -1 μm and often includes dissolution and grain pluck voids, exposing surrounding cements. Finally, 50-600 nm intracrystalline pores are observed in blocky feldspar cements. Ubiquitous low-density bituminous organic matter both conceals and preserves additional pore space.

## SAMPLE FX-73.7

The mineral composition of **sample FX-73.7** by XRD refinement is comprised of mainly quartz (58%), with lesser amounts of feldspar (19%), mica/illite (11%), pyrite (7%), carbonates (3%) and natrolite (zeolite group) (2%). The total organic carbon content of the sample is extremely high at 14.06 wt-%.

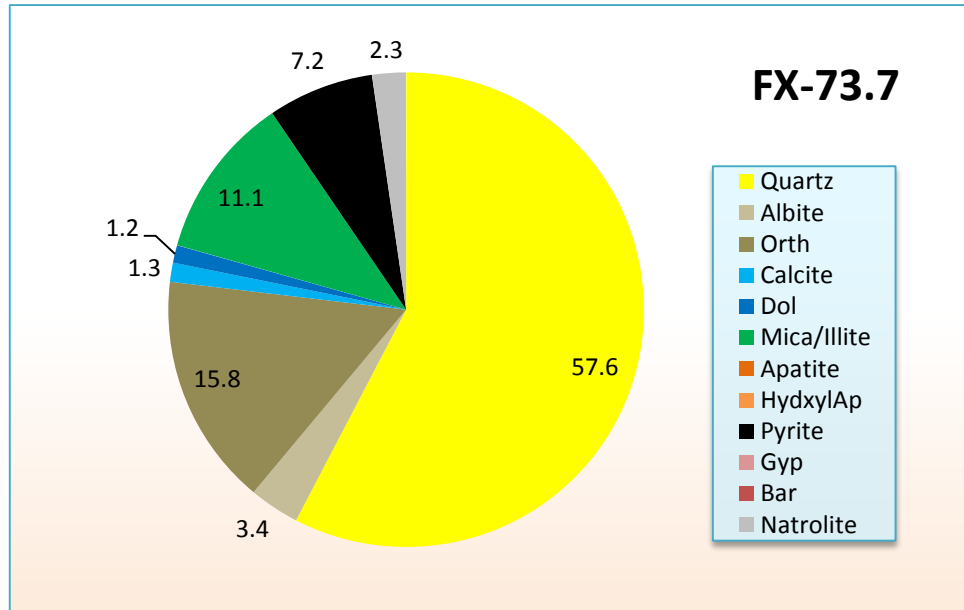


**Figure 69.** Pie-diagram of the mineralogical composition of sample FX-73.7 determined by XRD analysis. This composition is dominated by quartz, with lesser amounts of feldspar, clay minerals, pyrite, carbonates, and the zeolite natrolite.

---

## SEM ANALYSIS

---

**OVERVIEW** SEM analysis of the fresh chip samples reveal some fine silt-sized feldspar, quartz, and mica sheets embedded within a granular clay size matrix of neoformed microcrystalline quartz, organic matter, and clay minerals. The clay sheets (mica and chlorite) are oriented sub parallel, and impart a subtle lamination on the overall texture of the sample. The silt-sized feldspar and quartz often feature clean smooth surfaces, implying late diagenetic growth (i.e. secondary origin).

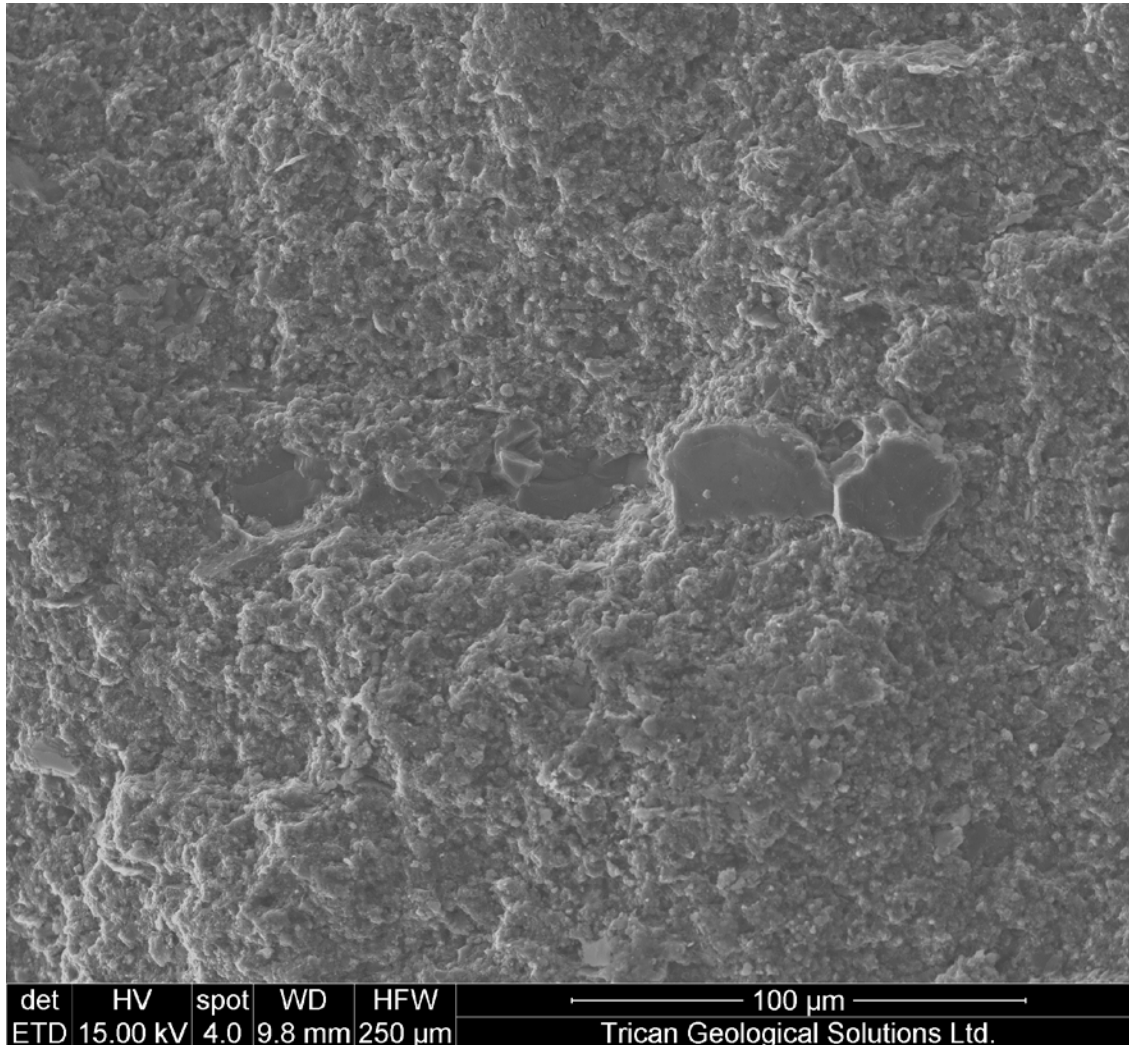


**Figure 70.** SE photomicrograph showing possible quartz-replaced microfossil of algal origin, within a clay size matrix of quartz, organic matter and clay minerals. Note mica sheets impart subtle lamination on overall texture of sample.

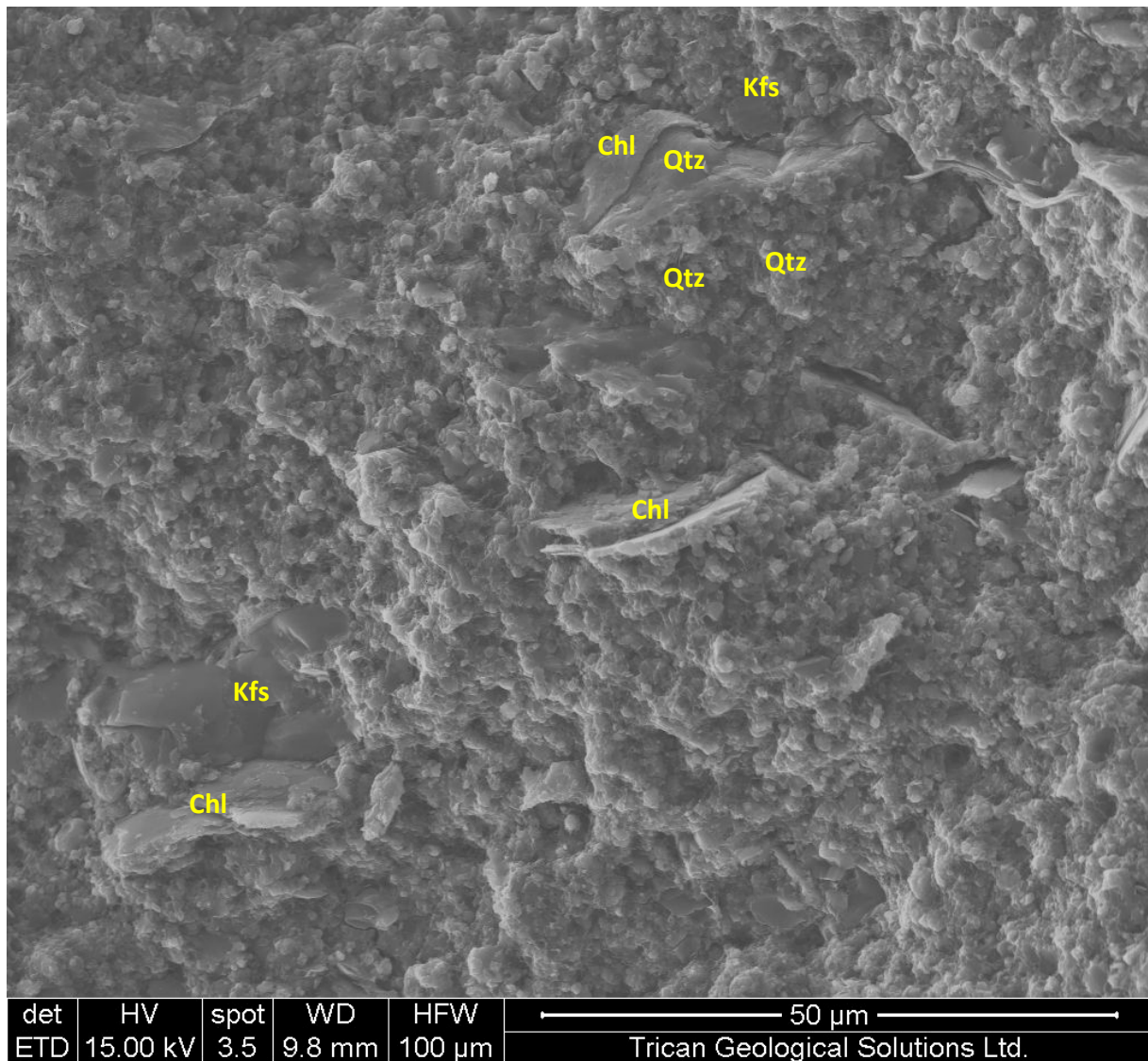


**Figure 71.** SE photomicrograph showing some K-feldspar, quartz, and clay grains within a clay-size matrix of organic matter, neoformed microcrystalline quartz, and illite/mica. Note intergranular void space associated with clay sheets may be due to material removed during sample preparation.

**FRAMEWORK** The primary framework constituent of **sample FX-73.7** is quartz, comprising approximately 50-60% of the sample volume. Quartz is predominately observed as clay size neofomed crystals forming the matrix, with lesser amounts of silt-sized cement particles (average 3-15  $\mu\text{m}$ ). The clay size quartz component is discussed further in the matrix description.

The remaining silt-sized cement particles include clay sheets, feldspar and calcite. Clay sheets include chlorite and mica and range in size from 5-35  $\mu\text{m}$ , average 10  $\mu\text{m}$ . Clay sheets in the 5-10  $\mu\text{m}$  range are often randomly oriented. K-feldspar is the next most abundant framework grain ranging in size from 5-15  $\mu\text{m}$ . A single instance of calcite cement is detected and was 10  $\mu\text{m}$  in size.

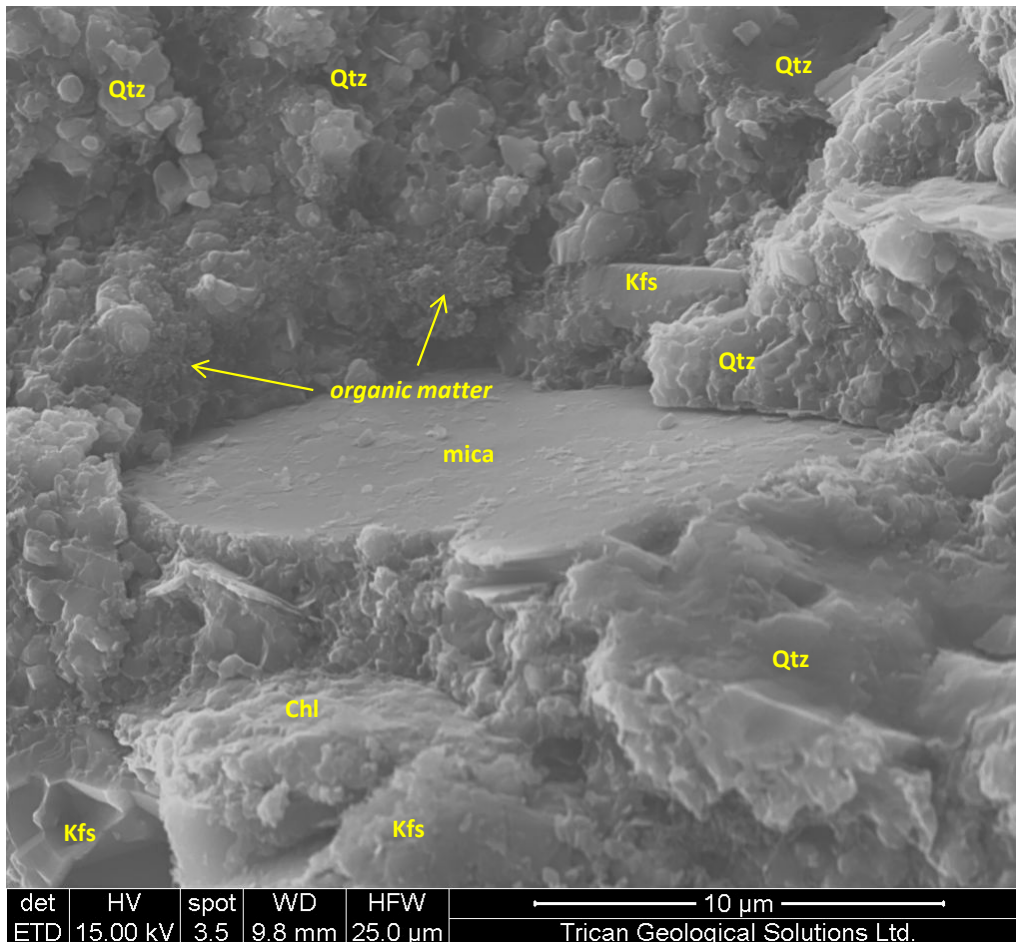


**Figure 72.** SE photomicrograph showing exposed surface mica sheet at center, surrounded by quartz and K-feldspar cements; within a matrix of microcrystalline quartz, organic matter, and clay minerals. Note fine illite flakes foliated up away from surface of mica sheet, as well as intercrystalline void space between quartz cement above mica sheet (right corner of grain).

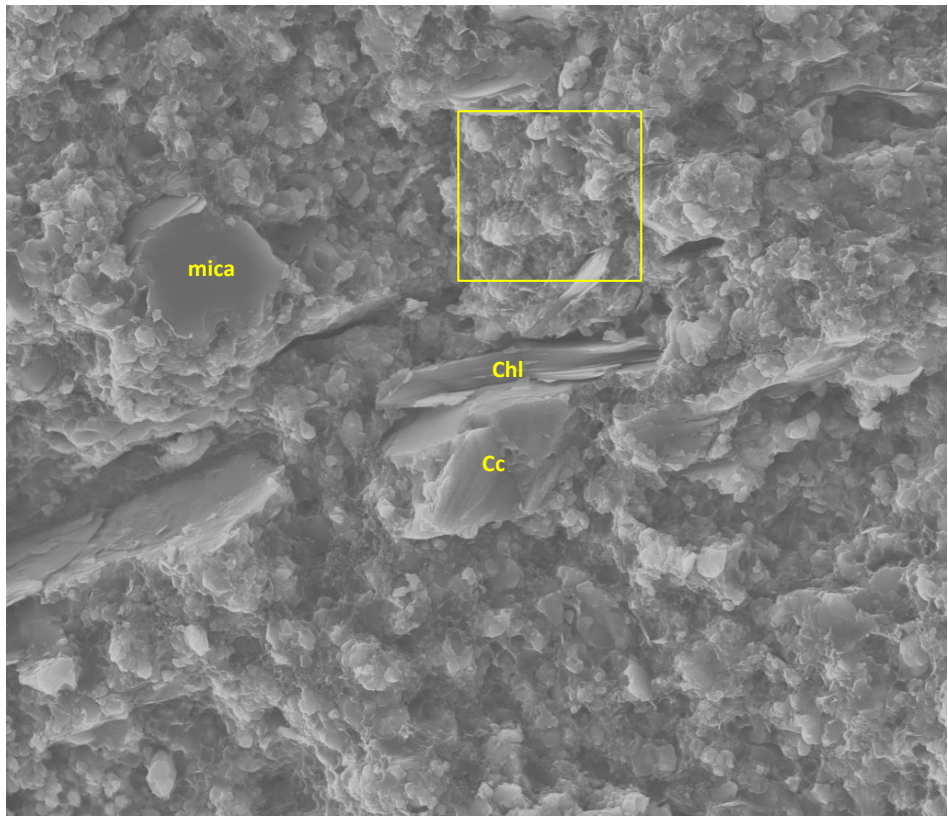
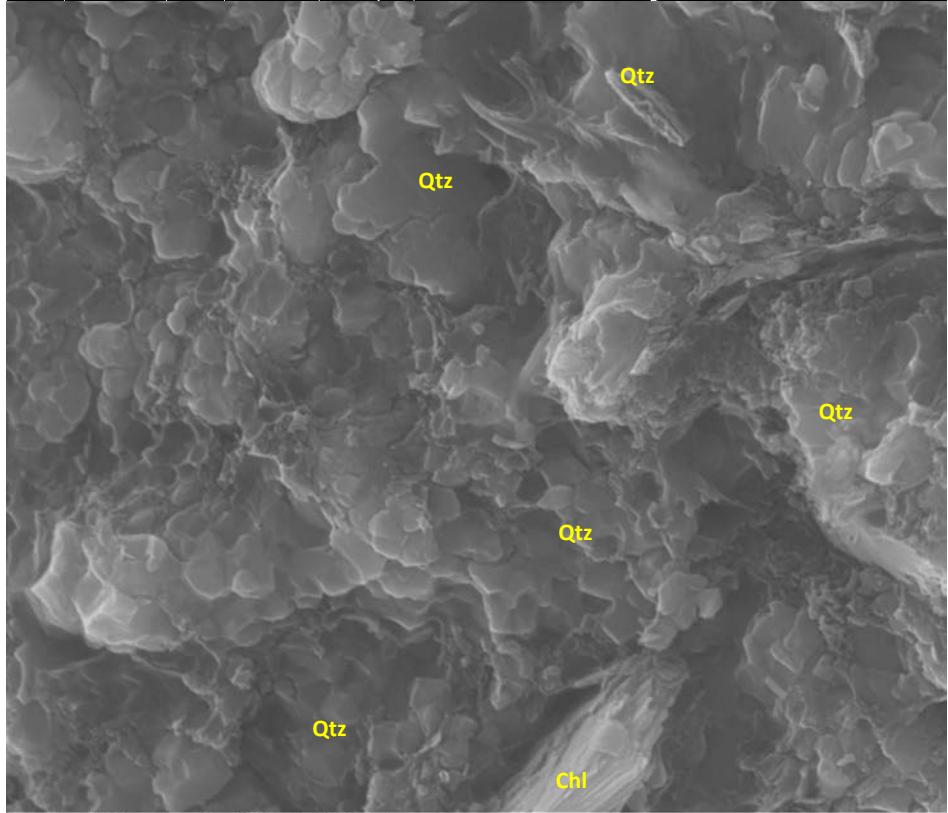


**Figure 73.** SE photomicrographs showing framework grains within clay size quartz- and organic-rich matrix.

Top: Chlorite and muscovite are observed within sample, as well as sparse calcite cements. Yellow box magnified in image below.

det	HV	spot	WD	HFV	20 $\mu$ m
ETD	15.00 kV	3.5	9.8 mm	50.0 $\mu$ m	Trican Geological Solutions Ltd.

Bottom: clay size neoformed microcrystalline calcite, showing granular crystals, with overgrowths cementing them together, as well as amorphous cements (top right).



det	HV	spot	WD	HFV	5 $\mu$ m
ETD	15.00 kV	3.0	9.8 mm	10.0 $\mu$ m	Trican Geological Solutions Ltd.

**GROUNDMASS** *Sample FX73.7* features very fine silt-sized grains suspended within a groundmass of clay size neoformed quartz, clay minerals and bituminous organics. The ubiquitous microcrystalline quartz crystals range in size from 200 nm up to 1-2  $\mu\text{m}$ . Fine grained illite is dispersed within the sample. “Super-fine” low-density bituminous organics are line cavities and fill pore space, while fine clays tend to coat grains.

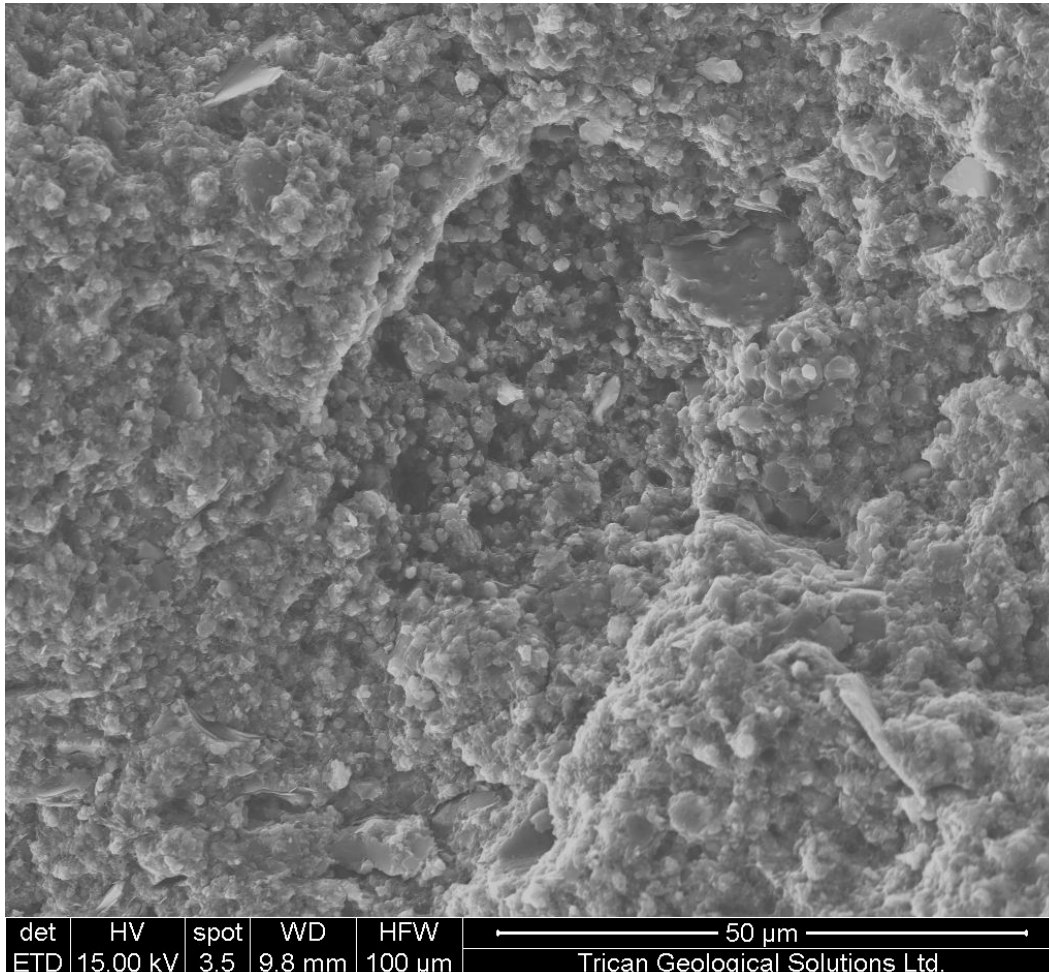


Figure 74. SE photomicrograph showing a marquis shaped cavity, left by removal of a microfossil (possible algal cyst). Note low-density (dark) bitumen fills pore space between sugary neoformed quartz crystals. Clay sheet at top right of cavity is chlorite.

**POROSITY** Pore space within *sample FX73.7* is predominately intercrystalline, with the largest voids associated with clay sheets. There are some large dissolution cavities that are likely due to grain plucking, ranging in size from 800nm to 4  $\mu\text{m}$ . The intercrystalline porosity associated with clay sheets and surrounding silt-sized cement particles ranges in size from 50-500 nm. Small dissolution pores with the clay size fraction range in size from 500-800 nm. Intercrystalline pore space between clay size neoformed quartz crystals range up to 80 nm. Some intracrystalline pore space in the form of residual growth pores are observed up to 150 nm. Low density porous organic matter both conceals and preserves additional porosity by coating and filling void space and featuring 5-50 nm pores within organic matter network.

## *Conclusions*

Petrographic and scanning electron microscopy (SEM) analyses for 4 samples of the Chevron Core Project from the Canol Formation were performed in order to better understand textural and compositional variability (or homogeneity). Pore structures and diagenetic overprints were also investigated. All samples show characteristics of fissile, finely laminated organic-rich siliceous shales/mudstones. The investigations revealed that most of the samples contain high amounts of diagenetic quartz derived most likely from biogenic silica of phytoplankton debris.

The FX samples are black organic-rich (up to 14 wt-% TOC) shales/mudstones with 50-90% quartz and feldspars and clay minerals (mica, illite). Trace amounts of carbonates are also present. These rocks are very fine-grained (mostly <10  $\mu\text{m}$ ) with some silt-size grains of mica, feldspars, pyrite, quartz and carbonates (dolomite, calcite). Quartz permeates the entire sample and forms idiomorphic microcrystalline grains (0.5-3  $\mu\text{m}$ ) but also occurs as cements between grains and organic material (incl. bitumen). Some thin beds can exhibit a "silty appearance" which makes the rock samples look like siltstones (sample FX-67.18) but SEM analysis reveal that the "silty" grains are recrystallized microfossils (possibly tasmanite or dasycladacean cysts). The cements are dominated by quartz but carbonate material is also found along the margins (overgrowth- secondary diagenetic growth). Algal remains are the dominant component of the organic matter. Several other microfossils are occasionally observed including possible planktonic radiolarian, gastropods, and pteropods. Most algal remains show replacement by quartz but mica and pyrite can also be observed within their structures together with abundant either dispersed or solid bituminous material. The paleoenvironmental setting of these samples may have been a shallow marine basin with restricted detrital influx (distal to the shoreline) and anoxic bottom water conditions. Detrital influx of feldspars, quartz, and mica occurred but only medium to fine silt-size particles (except for mica sheets) were transported and deposited at the location. Minimal bottom water currents disturbed the sediments resulting in these laminated shales/mudstone rocks.

In summary, these samples provide information about their origin and depositional settings. The high quartz and algal content of the samples together with the limited detrital component infers that these samples were deposited within a shallow marine basin with restricted detrital influx and highly stratified ocean where the bottom water was calm and anoxic due to the constant influx of organic matter. No bioturbation is evident in any of these rock samples. Some thin beds with high amounts of plankton material are present but there is little evidence that prolific algal blooms similar to modern upwelling settings occurred. In contrary, normal algal growth appears to have been the norm in the past during the deposition of these sediments. During early diagenesis, dolomite and pyrite formation occurred, followed by burial and late diagenesis, resulting in silicification and microfossil replacements, as well as organic maturation and migration of certain HC fractions.

Principal Authors:

Raphael A.J Wust, PhD, P.Geo.  
Technical Advisor  
*Trican Geological Solutions Ltd.*

R. Marc Bustin, PhD, P.Geo, FRSC  
Technical Advisor  
*Trican Geological Solutions Ltd.*

Ron Brezovski, P.Geol  
President  
*Trican Geological Solutions Ltd.*

Brent Nassichuk, MSc  
Technical Manager  
*Trican Geological Solutions Ltd.*

Heather Offord, BSc, Geol.I.T.  
Geologist  
*Trican Geological Solutions Ltd.*

## **DISCUSSION OF FINDINGS**

Analysis of the Canol core samples from FX07-03 corroborates the unusually high levels of organic matter richness identified previously (Frasier, 2012). The presence of solid bitumen infilling some pore networks observed in SEM and infilling fractures (FX07-03\_73.7m) would contribute to a portion of the measured TOC. High levels of thermal maturity are indicated by the dormant response upon pyrolysis.

Measurements of unconfined porosity and permeability indicate good reservoir quality and high gas storage potential within the Canol with SEM evaluation indicating visible porosity is associated with both degraded organic matter and intercrystalline pores. Microporosimetry results corroborate the presence of porosity but at lower average values presumably due to limited mercury intrusion into finer pores. Pore throat sizes in the range of 3-10nm dominate suggesting typical shale reservoir pore size ranges with finer sizes remaining unresolvable. Investigations of the architecture of porosity network and degree of connectivity would require additional and different forms of analysis.

The mineralogy of the Canol from XRD is dominated by biogenic silica but clays and feldspars being more abundant than described elsewhere and suggests a potential clastic component and different provenance in the lower part of the Canol from which the samples originated. Anomalous quantities of apatite in one sample suggest phosphate-enrichment in association with high primary organic matter productivity and preservation. Sphalerite mineralization replacement of microfossils is suggestive of SEDEX type mineralization processes.

## **APPENDIX**

### **Appendix A – Trican Disclaimers**

#### Trican Disclaimer – SRA

##### DISCLAIMER

All data in this report was obtained using a Source Rock Analyzer (SRA). Trican Geological Solutions Ltd. shall not, except in the case of gross or wilful negligence on our part, be liable or responsible for any loss, costs, damages or expenses incurred or sustained by anyone resulting from any interpretation made by our officers, agents, or employees.

Trican Geological Solutions Ltd. does not represent that this communication, including any files attached, is free from computer viruses or other faults or defects. Trican Geological Solutions Ltd. will not be liable to any person for any loss or damage, including direct, consequential or economic loss or damage however caused, and whether by negligence or otherwise may result directly or indirectly from the receipt or use of this communication or any files attached to this communication.

#### Trican Disclaimer – XRD

##### Disclaimer

All interpretations are opinions based on data obtained through quantitative Rietveld analysis using Jade software. TRICAN GEOLOGICAL SOLUTIONS LTD. shall not, except in the case of gross or wilful negligence on our part, be liable or responsible for any loss, costs, damages or expenses incurred or sustained by anyone resulting from any interpretation made by our officers, agents, or employees.

TRICAN GEOLOGICAL SOLUTIONS LTD. does not represent that this communication, including any files attached, is free from computer viruses or other faults or defects. TRICAN GEOLOGICAL SOLUTIONS LTD. will not be liable to any person for any loss or damage, including direct, consequential or economic loss or damage however caused, and whether by negligence or otherwise may result directly or indirectly from the receipt or use of this communication or any files attached to this communication.

#### Trican Disclaimer - Porosity and Permeability Analysis

##### Disclaimer

All interpretations are opinions based on inferences from geophysical logs and rock experiments. Trican Geological Solutions cannot and does not guarantee the accuracy or correctness of any interpretations, and we shall not, except in the case of gross or wilful negligence on our part, be

liable or responsible for any loss, costs, damages or expenses incurred or sustained by anyone resulting from any interpretation made by our officers, agents, or employees.

Trican Geological Solutions does not represent that this communication, including any files attached, is free from computer viruses or other faults or defects. Trican Geological Solutions will not be liable to any person for any loss or damage, including direct, consequential or economic loss or damage however caused, and whether by negligence or otherwise may result directly or indirectly from the receipt or use of this communication or any files attached to this communication.

#### Trican Disclaimer – Mercury Porosimetry

##### Disclaimer

All interpretations are opinions based on inferences from geophysical logs and site specific experimental apparatus and software. TRICAN GEOLOGICAL SOLUTIONS LTD shall not, except in the case of gross or wilful negligence on our part, be liable or responsible for any loss, costs, damages or expenses incurred or sustained by anyone resulting from any interpretation made by our officers, agents, or employees.

TRICAN GEOLOGICAL SOLUTIONS LTD does not represent that this communication, including any files attached, is free from computer viruses or other faults or defects. TRICAN GEOLOGICAL SOLUTIONS LTD will not be liable to any person for any loss or damage, including direct, consequential or economic loss or damage however caused, and whether by negligence or otherwise may result directly or indirectly from the receipt or use of this communication or any files attached to this communication.

#### Trican Disclaimer – Petrographic & SEM Analyses

##### Disclaimer

All interpretations are opinions based on petrographic analysis using an Olympus BX51 petrographic microscope and on SEM analysis using a FEI Quanta 250 ESEM. Trican Geological Solutions Ltd. shall not, except in the case of gross or wilful negligence on our part, be liable or responsible for any loss, costs, damages or expenses incurred or sustained by anyone resulting from any interpretation made by our officers, agents, or employees.

Trican Geological Solutions Ltd. does not represent that this communication, including any files attached, is free from computer viruses or other faults or defects. Trican Geological Solutions Ltd. will not be liable to any person for any loss or damage, including direct, consequential or economic loss or damage however caused, and whether by negligence or otherwise may result directly or indirectly from the receipt or use of this communication or any files attached to this communication.

## Appendix B – TOC and SRA Analysis Notes

*Modified from: Gas Shale Geology and Engineering – Application to Exploration and Development*

*Short Course Notes and Agenda Oct. 10 and 11<sup>th</sup>, 2002, R. M. Bustin, CBM Solutions Ltd. **Copyright***

### Organic Matter Content, Composition and Maturity

Abundance, composition and maturity of the organic matter determine the gas sorption capacity and thus the reservoir capacity for gas. Therefore, determining and identifying abundance, type and maturity of the organic matter are required as a routine part of gas shale characterisation.

### Total Organic Carbon Content

The total organic carbon content of rocks is obtained by heating the rock in a furnace and combusting the organic matter to carbon dioxide. At *Trican Geological Solutions* laboratory, a Weatherford Source Rock Analyzer™ is used for the analysis. The amount of carbon dioxide liberated is proportional to the amount of carbon liberated in the furnace, which in turn is related to the carbon content of the rock. The carbon dioxide liberated can be measured several different ways and the most common methodologies are the use of a thermal conductivity detector or infrared spectroscopy. During the combustion process of rock material, all organic and inorganic phases containing C produce carbon dioxide (CO<sub>2</sub>). As many source rocks also include inorganic carbon such as carbonates (notably calcite, dolomite and siderite), which break down at high temperatures, these sources also generate CO<sub>2</sub> and thus the liberated CO<sub>2</sub> must be corrected for these inorganic contributions in order to determine the organic carbon content. Generally, the amount of carbonate is determined by acid digestion (normally 50% HCl) and the carbon dioxide generated is measured and then subtracted from the total carbon content (carbon dioxide) to obtain the organic fraction as follows:

$$\text{TOC} = \text{TC} - \text{TIC}$$

TC= total carbon

TIC= total inorganic carbon

TOC = total organic carbon

However, with the SRA, the TOC is calculated from the curves as follows:

$$\text{TOC} = 0.083(\text{S}_1 + \text{S}_2)/10 + \text{S}_4/10 \text{ where the S-curves are in mg/g}$$

Many organic carbon analyses are routinely performed as part of Rock-Eval analyses (described below). The Rock-Eval combusts a crushed aliquot of rock at 600°C. At this temperature, carbonate minerals (in theory) do not decompose and the measured carbon dioxide is presumed only of organic origin. This

technique works extremely well, but some siderite apparently breaks down at temperatures less than 600° C (but none ever tested at UBC) and refractory organic matter such as inertinite does not combust readily at 600°C. Most coal samples yield Rock-Eval measured TOC values much lower than the actual values because of incomplete combustion. Rock-Eval is not recommended for use with coals or source rocks with significant amounts of Type III and IV kerogen. Kerogen is carbonaceous material (heteroatomic material) that is for the most part insoluble in common organic solvents (in contrast to bitumen).

***Definitions:***

***Kerogen: the fraction of the organic matter that is insoluble in organic solvents***

***Bitumen: the fraction of the organic matter that is soluble in organic solvents***

## **Kerogen**

The most commonly utilized scheme for classifying organic matter in sediments is based on the relative abundance of elemental C, O and H plotted graphically as the H/C and O/C ratio on a so called **Van Krevelen diagram** (Tissot et al., 1974). Rather than plot the elemental ratios it is common to plot indices determined by a pyrolysis technique referred to as Rock Eval (Espitalie et al., 1977, 1985). In the pyrolyses techniques two indices are determined: the Hydrogen Index (HI) which is milligrams of pyrolyzable hydrocarbons/TOC and the Oxygen Index (OI) which is milligrams of pyrolyzable organic carbon dioxide/TOC. Cross-plots of both elemental H/C and O/C ratios or of HI and OI are utilized to discriminate four 'fields', which are referred to as Types I, II, III and IV kerogen. These types of kerogen originate because of different kind of organic matter is deposited in the sediments and the different conditions that prevailed over geological time.

**Type I** kerogen is hydrogen rich (atomic H/C of 1.4-1.6: HI of > 700) and is derived predominantly from zooplankton, phytoplankton, micro-organisms (mainly bacteria) and lipid rich components of higher plants (H/C ratio 1.7 to 1.9).

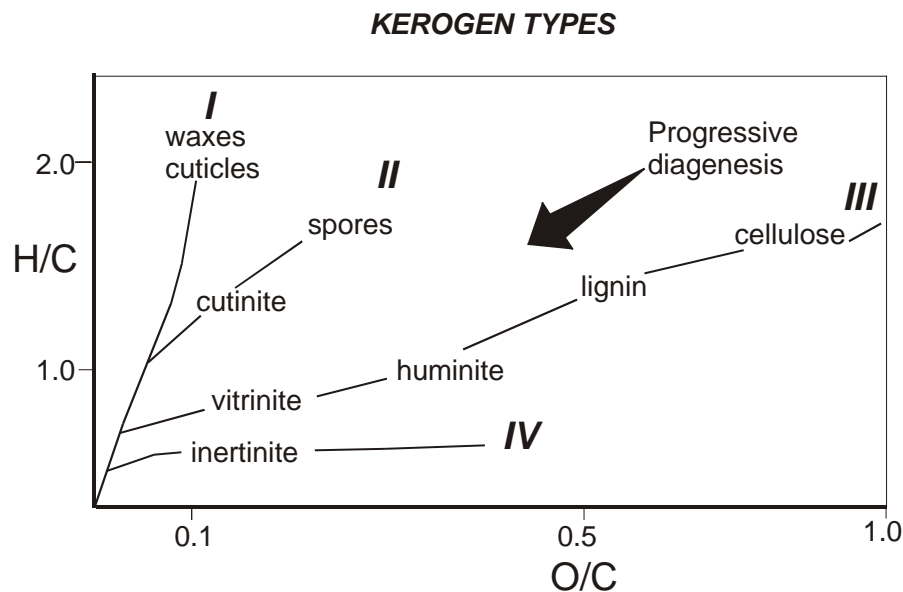
**Type II** kerogen is intermediate in composition (H/C ≈ 1.2: HI ≈ 600) and derived from mixtures of highly degraded and partly oxidized remnants of higher plants or marine phytoplankton.

**Type III** kerogen is hydrogen poor (H/C ratio 1.3 to 1.5) and oxygen rich and is mainly derived from cellulose and lignin derived from higher plants.

**Type IV** kerogen is hydrogen poor and oxygen rich and essentially inert. This organic matter is mainly derived from charcoal and fungal bodies. Type IV kerogen is not always distinguished but is grouped with Type III.

The different types of organic matter are of fundamental importance since the relative abundance of hydrogen, carbon and oxygen determines what products can be generated from the organic matter upon diagenesis. Since coal is comprised predominantly of Type III kerogen, there is little liquid hydrogen generating capacity. If the coal includes abundant hydrogen rich components (such as spores, pollen, resin, waxes- Type I or II) it will generate some liquid hydrocarbons. Although not common, some oil deposits are thought to be sourced by coals (Clayton, 1993).

The content of kerogen in the earth's crust is estimated to be  $10^{16}$  t, with most of the kerogen occurring in the clay fine silt or clay fraction deposited on continent shelf and slopes. Kerogen makes up the largest part of the total organic matter and can represent more than 95% of the weight of recent OM. The proportion of kerogen progressively changes during burial and the formation of soluble and/or volatile products, such as HCs. Hence, it is difficult to estimate the average proportion of kerogen of the total sedimentary OM {Durand, 1980}. Kerogen content is generally estimated on the basis of organic carbon content of the sediment, which yields often an underestimated value that has to be corrected by a factor of 1.5 or 1.6 for slightly evolved sediments. During kerogen evolution, i.e. diagenesis, the factor changes (1.2-1.3) as a result of the increase in carbon content of kerogen while at the same time soluble and/or volatile products are formed.



Types of Kerogen and Their Hydrocarbon Potential				
Environment	Kerogen Type	Kerogen Form	Origin	HC Potential
Aquatic	I	Alginite	Algal bodies	Oil
		Amorphous Kerogen	Structureless debris of algal origin	
	Structureless planktonic material, primarily of marine origin			
Terrestrial	II	Exinite	Skins of spores and pollen, cuticle of leaves and herbaceous plants	Gas, some oil
			III	
	IV	Inertinite		Oxidized, recycled woody debris

\*Crain's Petrophysical Handbook; [www.spec2000.net/11-vshtoc.htm](http://www.spec2000.net/11-vshtoc.htm)

### SRA/Rock-Eval Pyrolysis

SRA/Rock Eval pyrolysis comprises programmed heating in helium of a crushed sample (<100 mg). The amount of the free hydrocarbons contained in the sample and the hydrocarbon- and oxygen-containing compounds (CO<sub>2</sub>) that are volatilized during the cracking of the organic matter during programmed heating up to 550°C are determined.

The free hydrocarbons are determined from isothermally heating the sample at 300°C. The generated hydrocarbons are measured by a flame ionization detector and are referred to as the S<sub>1</sub> peak (Figure 6-1). The temperature is then increased from 300° to 550°C and hydrocarbons released from this thermal cracking are measured as the S<sub>2</sub> peak at the flame ionization detector. The temperature at which S<sub>2</sub> reaches its maximum rate of hydrocarbon generation is referred to as T<sub>max</sub>. CO<sub>2</sub> generated from the OM in the 300°-390°C range is measured by a thermal conductivity detector and is referred to as the S<sub>3</sub> peak.

In summary, Rock Eval provides the following data:

S<sub>1</sub> = amount of free hydrocarbons in sample (in milligrams of hydrocarbon per gram of rock). If S<sub>1</sub> >1 mg/g suggests oil or contamination of samples by hydrocarbons.

$S_2$  = amount of hydrocarbons generated through thermal cracking- provides measure of quantity of hydrocarbons that the rock has the potential of producing through diagenesis.

$S_3$  = the amount of  $CO_2$  (in milligrams  $CO_2$  per gram of rock) produced during pyrolysis of organic matter.  $S_3$  reflects the amount of oxygen in the OM.

$T_{max}$  = the temperature at which the maximum rate of generation of hydrocarbons occurs during pyrolysis.  $T_{max}$  is an indicator of the level of diagenesis of the OM.

A number of important parameters are calculated from Rock-Eval pyrolysis.

HI = hydrogen index ( $HI = [100 \times S_2]/TOC$ ).

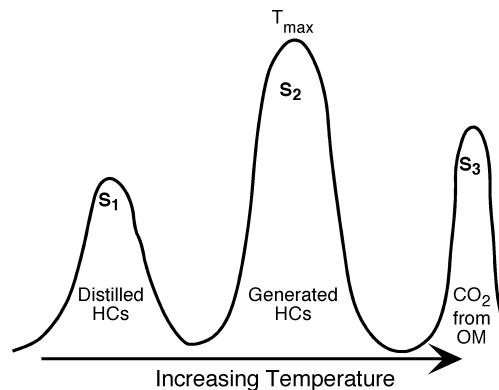
OI = oxygen index ( $OI = [100 \times S_3]/TOC$ ).

PI = production index ( $PI = S_1/[S_1 + S_2]$ ). PI is used to characterize the evolution level of the organic matter.

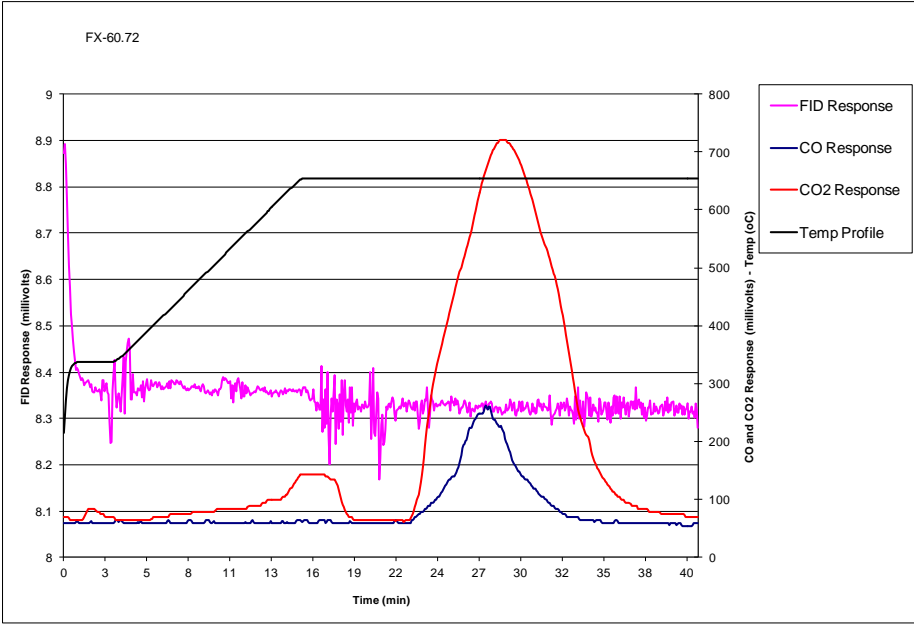
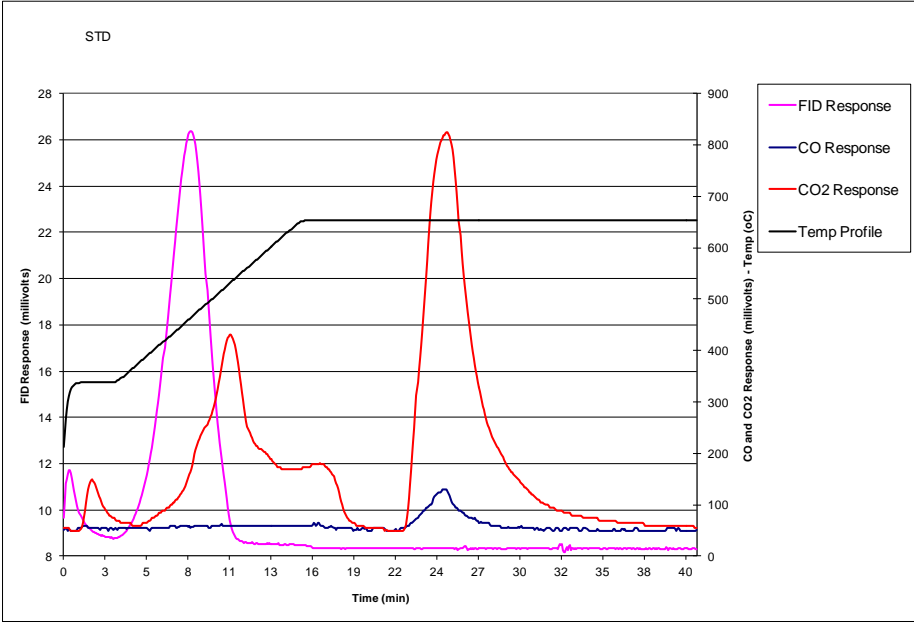
PC = pyrolyzable carbon ( $PC = 0.083 \times [S_1 + S_2]$ ). Carbon content of hydrocarbons volatilized and pyrolyzed during the analysis.

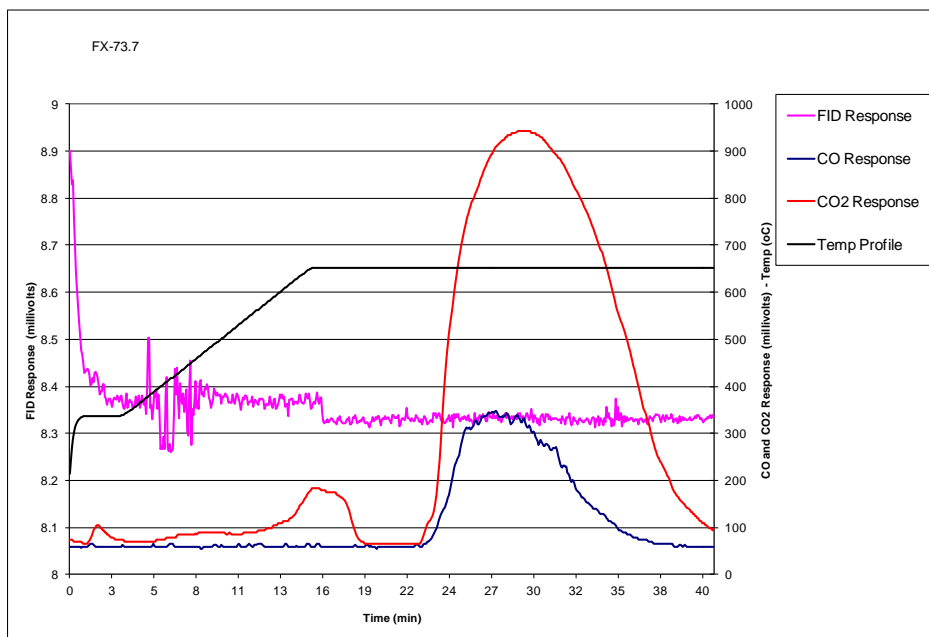
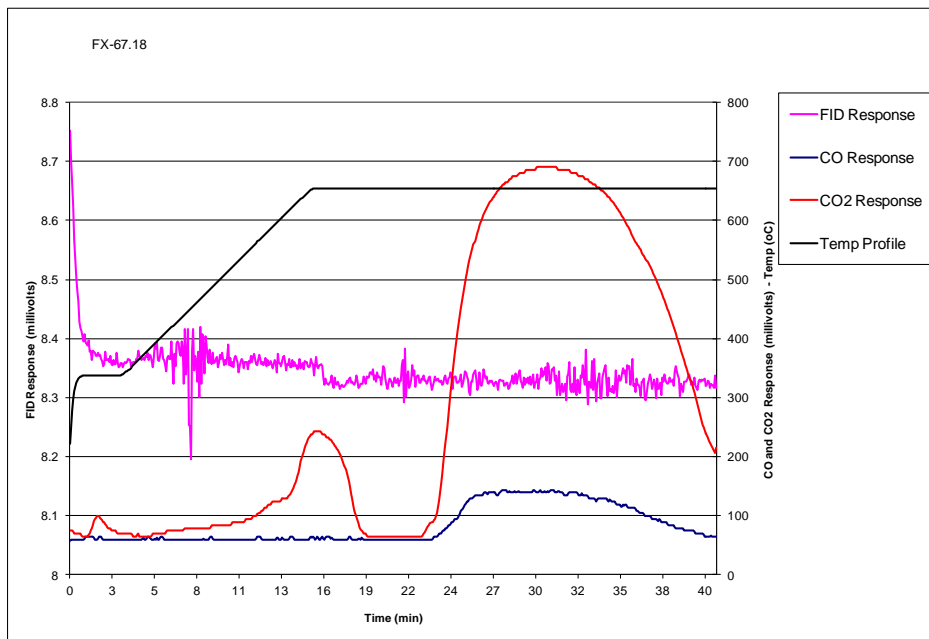
Kerogen type and degree of maturation of the organic matter can be estimated by cross-plotting of HI and OI on a van Krevelen diagram.

THE LEVEL OF DIAGENESIS AT WHICH THE OIL WINDOW OCCURS VARIES WITH KEROGEN TYPE. IN GENERAL  $T_{max} < 430^\circ C$  represents immature organic matter;  $T_{max} = 435^\circ - 450^\circ C$  defined the oil window;  $T_{max} > 450^\circ C$  indicates strata are over mature.



**Figure B1:** SRA pyrograms





Principal Authors:

Raphael A. J. Wust, PhD

Technical Advisor

*TRICAN GEOLOGICAL SOLUTIONS – a division of Trican Well Service Ltd.*

R. Marc Bustin, PhD, P. Geo., FRSC

Technical Advisor

*TRICAN GEOLOGICAL SOLUTIONS – a division of Trican Well Service Ltd.*

Ron Brezovski, P. Geol.

President

*TRICAN GEOLOGICAL SOLUTIONS – a division of Trican Well Service Ltd.*

Brent Nassichuk, MSc

Technical Manager

*TRICAN GEOLOGICAL SOLUTIONS – a division of Trican Well Service Ltd.*

Lisa Benson, BSc H.

Project Manager

*TRICAN GEOLOGICAL SOLUTIONS – a division of Trican Well Service Ltd.*

## Appendix C. Trican XRD analysis, methods and outputs

### Methods and sample details

The ground sample material was used to prepare smear slides (with ethanol as the transfer medium) on glass disks and dried. X-ray diffraction is conducted between 3 and 70° 2Theta using a Bruker D4 Endeavour X-ray diffraction instrument with a Lynx-Eye detector. The instrument is run at 40 kV and 30 mA and features a fixed divergence slit geometry (0.5°), an anti-scatter slit with both primary and secondary Soller slits at 4°.

After the samples are analysed, they are glycolated overnight in a glass desiccator at 60°C in order to determine expandable water sensitive clays (i.e. smectites or illite/smectite mixed-layers). Water-sensitive or swelling clays accommodate glycol molecules between the atomic layers which lead to a change of spacing between the layers. Because X-ray diffraction depends on interlayer distances and layer angles, incorporating glycol molecules in lattice structures produces peak position shifts in the XRD patterns. These samples were then analysed between 3-27° 2Theta. The range covers also the quartz 001 peak which is used for correction the any pattern shifts.

When kaolinite and therefore possibly also chlorite (chlorite 002 and kaolinite 001 peaks are overlapping) are present, the samples are also heat-treated at 550°C for 2 hrs in order to confirm if chlorite is present. Similar to the glycolation of the sample material, heating of the samples leads to the collapse of the crystal structure of certain clay minerals and hence leads either to a peak shift or peak disappearance (i.e. kaolinite at 550°C). These samples are then analysed between 10-22° 2Theta. The range covers also the quartz 001 peak which is used for correction the any pattern shifts.

The results of the x-ray diffraction analyses are analysed using the PDF-4 Minerals database 2009 (peak identification) and then quantified using Jade 9 software, a commercial Rietveld analyses program for quantification of the mineralogy. For further information on Rietveld theory refer to [http://en.wikipedia.org/wiki/Rietveld\\_refinement](http://en.wikipedia.org/wiki/Rietveld_refinement).

We would like to point out that Rietveld analysis only performs “quantitative” analysis of mineralogical phases identified from the XRD data. Mineral identification by **Trican Geological Solutions Ltd.** is done by reference to the International Centre for Diffraction Data database (<http://www.icdd.com/>). Most minerals can be unambiguously identified except for clays and complex solid solutions such as feldspars, amphiboles or even carbonates. Feldspars, which make up ~60% of the Earth’s crust contains the alkali feldspar (orthoclase/microcline–albite) and plagioclase (albite-anorthite) solid solution series where certain minerals have such similar X-ray diffraction patterns that they are essentially interchangeable for phase analysis. Carbonates on the other hand easily allow elemental substitution (i.e. Mg, Fe, Ni, Sr for Ca) which in small amounts will result in peak changes which are not present in the ICDD database. These carbonate phases will then most likely be slightly underestimated by the Rietveld refinement method. In addition, traces of some minerals may be present in the rock that produce only subtle diffraction patterns or the patterns are underlying others, more dominant phase patterns and hence their quantification may be difficult or impossible. Only if other data such as petrography or chemical analyses are available, better distinctions and mineral quantifications are possible. In order to characterize properly the mineralogical composition of rock

samples, other methods need to be incorporated, such as petrographic thin sections, chemical (XRF) or image (SEM/TEM) analyses, etc.

The standard patterns in the PDF-4 minerals database are used for both phase identification and quantification. Prior to all analysis, XRD pattern shifts are corrected using the Quartz 101 or Quartz 100 peak. For all samples, refinement of the scale factor and instrument zero is performed first and the background determination checked. The background is not corrected or subtracted prior to the Rietveld analysis.

In samples in which the mineralogy is composed of discrete minerals with fixed cell dimensions, such as calcite, quartz, gypsum and pyrite, the accuracy of the analyses by Rietveld is considered to be  $\pm 3-5\%$  relative. Samples with disordered clays (or solid solution series), such as some samples in this study, the accuracy of the data is less (sometimes  $> \pm 10\%$ ), the amount of which varies with the amount of disordered minerals. In samples in where substantial disordered clays are present Rietveld analyses does not fit the mineral patterns unless standard specifics to the samples are developed.

### **XRD peak patterns – explained**

---

FIGURE C1: XRD PATTERN OF AN OUTCROP SAMPLE FROM THE CHEVRON OUTCROP PROJECT AIR-DRIED (RED), AND GLYCOLATED (BLUE) AS AN EXAMPLE OF TYPICAL MINERAL PHASES IDENTIFIED IN THESE SAMPLES. QUARTZ, ALBITE, ORTHOCLASE, CALCITE, DOLOMITE, MICA/ILLITE, APATITE, PYRITE, GYPSUM, NATROLITE AND POSSIBLY PRENITE ARE PRESENT. NOTE: SCAN LENGTH SPANS 4-40° 2THETA.

---

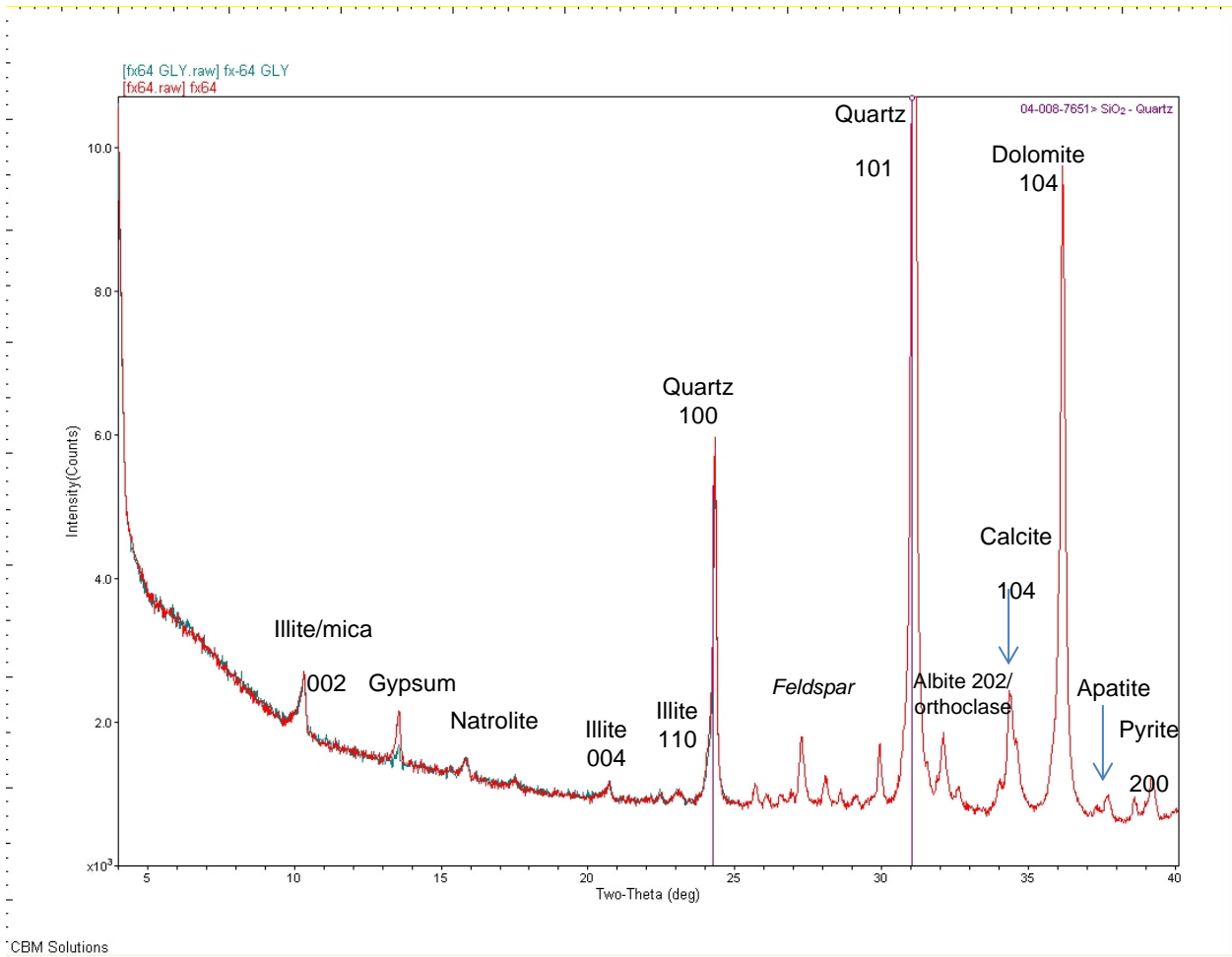
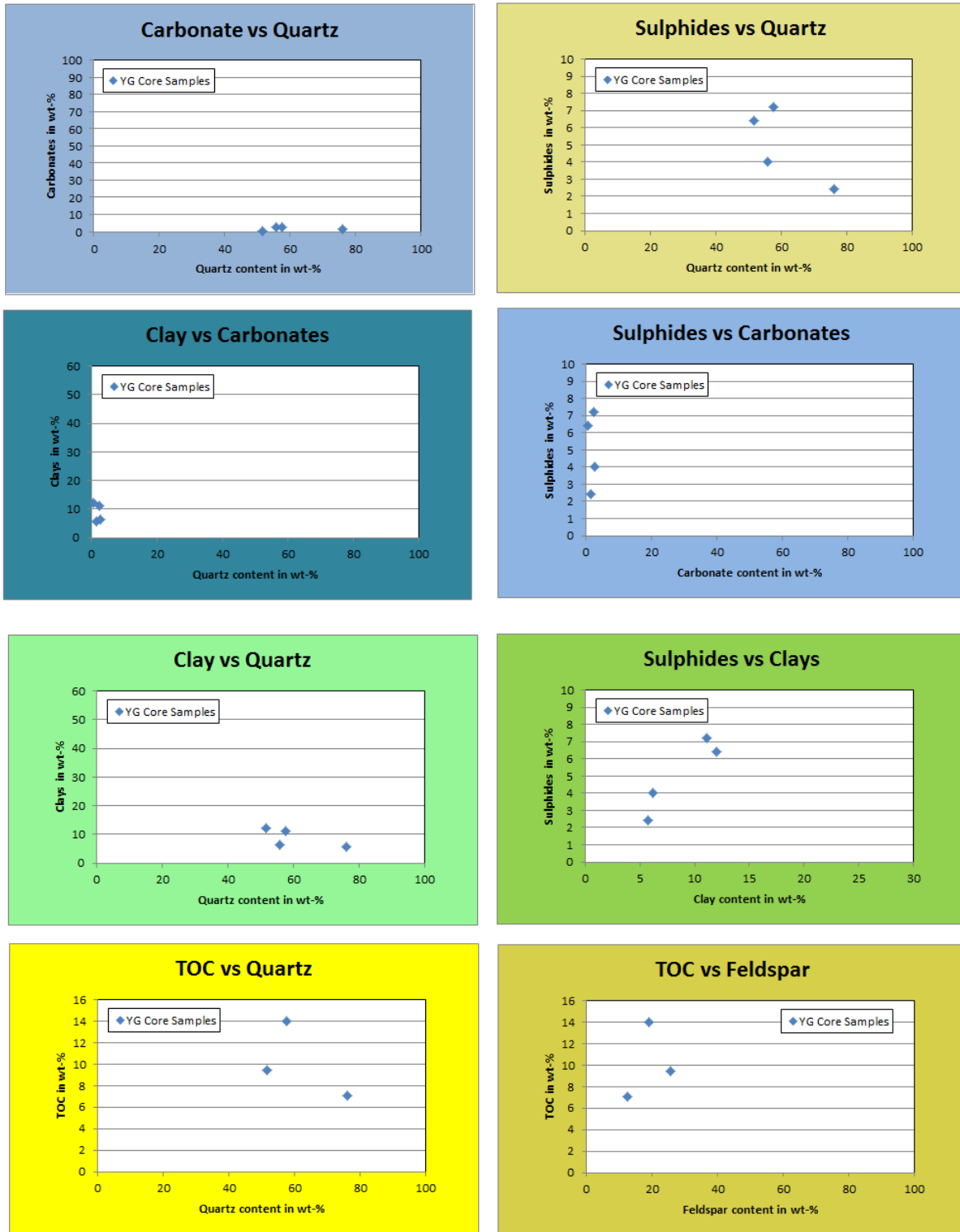
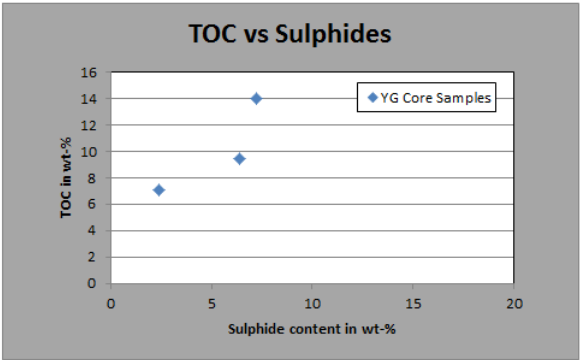
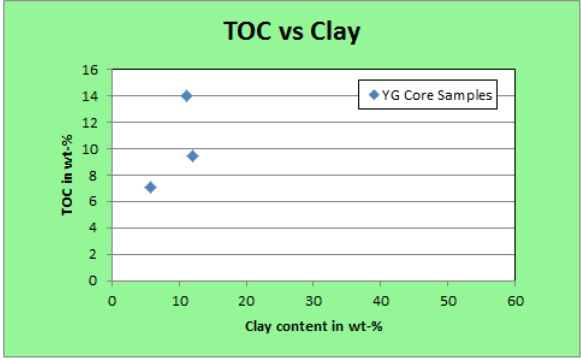
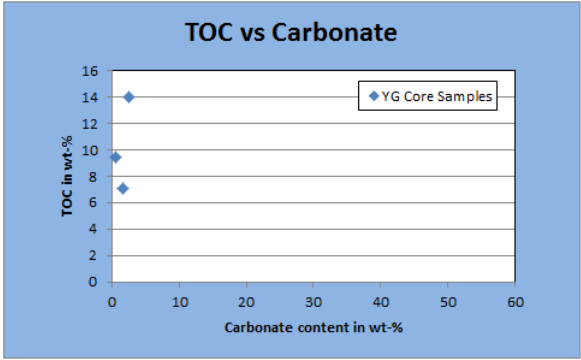


FIGURE C2. MINERALOGICAL COMPARISON PLOTS





## **Appendix D – Trican methods and experimental set-up for permeability and porosity**

### **1. Sample Preparation and Experimental Setup**

3 core samples were provided by Chevron for porosity, permeability, XRD and SRA analyses. A representative sample from each was selected for the porosity analysis. A 5 gram sub sample was used to measure the bulk density and a 20 gram sample was crushed and sieved with a 10 mesh screen (particle size 1.7mm and smaller) to measure skeletal density. Both the bulk and skeletal density samples were oven dried for 36 hours to ensure all samples were at similar moisture conditions. Porosity measurements were conducted on the dried, crushed component of the sample using a helium pycnometer.

### **2. Testing Procedure**

The bulk density was measured on a 5 gram uncrushed sample using mercury immersion. The technique involved the forced immersion of the sample under mercury. The weight of the displaced mercury was measured and, using the density of mercury at lab temperature, the volume of displaced mercury was calculated. The volume of mercury displaced is equal to the volume of the sample immersed. Due to the very high surface tension of mercury (mercury is a non-wetting liquid) mercury does not invade pores or micro-fractures and an accurate bulk volume is measured. Bulk density was calculated using the weight of the sample.

A helium pycnometer was used to measure the skeletal density of the crushed sample. Helium was used to minimize potential reactions with the samples that can occur with other gases (Cui et al, 2009). The helium pycnometer is comprised of sample and reference cells of known volume and a pressure transducer. The crushed sample was loaded into a sample cell and sealed. The reference cell was filled with helium and after the pressure within the reference cell had equilibrated, the pressure was recorded. The reference cell and sample cell are then opened to each other, allowing the helium from the reference cell to enter the sample cell. By recording the pressure after the system has reached a new equilibrium the volume of the system can be calculated using Boyle's gas law ( $P_1V_1=P_2V_2$ ). The difference between the known volume of the sample cell and the measured volume of gas is equal to the skeletal volume of the sample. Skeletal density was then calculated from the weight of the sample.

Permeability was measured on the crushed and sieved sample. Screens of mesh sizes 20 and 35

were used to sort the sample to a uniform particle size (approximately 0.67 mm). The same procedure as described above (for skeletal density) is used to collect pressure decay data during

the analysis. The late time pressure decay data was used to calculate permeability via a method refined from ResTech (1996) and Luffel et al. (1993). Permeability was calculated at ambient conditions and, although widely quoted in industry, was not calibrated to in situ conditions. Reported values are therefore to be used only for comparative purposes.

## 1. Data Analysis

The porosity under unconfined stress conditions and at laboratory temperature is calculated by:

$$\phi = \left( \frac{1}{\rho_B} - \frac{1}{\rho_{Sk}} \right) \rho_B \times 100,$$

Where (**units are bolded**):

$\rho_B$ , bulk density, **g/cc**

$\rho_{Sk}$ , skeleton density, **g/cc**

## 2. References

API 40, 1998, Porosity Determination in Recommended Practices for Core Analysis, pp.5-1-23, *API Publishing Services, 1220 L Street, N.W., Washington, D.C. 20005-4070*

Cui X., Bustin M. M., Bustin R. M., 2009. Measurements of gas permeability and diffusivity of tight reservoir rocks: different approaches and their applications. *GeoFluids* **9**, 208-223.

Luffel D.L., Hopkins C.W., Shettler P.D., 1993. Matrix Permeability measurements of gas productive shales, Paper SPE presented at the 1993 SPE Annual Technical Conference and Exhibition, 3-6 October, Houston, Texas.

ResTech, 1996. Development of Laboratory and Petrophysical Techniques for Evaluating Shale Reservoirs. GRI-95/ 0496, Gas Research Institute, Chicago, Illinois, 279.

## Appendix E – Trican methods for microporosimetry

### Background

Modified from Pittman (1992)

Washburn (1921) first used mercury injection as a laboratory method for studying the pore aperture size distribution in porous rocks. Washburn's equation which is the widely used for interpreting intrusion data is:

$$P_c = -2 \gamma \cos \theta / r \quad (1)$$

where  $P_c$  = capillary pressure (dynes/cm<sup>2</sup>),  $\gamma$  = surface tension of Hg (480 dynes/cm),  $\theta$  = contact angle mercury in air (140°), and  $r$  = radius of pore aperture assuming a cylindrical pore.

Washburn assumed the pores were cylindrical and some of the limitations of these assumptions were addressed by Van Brakel et al. (1981). In interpreting conventional porous reservoir rocks it is common to differentiate entry pressure, displacement pressure, and threshold pressure based on the shape of the injection curve. Entry pressure is the pressure at which mercury first enters the pores and reflects the largest pore apertures (Robinson, 1966). Entry pressure is difficult to define in many rocks due to irregularity of the samples. This parameter often is vague and difficult to determine because of the sample size and surface irregularities of the rock. Schowalter (1979) defined displacement pressure as the pressure at which 10% mercury saturation occurs. Threshold pressure was defined by Katz and Thompson (1986, 1987) as the pressure at which mercury forms a connected pathway across the sample and corresponds to the inflection point on a mercury injection plot.

### References

- API 40, 1998, Porosity Determination in Recommended Practices for Core Analysis, pp.5-1-23, *API Publishing Services, 1220 L Street, N.W., Washington, D.C. 20005-4070*
- Katz, A.J., and A.H. Thompson, 1986. Quantitative Prediction of Permeability in Porous Rock. *Physical Review B*, v. **34**, pg.8179-8181.
- Katz, A.J., and A.H. Thompson, 1987. Prediction of Rock Electrical Conductivity from Mercury Injection Measurements. *Journal of Geophysical Research*, v. **92**, pg. 599-607.
- Pittman, E.D., 1992. Relationship of porosity and permeability to various parameters derived from mercury injection-capillary pressure curves for sandstone. *The American Association of Petroleum Geologists Bulletin*, v. **76 no.2**, pg. 191-198.

Robinson, R.B., 1996. Classification of Reservoir Rocks by Surface Texture. AAPG Bulletin, **v.50**, pg. 547-559

Schowalter, T.T., 1979, Mechanics of Secondary Hydrocarbon Migration and Entrapment. AAPG Bulletin, **v.63**, pg.723-760

Van Brakel, J., S. Modry, M. Svata, 1981. Mercury Porosimetry: State of the Art. Powder Technology, **v.29**, pg. 1-12

Washburn, E.W., 1921. Note on a method on determining the distribution of pore sizes in a porous material. Proceedings of the National Academy of Science, **v.7**, pg. 115-116.

Webb, P.A., 2001. An introduction to the physical characterization of materials by mercury intrusion porosimetry with emphasis on the reduction and presentation of experimental data. *Micromeritics Corp. 4356 Communications Dr. Norcross, GA.*

## Appendix F – Trican petrology and SEM classification scheme

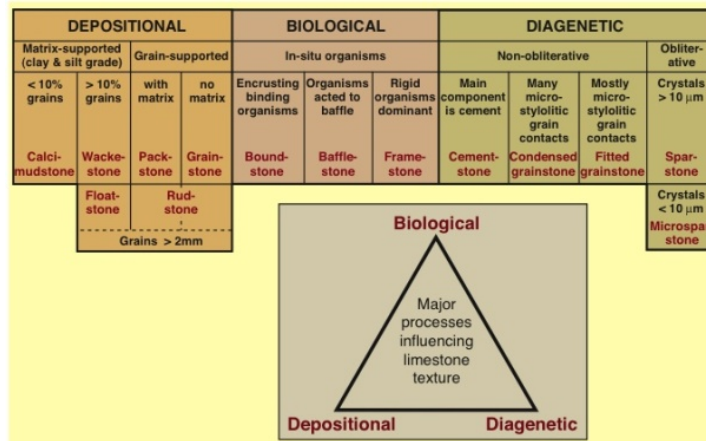
Sedimentary rocks are often classified as either carbonate or siliciclastic rocks. **Carbonate/limestone rocks** are a group of rocks composed of CaCO<sub>3</sub> (and thus reacting with HCl acid). Carbonate rocks (limestones and dolomites) are usually described using the allochems (large, transported pieces) and the interstitial material, i.e. matrix. Allochems include fossils, oolites, pellets, intra- and extraclasts. For carbonate classification, two schemes are generally used; The Folk (1959) and the Dunham (1962) classification (Fig. 82-84). Folk's (1959 and 1962) classification (Folk, R.L., 1959, Practical petrographic classification of limestones, AAPG Bulletin, 43, 1-38) subdivides limestones primarily on the basis of matrix content. Most limestones are classified as allochemical rocks if they contain over 10% allochems (transported carbonate grains). Based on the percentage of interstitial material, the rocks may be further subdivided into two groups: sparry allochemical limestones (containing a sparry calcite cement of clear coarsely crystalline mosaic calcite crystals) and microcrystalline allochemical limestone (containing microcrystalline calcite mud and micrite which is subtranslucent grayish or brownish particles less than about 5 microns in size). Further subdivision is based on the allochem ratios of Folk (1962) (Folk, R.L., 1962, Spectral subdivision of limestone types, in Ham, W.E., Classification of Carbonate Rocks: AAPG Memoir 1, 62-84). The Folk's classification is best suited for thin section study. Rocks with appreciable matrix are termed micrites while matrix-free rocks that contain sparry calcite cement are termed sparites. Further information on classification of carbonate rocks and allochems can be found at: <http://sepmstrata.org/caco3-petrology.html>

In contrast, Dunham's classification (Dunham, RJ, 1962, Classification of carbonate rocks according to depositional texture. In: Ham, W. E. (ed.), Classification of carbonate rocks: American Association of Petroleum Geologists Memoir, p. 108-12) and its modification by Embry and Klovan (Embry, AF, and Klovan, JE, 1971, A Late Devonian reef tract on Northeastern Banks Island, NWT: Canadian Petroleum Geology Bulletin, v. 19, p. 730-781) and James (James, NP, 1984, Shallowing-upward sequences in carbonates, in Walker, RG, ed., Facies Models: Geological Association of Canada, Geoscience Canada, Reprint Series 1, p. 213-228) deals with depositional texture.

Original components not bound together at deposition				Original components bound together at deposition. Intergrown skeletal material, lamination contrary to gravity, or cavities floored by sediment, roofed over by organic material but too large to be interstices
Contains mud (particles of clay and fine silt size)		Lacks Mud		
Mud-supported		Grain-supported		
Less than 10% Grains	More than 10% Grains			
Mudstone	Wackestone	Packstone	Grainstone	Boundstone

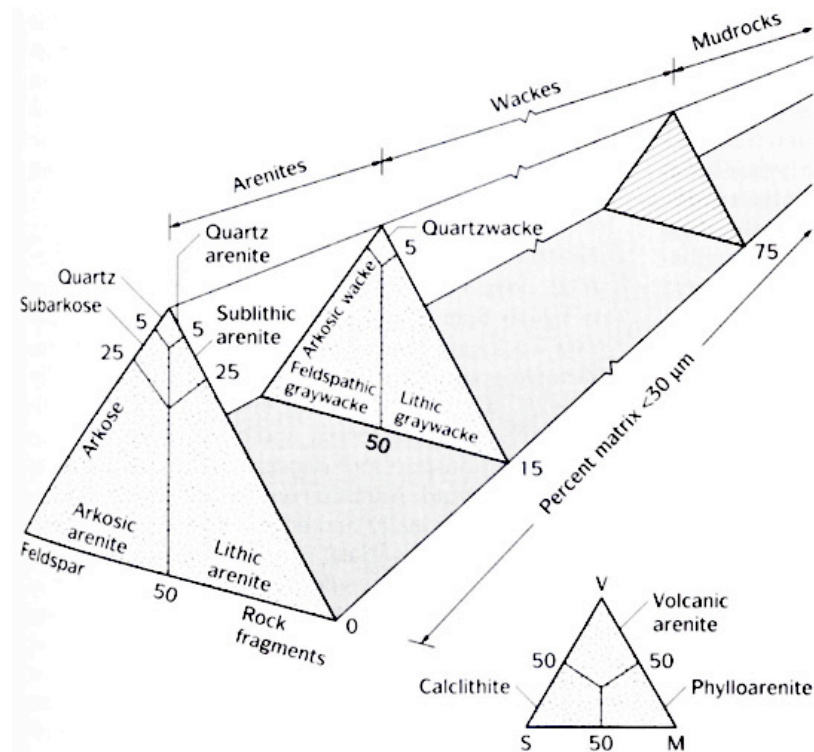
C. G. St. C. Kendall, 2005 (after Dunham, 1962, AAPG Memoir 1)

For this reason, the Dunham scheme may be better suited for rock descriptions that employ a hand lens or binocular microscope. For example, if the grains of a limestone are touching one another and the sediment contains no mud, then the sediment is called a grainstone. If the carbonate is grain supported but contains a small percentage of mud, then it is known as a packstone. If the sediment is mud supported but contains more than 10 percent grains, then it is known as a wackestone, and if it contains less than 10 percent grains and is mud supported, it is known as a mudstone. For diagenetic changes of depositional fabrics, the Dunham scheme is not sufficient and Wright (1992) modified the original Dunham classification scheme to cover such carbonate rocks. Further details can be obtained on page 349 of E. Flügel (2004). *Microfacies of carbonate rocks*, Springer Verlag, Berlin, 976 pp. or Wright, V. P., 1992, *A revised classification of limestones: Sedimentary Geology*, v. 76, p. 177-185; and Scholle, P.A. and Ulmer-Scholle, D. 2003. *A Color Guide to the Petrography of Carbonate Rocks: Grains, textures, porosity, diagenesis*. AAPG Memoir 77:



Terminology for very fine grained **clastic rocks** is somewhat variable but, generally incorporates claystones, mudstones and siltstones into the grab-bag term 'shale'. For petrographic purposes, the following general rules are applied. The term mudrock encompasses rocks composed of clay- and silt-sized detritus. The terms shale and claystone are used to describe rocks containing less than 33% silt-sized particles, and displaying a laminated (fissile) or non-laminated fabric, respectively. Rocks composed of between 33% and 66% silt-sized particles displaying a laminated fabric are shales, and with a massive fabric, mudstones. The term 'silty' is appended to the general terms if it appears there is close to 33% silt embedded in the matrix. Siltstones consist of less than 33% matrix. Grain size variations are variously 'interlaminated' or 'interbedded' (>1cm thick) or simply 'variable'.

Sandstones are commonly divided into two major groups based on their textures. If the rocks are composed of grains only, they may be termed arenites. Comparatively if the rocks contain more than 15% matrix they are classified as wackes. Quartz arenite is applied to rocks with >95% quartz grains while arkosic arenite refers to an arenite with >25% feldspars (which must exceed the rock fragment component). The term litharenite is applied to a rock which contains >25% lithics (which must exceed the feldspar component). The terms subarkose and sublitharenite can also be used for samples which contain <25% but >5% feldspar and lithics, respectively, and contain higher volumes of feldspar (subarkose) or lithics (sublitharenite) (Tucker, 2001; see figure below).



## **REFERENCES**

Dumala, M. 2007. Assessment Report - Prospecting, mapping, geochemical sampling and diamond drilling at the Fox Property. FOX 1-188, YC52526-YC 52713. Dawson Mining District, Yukon Territory. Archer, Cathro & Associates (1981) Ltd. Yukon Energy Mines & Resources Library Catalogue Report 094870, p. 1-207.

Fraser, T.A., Allen, T.L., Lane, L.S., and Reyes, J.C., 2012. Shale gas potential of Devonian shale in north Yukon: Results from a diamond drillhole study in western Richardson Mountains. *In: Yukon Exploration and Geology 2011*, K.E. MacFarlane and P.J. Sack (eds.), Yukon Geological Survey, p. 45-74.

Lane, L.S., Snowdon, L.R. and Obermajer, M., 2010. Rock-Eval/TOC and oil show analyzer data for selected Yukon borehole samples; Geological Survey of Canada, Open File 6652, 1 CD-Rom.

Lane, L.S., Hayman, A., Utting, J., and Sweet, A.R., 2012. Summary of current geochemical, geophysical and biostratigraphic data for Chevron SOBC WM N. Parkin YT D-61 (UWI 300D616630137000), Eagle Plain, Yukon; Geological Survey of Canada, Open File 7050, 1 CD-ROM. doi:10.4095/290117